

AN ABSTRACT OF THE DISSERTATION OF

Hiral Patel for the degree of Doctor of Philosophy in Physics presented on September 1, 2017.

Title: Interlayer Electronic Interactions in Twisted and Stacked Bilayer Graphene

Abstract approved: _____

Matt W. Graham

The photophysical properties of two-dimensional (2D) layered van der Waals (vdW) materials, and their heterostructures are manifestly distinct from crystalline bulk materials. Recently, the discovery of new 2D vdW materials and strongly-bound interlayer excitons in these materials has created a new branch in nanoscience. As such, there are a number of ways to stack 2D materials to produce novel heterostructures with ground-breaking interlayer electronic and photophysical properties. This dissertation explores the stacking and twisting degree of 2D vdW layers to engineer new interlayer electronic states that are not present in as-grown stacked materials. In particular, graphene is the prototypical highly conductive, metallic vdW material consisting of carbon atoms arranged in a hexagonal lattice. When two sheets of graphene are stacked at an off-axis angle, twisted bilayer graphene (tBLG) is formed with modified interlayer electronic properties from the orbital hybridization.

This dissertation presents the first exploration and discovery of bound excitons in electronically hybridized interlayer states in tBLG. Using tBLG as a prototype, this

research provides new methodologies to understand the time-domain light-matter interactions in a 2D heterostructure. In particular, we film the journey of electrons in tBLG from excitation to relaxation with space-time and energy resolution to study fundamental interlayer electronic properties and many-body electronic effects.

When two graphene sheets stack in a tBLG configuration, angle-tunable optical absorption resonances are generated owing to the rehybridization of interlayer orbitals. Early characterization of tBLG graphene was limited to optical absorption and Raman scattering studies. We apply advanced nonlinear optical techniques to tBLG for the first time to understand the underlying Physics of interlayer electronic interactions in stacked and twisted graphene materials. To accomplish this, we developed a novel ultrafast multi-photon transient absorption (TA) microscopy technique to map relative electron population in a single grain of tBLG with the space-time and energy resolution. Even though graphene is a semimetal, upon resonant excitation of interlayer excitons, surprisingly, we observe a clear electronic relaxation bottleneck that is not present in either ‘non-twisted’ Bernal stacked bilayer graphene or monolayer graphene. This bottleneck can be best explained by the existence of a strongly bound, dark excitonic state. To further investigate the nature of the excitonic states and the exciton binding energy, we employ near-IR excited state absorption (ESA) microscopy approach. By measuring the excited state absorption manifold in tBLG, we found exciton binding energy of ~ 0.5 eV. Such a large exciton binding energy in tBLG is comparable to other 2D semiconductor vdW materials such as transition metal dichalcogenides (TMDs) and an order of magnitude larger than the reported value in metallic carbon nanotubes (CNTs).

Lastly, we report light emission from a semimetal tBLG for the first time. We developed a novel 2-photon photoluminescence (PL) microscopy technique to detect emission. The detected PL energy is tunable with the absorption resonance energy. We find that upon resonant two-photon excitation, the relatively slow process of PL is possible owing to the strongly-bound excitons with large binding energy and the corresponding long-lived recombination times measured.

Collectively, our results demonstrate that resonantly excited tBLG functions as a unique 2D-hybrid material where free-electron continuum states may co-exist alongside strongly-bound and stable exciton states. The discovery of these remarkable interlayer interactions opens up possible new avenues for excitonic applications with graphene-based light harvesting technologies and fast photosensor development.

©Copyright by Hiral Patel
September 1, 2017
All Rights Reserved

Interlayer Electronic Interactions in Twisted and Stacked Bilayer Graphene

by
Hiral Patel

A DISSERTATION

submitted to

Oregon State University

in partial fulfillment of
the requirements for the
degree of

Doctor of Philosophy

Presented September 1, 2017
Commencement June 2018

Doctor of Philosophy dissertation of Hiral Patel presented on September 1, 2017

APPROVED:

Major Professor, representing Physics

Chair of the Department of Physics

Dean of the Graduate School

I understand that my dissertation will become part of the permanent collection of Oregon State University libraries. My signature below authorizes release of my dissertation to any reader upon request.

Hiral Patel, Author

ACKNOWLEDGEMENTS

I would like to acknowledge my research advisor Matt Graham, whose support and scientific insights have guided me throughout my research. I would like to thank my group members for the helpful discussions and comments. I am thankful to the entire faculty, staff in the Physics Department and my committee members Ethan Minot, Guenter Schneider, Chong Fang, Oksana Ostroverkhova, John Conley and Douglas Warrick for their guidance and discussions.

I would like to thank my fellow graduate students and friends in the department and outside the department for having the time to help me when I needed. I am grateful for the encouragements and unconditional support I have received from my parents and my siblings, which helped me throughout this journey. Most importantly, I want to thank my wonderful husband Jatin who kept me sane and supported me with the whole process.

CONTRIBUTION OF AUTHORS

Robin Havener, Lola Brown, Lujie Hung, Cheol-Joo Kim in the Park group at Cornell University provided tBLG samples for all the experiments (Chapter 3, 4, 5). Lola Brown performed dark field TEM imaging to characterize the twist angle between two sheets of graphene (Chapter 3, 4, 5). Jeaseok Hao prepared $\text{Cu}_{10}\text{Te}_4\text{S}_{13}$ crystals, James Haggerty, and Chris Reidy from Tate group in the Physics department performed the thin film deposition in Appendix A (Chapter 8). For Appendix B, Collin Muniz prepared samples and Sandia lab staff performed quantum yield measurements. Matt Graham provided insight, and guidance for all aspect of the work presented here.

TABLE OF CONTENTS

	<u>Page</u>
1. INTRODUCTION	1
1.1 Introduction.....	1
1.2 2D Materials	4
1.3 Methods of Obtaining 2D Materials	9
1.3.1 Micromechanical Exfoliation	9
1.3.2 Liquid Exfoliation.....	11
1.3.3 Chemical Vapor Deposition.....	13
1.4 Construction of Heterostructures	17
1.4.1 Transfer Process of Graphene.....	17
1.4.2 Artificial Transfer Process to Create 2D Heterostructures	18
1.4.3. Vertical and Lateral Heterostructure Formation with CVD Growth	20
1.5 Summary and Outlook	22
2. IMAGING AND CHARACTERIZING 2D MATERIALS	24
2.1 Introduction.....	24
2.2 Optical Microscopy.....	25
2.3 Hyperspectral Microscopy	27
2.4 Photoluminescence Microscopy	35
2.5 Transient Absorption Microscopy and Spectroscopy.....	38
2.6 Raman Spectroscopy and Wide-Field Raman Imaging.....	42
2.7 Electron Microscopy.....	46
2.8 Scanning Probe Microscopy	51

TABLE OF CONTENTS (Continued)

	<u>Page</u>
2.9 Characterization of Twisted Bilayer Graphene	58
2.10 Summary.....	60
3. THEORY: INTERLAYER ELECTRONIC STRUCTURE.....	62
3.1 Electronic Band Structure of Graphene in the Tight Binding Approximation	63
3.2 Electronic Band Structure of Bilayer Graphene in the Tight Binding Approximation	65
3.3 Effective Free Electron Model: Electronic Band Structure of tBLG.....	68
3.4 Bound Exciton Model for tBLG	72
3.4.1 Excitonic Effects in Nanomaterials	72
3.4.2 Fano Resonance and Bound Excitons.....	73
4. TUNABLE OPTICAL EXCITATIONS IN TWISTED BILAYER GRAPHENE FORM STRONGLY BOUND EXCITONS.....	78
4.1 Introduction.....	79
4.2 Free Electron Vs. Bound Exciton Model.....	79
4.3 TA Microscopy on Single tBLG Domains	82
4.4 Electronic Relaxation Bottleneck	82
4.5 One and Two Photon TA Spectrum and Maps.....	86
4.6 One and Two Photon Relaxation Kinetics.....	90
4.7 Summary	91
4.9 Supporting Information.....	94

TABLE OF CONTENTS (Continued)

	<u>Page</u>
5. PHOTOLUMINESCENCE FROM STRONGLY-BOUND INTERLAYER EXCITONS IN TWISTED BILAYER GRAPHENE	105
5.1 Introduction.....	106
5.2 Photoluminescence from tBLG -2-ph PL Microscopy	107
5.3 tBLG Photoluminescence Mechanism.....	110
5.4 Photoluminescence Excitation Spectrum and Spatial Maps.....	113
5.6 Exciton Binding Energy with Near-IR Intraband TA Microscopy.....	117
5.7 Summary	120
6. CONCLUSIONS AND OUTLOOK.....	123
6.1 Summary	123
6.2 Future Outlook	126
6.2.1 Introduction.....	126
6.2.2 Femtosecond Resolved Near-field Photocurrent Generation	127
6.2.3 Polarization and Handedness Dependent Optical Properties of tBLG	130
6.2.4 Engineering 2D vdW Heterostructures With and Without Twist	133
7. BIBLIOGRAPHY	136
8. APPENDICES	160
APPENDIX A: NEW CLASS OF HIGH-EFFICINCEY THIN-FILM TETRAHEDRITE SOLAR ABSORBER- $\text{Cu}_{10}\text{Te}_4\text{S}_{13}$	160
8.1 Introduction.....	160
8.2 Experiment and Methods	161
8.3 Results and Discussion	164

TABLE OF CONTENTS (Continued)

	<u>Page</u>
8.4 Summary	171
References.....	173
APPENDIX B: LUMINESCENCE STUDIES ON SERIES OF OXALATE LINKED HETEROMETALLIC COORDINATION POLYMERS	176

LIST OF FIGURES

<u>Figure</u>	<u>Page</u>
Figure 1.1: Typical 2D vdW layered lateral and vertical heterostructure. Weak vdW	4
Figure 1.2: Graphene. (a) Honeycomb lattice of graphene with two distinct atoms per unit	5
Figure 1.3: Hexagonal boron nitride. (a) Atomic structure of h-BN with hexagonal.....	6
Figure 1.4: MoS ₂ . (a) (i) Top view of atomic structure of MoS ₂ showing honeycomb.....	7
Figure 1.5: Absorption and photoluminescence spectrum of MoS ₂ . (a) Absorption.....	8
Figure 1.6: Mechanical exfoliation process. (a-f) (a) Material to be exfoliated is placed on	10
Figure 1.7: Schematic of liquid exfoliation process. (a) Between the layers of 2d	11
Figure 1.8: CVD synthesis mechanism. (a) Schematic of CVD growth process of.....	14
Figure 1.9: Graphene transfer process. (a) CVD grown graphene is transferred to a.....	17
Figure 1.10: tBLG artificial transfer process. (a) Starting with CVD aligned graphene ..	19
Figure 1.11: Vertical and in-plane heterostructure growth process of WS ₂ /MoS ₂ . (a).....	21
Figure 2.1: Graphene and WSe ₂ optical imaging. (a) Exfoliated graphene on 300 nm	26
Figure 2.2: Optical absorption spectroscopy in graphene. (a) Optical transitions.....	28
Figure 2.3: Schematic of the Horiba Fluorolog. Xenon arc lamp provides a broadband .	30
Figure 2.4: Schematic of hyperspectral microscopy. The light from Horiba fluorolog is	31
Figure 2.5: Data processing of hyperspectral images. (a) Snapshot of a CVD grown	32
Figure 2.6: Optical imaging of tBLG. (a) Hyperspectral imaging snapshot of CVD grown	34
Figure 2.7: Photoluminescence map of MoS ₂ single crystal. (a) PL spectra of single (red)	36
Figure 2.8: Transient Absorption spectroscopy. (a) Schematic of pump-probe experiment	39

LIST OF FIGURES (Continued)

<u>Figure</u>	<u>Page</u>
Figure 2.9: Energy level diagram, TA spectroscopy, and time dynamics. (a) Energy level	41
Figure 2.10: Raman spectroscopy of graphene and tBLG. (a) Typical Raman signatures	44
Figure 2.11: Micro Raman, widefield Raman microscopy, and Raman G-band.....	45
Figure 2.12: TEM images of vdW 2D materials MoS ₂ , MoSe ₂ , WS ₂ , WSe ₂ , and	48
Figure 2.13: Dark field TEM imaging of 2D materials. Diffraction spots, and	49
Figure 2.14: SEM imaging of CVD grown graphene and MoS ₂ . (a) Large graphene single	50
Figure 2.15: Schematic of scanning probe microscope. (a) SPM schematic. PZT scanner	52
Figure 2.16: AFM imaging of multilayer and single layer graphene. (a) Graphene on the	54
Figure 2.17: Electrical measurement schematic of C-AFM, zooming in at the tip at the	56
Figure 2.18: STM imaging of graphene, and tBLG showing atoms and local density of	57
Figure 2.19: Areas containing low-angle tBLG were first identified using TA	59
Figure 2.20: Hyperspectral microscopy characterization. ³⁸ (a) Off-resonant linear.....	60
Figure 3.1: (a) Lattice structure of single layer graphene; Two carbon atoms per unit cell	64
Figure 3.2: Band structure of graphene and bilayer graphene. (a) Representation of	67
Figure 3.3: (a) Unit cell size as a function of twist angle. The lower bound for the	71
Figure 3.4: Excitonic effects in graphene. The experimental optical conductivity	73
Figure 3.5: Bound Exciton model. (a) Upon resonant optical excitation, degenerate Fano	75
Figure 4.1: (a) tBLG free-electron interlayer band-structure. (b) Cross-sectional view ..	80
Figure 5.1: Two-photon photoluminescence. (a) i. Ultrafast 2-photon photoluminescence	109

LIST OF FIGURES (Continued)

<u>Figure</u>	<u>Page</u>
Figure 5.2: Tunable photoluminescence. (a) Electronic bandstructure cross-sectional view	111
Figure 5.3: 2-photon emission. (a) Energy diagram of the bound exciton model outlines	114
Figure 5.4: tBLG intraband, 2-ph TA, and 2-ph PL microscopy. TA and PL response.	116
Figure 5.5: tBLG intraband and 2-ph TA microscopy. (a) TA measurements on a 7.9°	118
Figure 6.1: (a) Near-field optical microscope setup. (b) tBLG will have its	129
Figure 6.2: Optical activity, photoluminescence, and photocurrent in as a function of.	131
Figure 6.3: Helicity dependent off-resonant time dynamics of tBLG. Same helicity	132
Figure 6.4: (a) Differential transmission spectrum from WSe ₂ , heterostructure,	134
Figure 8.1: Tetrahedrite crystal structure showing Cu (Td), Cu (Tri), S (Td) and S (Oh) sites. [Adapted from ⁷ .]	165
Figure 8.2: (a) XRD of Cu ₁₀ Te ₄ S ₁₃ showing single phase tetrahedrite phase. ⁷	166
Figure 8.3: Total (a) and projected (b, c, d) density of states for Cu ₁₀ Te ₄ S ₁₃	167
Figure 8.4: Optical absorption, transmission and reflection spectrum showing abrupt absorption edge at ~ 1.4 eV confirming the bandgap.	168
Figure 8.5: Photoluminescence spectrum of Cu ₁₀ Te ₄ S ₁₃ for excitation above bandgap. (a)	169
Figure 8.6: Time dynamics of Cu ₁₀ Te ₄ S ₁₃ . (a) Sketch of energy level showing pump and	170

INTERLAYER ELECTRONIC INTERACTIONS IN TWISTED AND STACKED BILAYER GRAPHENE

1. INTRODUCTION

1.1 Introduction

The term nanotechnology was first used in 1974 by Norio Taniguchi to refer to any field of study that deals with the synthesis, manipulation, and separation of materials on the order of one atom or one molecule.¹ Physical properties of many bulk materials are well understood. However, when the dimension becomes smaller, going from 3-dimensions to 2 or 1 dimension, many material properties modify drastically. At this scale, quantum confinement effects can be observed such as plasmon resonance in metal nanoparticles, quantum confinement in semiconductors and so on. There has been a massive effort around the world to develop various nanomaterials for applications in electronics, biomedical, sensing, solar technology, and so forth. Being able to control these materials at the nanometer scale and emergence of promising new properties opens up a new realm of applications from electronics to sensing. Understanding how these materials behave at the nanometer scale offers a new platform in realizing new approaches to better explain the world around us.

One of the fascinating aspects of the nanomaterials is that they can be easily manipulated to form complex structures to create desired physical properties. For fundamental research and applications, many carbon based nanomaterials such as carbon

nanotubes, fullerenes, and graphene are widely studied. In particular, there has recently been a tremendous development in the field of the family of 2D materials, such as hexagonal boron nitride (h-BN), transition metal dichalcogenides (TMDs) and others since the discovery of graphene in 2004.^{2,3} The single layer 2D materials are continuous sheets with one or two atom thickness, where one sheet interacts through van der Waals (vdW) forces with other adjacent or bulk surfaces. Some of the most exciting applications are based on the quantum interlayer effects resulting from multiple 2D layer interactions, which is not present in a single material. Control over the stacking and twisting of 2D vdW materials offers a new degree of freedom that is inaccessible with traditional 3D bulk materials. Recently, the family of 2D vdW materials has grown substantially. As a result, there are many exciting possibilities of stacking and twisting 2D vdW materials to produce desired interlayer electronic states for the next generation optoelectronics.

Graphene is a 2D structure of carbon atoms arranged in a hexagonal lattice with two-carbon atoms per unit cell.^{2,3} It is the thinnest yet strongest material in the world which is electrically and thermally conductive, elastic, transparent and impermeable to gases.^{4,5} Graphene is well-suited for many novel applications such as: touch screens, solar cells owing to low resistance, and transparency; electronic devices due to lightweight and flexible properties; transistors and photodetectors due to high electron mobility.⁶⁻⁸ This dissertation focuses primarily on graphene. In particular, it focuses on twisted bilayer graphene (tBLG) configuration, which is created when two sheets of graphene are stacked and twisted at an off axis angle relative to each other. We focus on understanding the nature of the hybridized electronic states upon stacking two 2D materials. Although the intrinsic properties of many 2D materials have thoroughly been studied recently,

many of the twisted heterostructures of 2D materials have not been explored and are poorly understood. To understand the twisted heterostructure better, this dissertation addresses few challenges to help 2D material heterostructure reach its maximum potential as a viable candidate to transform photonic technology.

We develop a basic tool that is required to understand electron dynamics in 2D materials beyond optical absorption. Owing to the size and spatial variation in the structural composition of 2D materials, it is important to have control over large scale spatial imaging in the time domain to obtain useful information beyond optical absorption in the material. We use transient absorption (TA) approach to capture electron population as a function of space, time and energy providing helpful information such as homogeneity, time dynamics, and charge transfer processes. This information is essential to create any viable devices to advance technology in the field of solar or photovoltaic. Our approach can be used to study relative electron population and dynamics of 2D materials and their heterostructures. In Chapter 2, we discuss TA microscopy technique to acquire diffraction limited spatial maps of the journey of electrons from optical excitation to relaxation. We will further review other well-known material characterization techniques such as optical microscopy, electron microscopy, scanning probe microscopy, and Raman imaging. We explore tBLG as a prototype beyond optical absorption and Raman studies using the developed TA microscopy approach. Our work represents the first time-domain study of a stacked and twisted 2D system, tBLG. We apply TA microscopy approach on tBLG in Chapter 4 and Chapter 5 to test the conflicting model we describe in Chapter 3 and to understand the nature of the hybridized electronic states. This dissertation provides a framework to understand the nature of

interlayer electronic states and many body effects in tBLG that can be extended to other 2D materials and their heterostructures with or without rotation between layers.

In this first Chapter, we will review the current standing of 2D materials, their structure, methods of acquiring 2D materials, material transfer to a substrate and creating heterostructures with artificial transfer process or CVD growth.

1.2 2D Materials

2D materials are a class of crystalline materials with one or two atom thickness. This class of material has been aggressively developed due to their unusual characteristics for fundamental research as well as device applications. They consist of

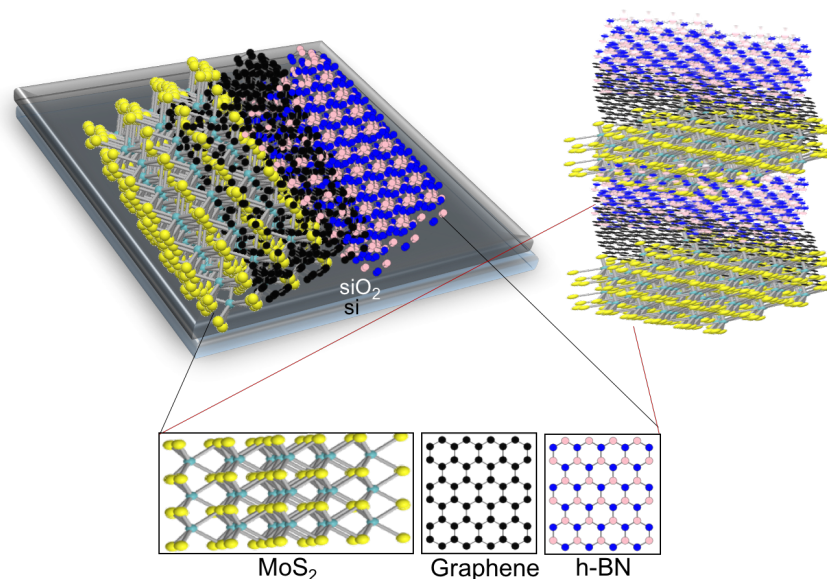


Figure 1.1: Typical 2D vdW layered lateral and vertical heterostructure. Weak vdW forces allow separation of individual sheets from 2D materials such as MoS₂, graphene, h-BN. They can be stacked on top of each other or next to each other to create vertical and lateral heterostructure respectively. The angle rotation between layers provides an extra degree of freedom to modify electronic properties.

sheets that are held together by strong covalent bonds out of the plane and weak vdW forces for in-plane bonding between the sheets. They do not have any reactive dangling bonds making it stable under ambient conditions. The combination of different 2D layer stacking is called vdW heterostructures. Such a 2D vdW layered lateral and vertical heterostructure composed of MoS₂, graphene and h-BN is shown in Figure 1.1. Restriction of size in one or more dimensions changes some electronic properties of the material. The 2D material has different optical and electronic properties from its bulk counterpart due to confinement of electrons as well as the lack of interlayer interactions. Mechanical and chemical properties are also different from its counterpart due to high surface-bulk ratio. Since the discovery of graphene, extensive research on these materials has grown rapidly all over the world.

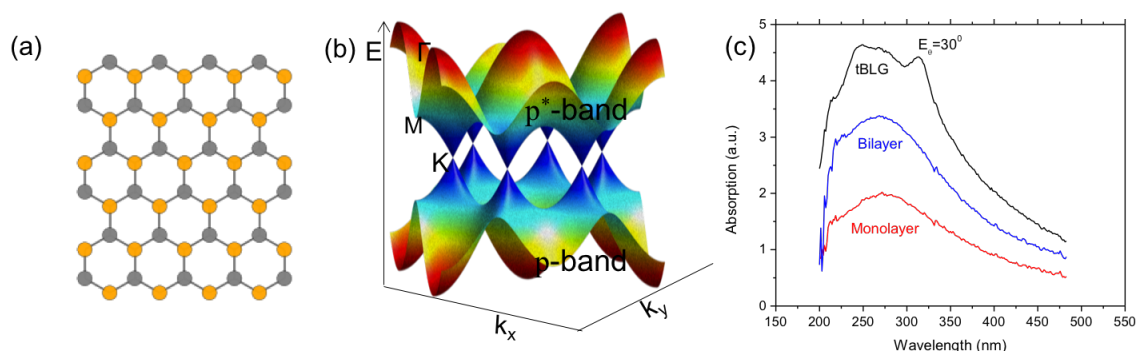


Figure 1.2: Graphene. (a) Honeycomb lattice of graphene with two distinct atoms per unit cell. (b) Tight binding approximated electronic band structure of graphene showing 6 Dirac cones in the k -space. (c) Optical absorption spectrum of graphene, bilayer graphene and tBLG. A peak at 290 nm is visible due to saddle point exciton, an additional peak at ~ 307 nm appears in tBLG that is tunable with angle between the two layers.

2D materials hold great promise due to their desirable properties and freedom to control the physical properties via stacking as shown in Figure 1.1. Currently, there are

many known 2D materials with different electrical and optical properties. They are known for exceptional properties such as lightweight, flexible and good conduction of heat and electricity. Recent 2D materials research holds exciting promise for potential revolutionized applications in transistors, solar voltaic technology, sensors, flexible displays and more.

Since its Nobel Prize winning discovery, Graphene has been the most popular 2D nanomaterial. It is a semimetal with a single atom sheet of carbon atoms arranged in a hexagonal lattice as shown in Figure 1.2a. It attracted huge attention due to its exceptional electronic properties. This dissertation primarily focuses on graphene, twisted bilayer graphene in particular. The tight binding approximated electronic band structure of graphene is shown in Figure 1.2 highlighting the unique Dirac cones in the k space.

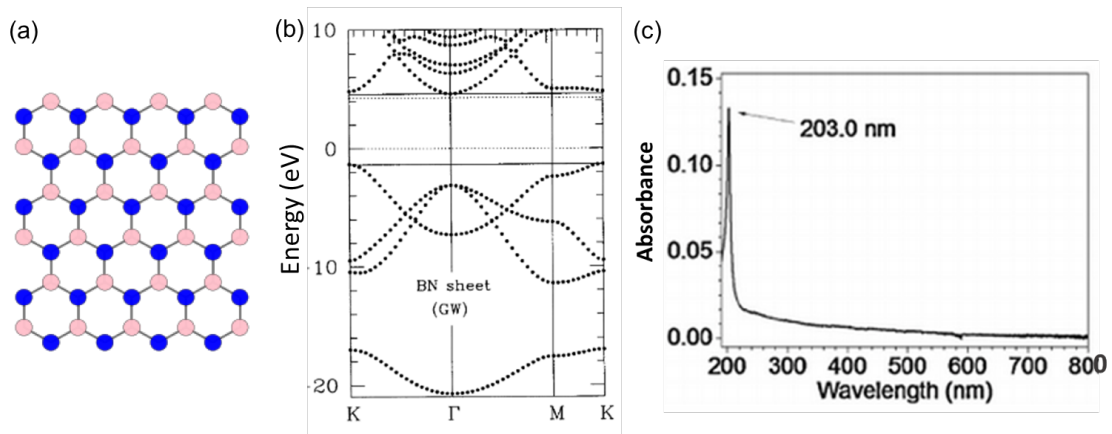


Figure 1.3: Hexagonal boron nitride. (a) Atomic structure of h-BN with hexagonal Lattice with alternating boron and nitrogen atoms. (b) h-BN electronic bandstructure calculated with GW approximation. It shows a large bandgap of 5.97 eV.⁹ (c) Optical absorption spectrum of h-BN on a quartz substrate showing strong absorption at 203 nm corresponding to the optical band gap of 6.02 eV.¹⁰ [Adapted from ^{9,10}.]

Its optical absorption spectrum shows 2.3 % absorption in the visible spectrum range as presented in Figure 1.2c.¹¹ Upon stacking and twisting two graphene sheets, an additional absorption peak appears (Figure 1.2c) that is not present in a single layer or bilayer graphene. The energy of this absorption peak is tunable with the stacking angle as discussed further in Chapter 2, 3 and 4.

Other 2D materials recently have been extensively studied and are being developed. Some of the examples are insulating boron nitride; semiconductor, metal and superconductor family of transition metal dichalcogenides; XY_2 with X for Mo or We and Y for S, Se, Te. Hexagonal boron nitride is an insulator with carbon atoms in graphene are replaced with alternate boron and nitrogen atoms for h-BN as shown in the atomic structure in Figure 1.3a. It is an insulator with a bandgap of ~ 6 eV as shown in the band structure (Figure 1.3b) and an absorption spectrum (Figure 1.3c). h-BN is typically used

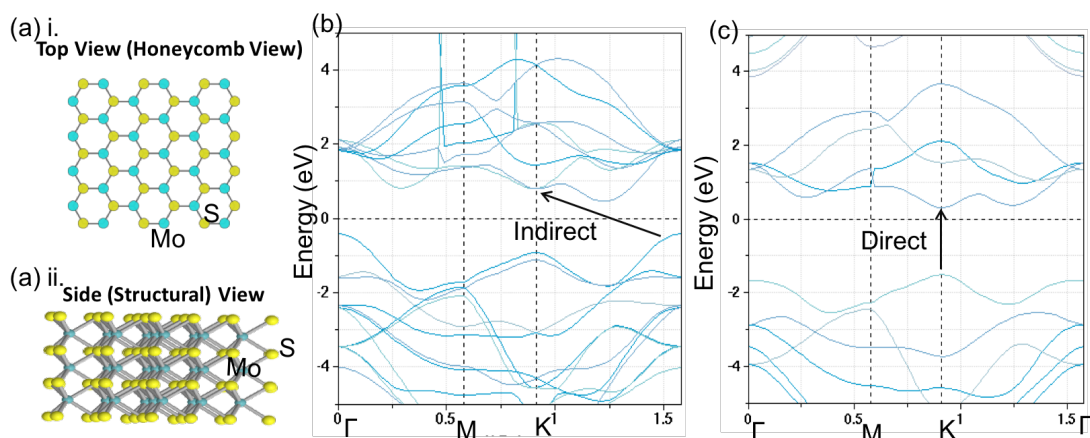


Figure 1.4: MoS₂. (a) (i) Top view of atomic structure of MoS₂ showing honeycomb structure like graphene. (ii) Side view of the lattice structure showing two atoms involved in a single layer material. (b) Electronic band structure with tight binding approximation of bulk MoS₂, indirect band gap is highlighted. (c) Indirect band gap becomes direct band gap for a single layer material from quantum confinement.

to protect 2D materials from the environment. From the transport perspective, it has been demonstrated that highest mobility graphene transistor can be obtained by encapsulating graphene with h-BN.¹²

The family of 2D material TMDs is composed of three atoms. The chemical composition of some TMDs is XY_2 with X as a metal atom Mo, W, Cr, Co, Ni, Ta is shown in Figure 1.4a i, ii. TMDs offer distinct electronic properties. In particular, some of the indirect band gap bulk TMDs turn into a direct gap semiconductor going from bulk to single layer as shown in the Figure 1.4b-c for MoS_2 as an example.¹³

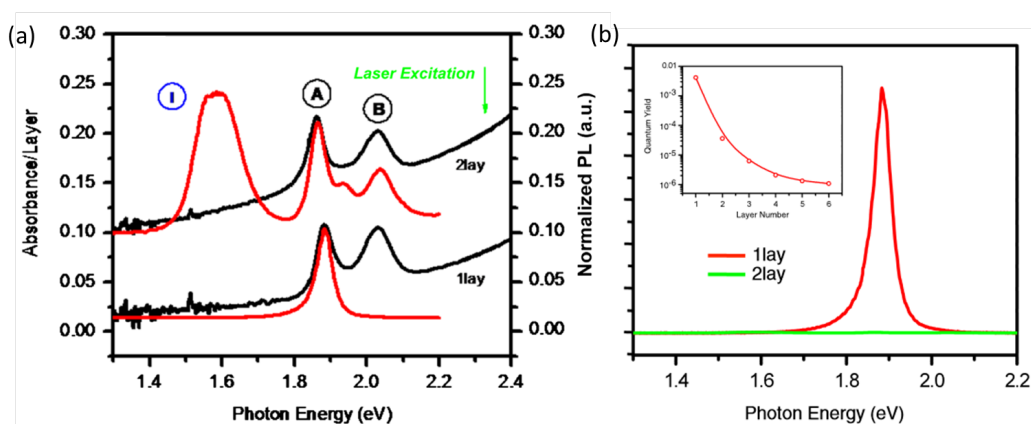


Figure 1.5: Absorption and photoluminescence spectrum of MoS_2 . (a) Absorption spectrum of MoS_2 shows 10% absorption per layer on resonance. (b) Photoluminescence spectrum of MoS_2 .¹³ [Adapted from¹³.]

Absorption and photoluminescence spectra of MoS_2 are shown in Figure 1.5. There are multiple excitonic peaks seen in the absorption spectrum labeled A, and B in Figure 1.5a. For a single layer material, A-exciton is dominating the absorption with 10% absorption of the incident light. Since single layer material has a direct bandgap transition, huge PL is observed (Figure 1.5b) for single layer vs. bilayer suggesting bound exciton formation.

There are many layered materials besides TMDs, such as monochalcogenides GaSe, monoelemental semiconductors such as silicone, phosphorene, germanene and MXenes.¹⁴ Many of these materials are stable at ambient conditions, and researchers have found strategic handling procedures for the materials that are not stable.¹² Mechanical exfoliation and chemical or solvent assisted exfoliation has been the primary method of material synthesis. This process gives nanosheets as the vdW interactions between the layers are inherently weak and can be broken. Many of these materials can be synthesized by chemical vapor deposition on a wafer scale with a high degree of control over structure, defects, composition and physical properties.

Graphene, hexagonal boron nitride, TMDs and other 2D materials have been widely used as channels in field-effect transistors and valleytronics for fundamental studies. Carbon based materials such as graphene are mostly being used as a low-cost catalyst for renewable energy production and storage. True potentials of these 2D materials may arise by stacking them layer by layer in the desired sequence creating a novel 3D material with entirely new properties and functionality.¹⁴

1.3 Methods of Obtaining 2D Materials

There are several methods for preparation of 2D materials. Out of those, micromechanical exfoliation, liquid exfoliation, and CVD growth are primarily being used to acquire single layers and few layers of 2D material samples.

1.3.1 Micromechanical Exfoliation

The first reported single layer 2D material, graphene was prepared by Novoselov and Geim with the scotch tape exfoliation method.¹⁵ This technique is shown in Figure

1.6. In this technique, single layer material is detached from a bulk crystal using adhesive tape. After peeling it off the bulk crystal, due to weak vdW interactions between layers, multiple layer material remains on the tape (Figure 1.6a). Upon repeated peeling, the multilayer material is cleaved into many few layer flakes (Figure 1.6b-c). Afterward, the tape is attached to the substrate transferring most of the material on it (Figure 1.6d-e). The substrate with the material on is then inspected under the optical microscope to locate few and single layer pieces of material (Figure 1.6f).

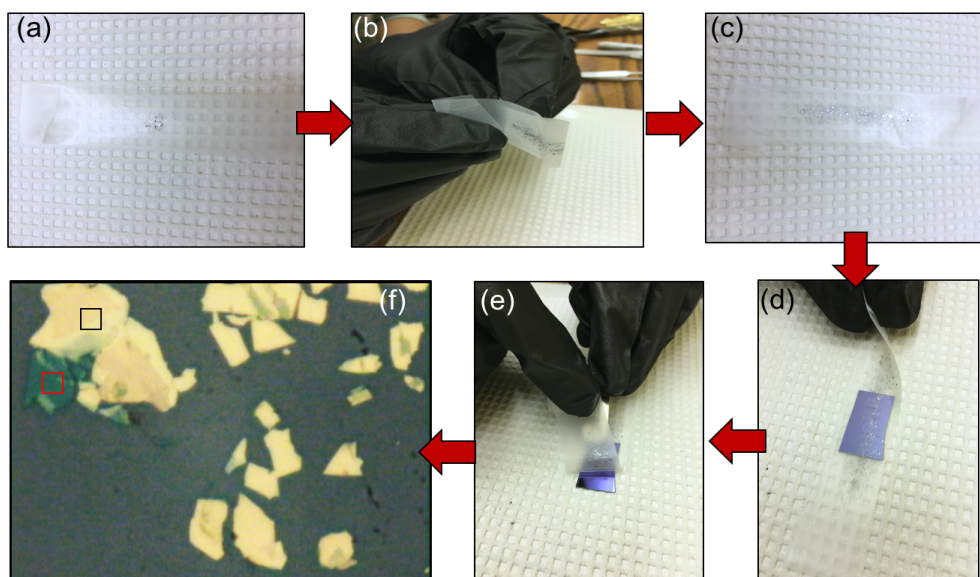


Figure 1.6: Mechanical exfoliation process. (a-f) (a) Material to be exfoliated is placed on a piece of adhesive tape, (b) the tape is repeatedly peeled off on itself to disperse the material that looks like (c), the tape is then pressed onto the substrate and, (e) then peeled off, (f) the substrate with exfoliated layers is taken to the optical microscope for inspection. Multilayer pieces can be seen with highlighted thick (black) and thin (red) pieces based on the optical contrast.

The transferred few and single layer flakes differ significantly from the shape and thickness with the size anywhere from nanometers to few tens of micrometers for a single

layer piece. It is possible to identify single layer flake with optical contrast due to the interference effect on Si/SiO₂ substrate under the microscope (Figure 1.6f).¹⁶ This technique is relatively straightforward, and the quality of single layer pieces produced with this method is very high with very low defects. However, it is difficult to produce large size flakes and finding single layer pieces is labor intensive.

1.3.2 Liquid Exfoliation

Due to low yield of the mechanical exfoliation process, extensive research has been carried out to solve the production rate. One of the solutions is the liquid exfoliation method to get large quantities of dispersed nanosheets. The schematic of liquid

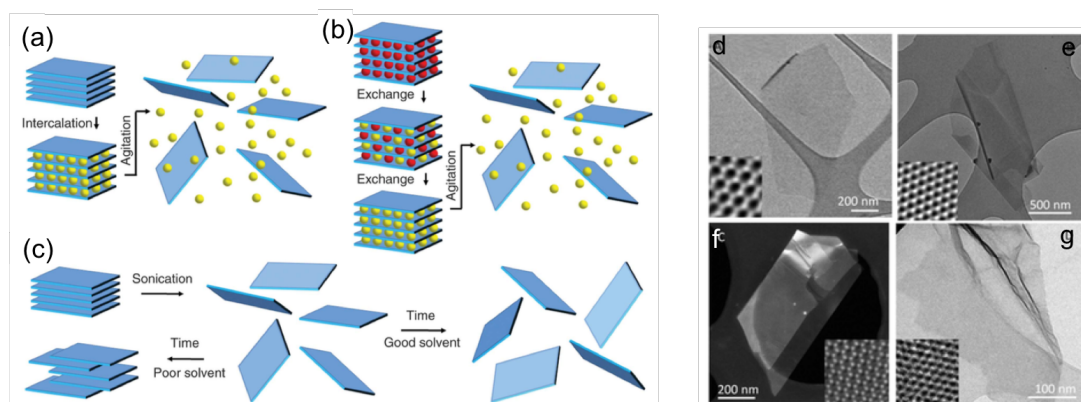


Figure 1.7: Schematic of liquid exfoliation process. (a) Between the layers of 2d material ions are intercalated. This weakens the interlayer interactions. (b) In the case of ions present between the layers; they are exchanged with other ions. (c) 2d material is sonicated in a solvent to create nanosheets. (d)-(g) TEM images of nanosheets through liquid exfoliation process: (d) A graphene nanosheet with sonication exfoliation, (e) An h-BN nanosheet with sonication exfoliation, (f) A MoS₂ nanosheet exfoliated with sonication process, (g) A MoS₂ nanosheet Exfoliated with ion intercalation. [Adapted from¹⁷.]

exfoliation process and TEM images of graphene, h-BN, MoS₂ nanosheets with sonication and MoS₂ nanosheets with an intercalation exfoliation process is shown in Figure 1.7. This is a scalable technology for bulk manufacturing. There are multiple methods such as sonication in the surfactant solution, in solvents, in polymer solutions, ion intercalation, and polymer intercalation for obtaining liquid exfoliated nanomaterials. One sonication method is more efficient than others for a specific family of 2D materials.¹⁵

One of the oldest methods is oxidation followed by dispersion into suitable solvents. The treatment with oxidizers, hydroxyl and added epoxide groups makes the material hydrophilic. This treatment allows water intercalation and exfoliation into single and few layer nanosheets upon ultrasonication (Figure 1.7a-c).¹⁷ They can be stabilized against reaggregation with the addition of negative surface charge with surfactant or polymer. This process is primarily used for production of graphene which largely produces single layer sheets with hundreds of nanometers across as seen in the TEM image (Figure 1.7d).¹⁸

Another most widely used technique uses guest molecules adsorbed into the spacing between layers forming inclusion complexes. The ionic species increases layer spacing, which then decreases the interlayer adhesion between layers making exfoliation easier (Figure 1.7a-c). After which, thermal shock or ultrasonication accomplishes the exfoliation process. The produced nanosheets are stabilized by a surface charge or surfactant. This method is primarily used for graphite and TMDs. Nanosheets produced by liquid exfoliation can be drop cast on a substrate or used as produced. Most of the materials produced are stable in ambient condition.^{18,19} Glove box and vacuum chambers

are widely used for unstable compounds for preparation and storage. Liquid exfoliation technique is a scalable route for the production of 2D nanomaterials. This process can be useful for large area electronics through techniques like inkjet printing.

1.3.3 Chemical Vapor Deposition

Chemical vapor deposition (CVD) process was first used in 1897²⁰ to deposit tungsten onto carbon filament lamps using hydrogen. Since, then it has been extensively adapted to produce high purity materials such as Ta, Ti, Si and many more. Modified CVD method has been currently used for mass production of high purity polycrystalline silicon, which is essential to obtain single crystal Si. This technique has been considered a reliable method to study fundamental physics as well as applications for zero-dimensional material such as quantum dots, one-dimensional material such as carbon nanotubes, and two-dimensional materials such as graphene, TMDs, and others. There are some drawbacks of mechanical exfoliation technique and liquid exfoliation method for acquiring 2D materials. Mechanical exfoliation method of acquiring single and few layers material from bulk gives high-quality material. However, it is limiting in size and not efficient. Liquid exfoliation method on the other hand is efficient, but the final product has low quality and limited in the small size of single and few layer sheets. CVD technique has been used as a reliable process due to control over the process with much better quality than liquid exfoliation process, and higher efficiency compared to mechanical exfoliation process.

The majority of elements in the periodic table have been deposited with CVD for a pure element deposition or combination of elements to form compounds. This

technique is mostly used for applying a solid thin-film coating on surfaces as well as producing high purity bulk material.

In a simplest CVD method, one or more heated objects are placed in a chamber, and precursor gases flow into the chamber as shown in the schematic of graphene growth on a Cu substrate with a methane precursor in Figure 1.8. On or near heated surfaces, chemical reactions occur which results in a thin film coating on the surface. This is followed by draining out the chemical by-product and unreacted precursor gases.

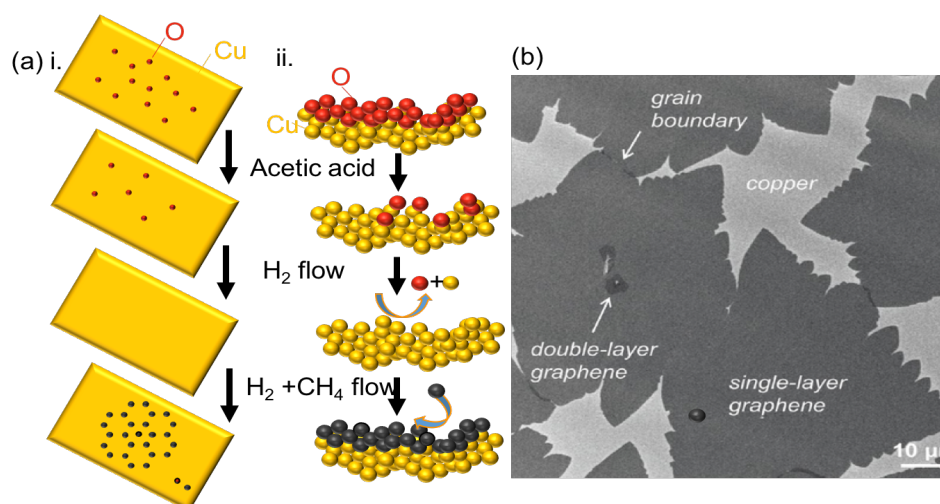


Figure 1.8: CVD synthesis mechanism. (a) Schematic of CVD growth process of graphene on copper substrate²¹. (b) Partially grown CVD grown graphene on copper imaged with SEM. Single layer graphene, double layer graphene, and grain boundary are visible.²² [Adapted from^{21, 22}.]

The precursors, environmental conditions, substrates, and catalysts are most critical parameters in determining the quality of a grown material. In the 2D material community, tremendous efforts are made towards achieving improved quality, large domains and efficiency for single and few layers 2D material growth. Copper or Ni is found to be the

best substrate for CVD growth of graphene, and h-BN. Various substrates such as Si/SiO₂, glass, quartz, LiF, MgO, mica, Mo, Au, Pt, Al, Cu, steel have been used for TMD material growth process.²¹

This dissertation mainly focuses on CVD grown graphene and twisted bilayer graphene. CVD method provides large domains, high quality single and few layer material. As an example, SEM image of CVD grown graphene is shown in Figure 1.8b. This process also produces complex 2D structures such as heterostructures with and without twist between two layers as discussed later in Section 1.4.3. It has been shown that for some growth parameters, CVD method produces a mixture of the single layer, bilayer, and twisted bilayer graphene domains. For this dissertation, we used as-grown CVD twisted bilayer graphene or artificially transferred tBLG. For each case, a slightly different CVD growth process was used.

For the as-grown CVD tBLG, randomly oriented graphene growth method reported by Li et al.²³ was used. Cu foil (Alfa Aesar, 25 μm thick, 99.8 % purity, item no.13382) was cleaned in acetic acid for 10 minutes before inserting into an evacuated furnace with a base pressure of 6 Torr. In 100 sccm hydrogen, the Cu foil was then annealed at 1000°C for 10 minutes followed by 10 minutes airgas, ultra-high purity (UHP) 300, 10 sccm methane and airgas, ultra-high purity (UHP) 300, 100 sccm hydrogen flow over the foil for graphene growth. The grown tBLG was then transferred to a desired substrate as discussed in Section 1.4.1.

In randomly oriented graphene growth, tBLG is a byproduct. However, the films are usually small limiting potential scalable applications. Moreover, small angle tBLG is rare in as-grown sample because it is close to energetically stable form, Bernal stacked

bilayer graphene. Due to better electron-hole symmetry in small angle tBLG, part of this dissertation is focused on exploring the nature of hybridized states due to interlayer interactions between two layers in small angle tBLG. Small angle tBLG can be obtained by scanning significant amount of as-grown CVD graphene, searching in accidentally folded exfoliated graphene samples, or intentionally folding graphene with AFM tip. These methods do not provide any control or scalable options; they are rather time intensive and ineffective.

On the other hand, aligned graphene growth produces large crystalline alignment of single layer graphene, which can be cut into pieces and then stacked to make tBLG configuration of the desired angle as well as heterostructures. This method holds promises for scalable aligned graphene growth with large domains. In this growth process, the Cu foil (Nilaco corporation, #CU-113213, 99.9 % pure) is annealed in a hot-wall quartz tube furnace for up to 12 hours under hydrogen (airgas, UHP 300, 100 sccm) and argon (airgas, UHP 300) flow with a pressure of 26 Torr. Under dilute methane (airgas, 1% CH₄ in H₂, 6 sccm), hydrogen (airgas, UHP 300, 30 sccm) and argon (airgas, UHP 300) flow at 1030°C with 26 Torr of pressure, partial graphene can be grown in 45 minutes and full coverage graphene can be grown in 1.5 hours.²⁴ The Cu foil with graphene is cut into two pieces and treated separately for the artificial transfer process to create tBLG as discussed in Section 1.4.2.

1.4 Construction of Heterostructures

1.4.1 Transfer Process of Graphene

There are many techniques to transfer 2D material from one substrate to other. For the scope of this research, the transfer process used is outlined in Figure 1.9. To transfer graphene grown on Cu to a desired substrate such as Si/SiO₂, fused silica or SiN,

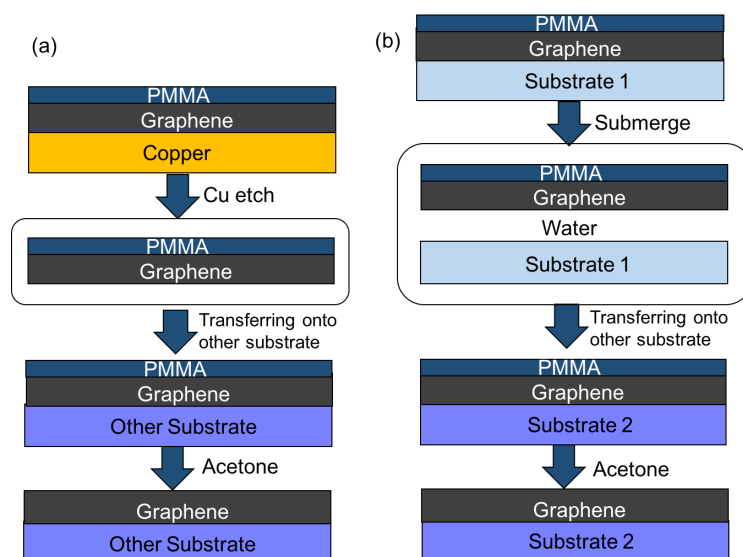


Figure 1.9: Graphene transfer process. (a) CVD grown graphene is transferred to a substrate. (b) Graphene from one substrate is getting transferred to another substrate.

Cu with graphene is covered with a thin spin coated Poly (methyl methacrylate) (PMMA, 495 K, 4% in anisol) followed by etching of Cu in saturated ammonium persulfate solution overnight. Multilayer graphene covered with PMMA is then rinsed multiple times in an ultra-high purity (UHP) water bath before transferring it to the desired substrate such as Si/SiO₂, fused silica or SiN. The sample with graphene/PMMA is then annealed in air at 350°C for 5 minutes and washed in acetone/IPA for PMMA removal.

For a better electronic coupling between the layers, the sample is then annealed in air at 350°C for 10 minutes. To transfer graphene from one substrate to another, cover graphene on substrate 1 with spin coated PMMA and then submerge it in water as shown in Figure 1.9b. Graphene with PMMA will float on water, scoop it with substrate 2. Follow the same procedure as earlier to remove PMMA.^{25,26}

1.4.2 Artificial Transfer Process to Create 2D Heterostructures

Randomly oriented CVD growth process for graphene produces tBLG as a by-product. Another way to create tBLG is to stack two single layer graphene pieces artificially with a desired rotation between the two layers. This process is referred to as artificially transferred graphene process.

The schematic of the process is shown in Figure 1.10. For the scope of this research, the following method is used. The process starts with aligned CVD grown graphene on a Cu substrate that is cut in half. Both pieces are treated separately. The first Cu/graphene piece is placed on a custom built stage system with the graphene surface facing up. The second Cu/graphene piece is prepared with a spin coating of PMMA followed by a thermal release tape with a hole in the center exposing the Cu/graphene/PMMA. Cu/graphene/PMMA/thermal release tape is then treated in saturated ammonium persulfate solution overnight for Cu etching followed by rinsing multiple times in an ultra-high purity (UHP) water bath and a gentle air blow dry. The resultant graphene/PMMA/thermal release tape is placed graphene side down above the first Cu/graphene piece on a custom-built stage holder. Upon applying the negative pressure between the first and the second layer, the two layers start to approach closer.

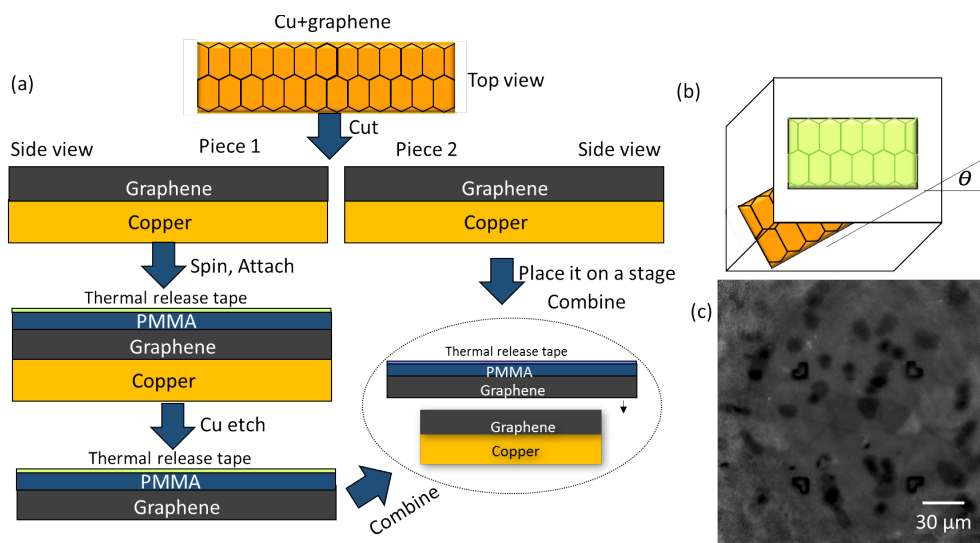


Figure 1.10: tBLG artificial transfer process. (a) Starting with CVD aligned graphene growth, cut a copper piece with graphene in half. Treat both pieces separately; combine them for the final step rotating one piece with respect to the other. (b) Final transferred tBLG showing angle between two pieces. (c) Optical image of an artificially stacked tBLG sample.

The manual microscopic angle control can be achieved by looking at the angle between the two copper pieces in the camera while two pieces are approaching closer. Since the two Cu pieces share the same graphene to Cu piece alignment, any range ($0.4 - 30^\circ$) of angle control is relatively easier and angular precision of about 0.2° can be achieved. Gentle heat gun treatment on the top Cu piece is used for better interlayer coupling between two graphene layers. The resultant sample is Cu/tBLG/PMMA/thermal release tape. The stack is heated in air at 120°C for 1 minute to detach the thermal release tape, and then Cu is etched in saturated ammonium persulfate solution overnight. PMMA covered tBLG is then rinsed multiple times in an ultra-high purity (UHP) water bath before transferring it to the desired substrate such as Si/SiO₂, fused silica or SiN. Once

tBLG/PMMA is transferred on the desired substrate, it is then annealed in air at 350°C for 5 minutes and then washed in acetone/IPA for PMMA removal. In the final step, the sample is annealed in air at 350°C for 10 minutes to increase coupling between two layers. This technique holds great promise since heterostructures of 2D materials can be prepared with the modified version of this procedure.

1.4.3. Vertical and Lateral Heterostructure Formation with CVD Growth

Recently, heterostructures based on single layer TMDs and graphene based materials are attracting enormous attention. First principle simulations predict that particular type-II band alignment of single layer TMDs heterostructures are useful for optoelectronics, photovoltaic, and energy conversion technology.²⁷ First principle simulations also predict that single layer TMDs and graphene heterostructures could achieve 1% power conversion efficiency.²⁸ There has been a tremendous effort made towards making heterostructures with a combination of single and few layers TMDs, graphene, h-BN and other 2D materials. In most cases, these heterostructures are prepared with either exfoliation or CVD growth process followed by a transfer process described in Section 1.4.1, and 1.4.2.

Different 2D materials can be grown together on the same substrate and stitched together to form a continuous film. This requires the two materials to have similar structure and lattice constants such as graphene and hBN, or materials from the TMDs family. Lateral heterostructures hold promise in controlling the dopant density and potential p-n junction fabrication within the same 2D film. It has been shown that under certain growth conditions, some of these lateral heterostructures can be stitched together with atomic precision.²⁹⁻³³ Lateral and vertical heterostructures can be produced by

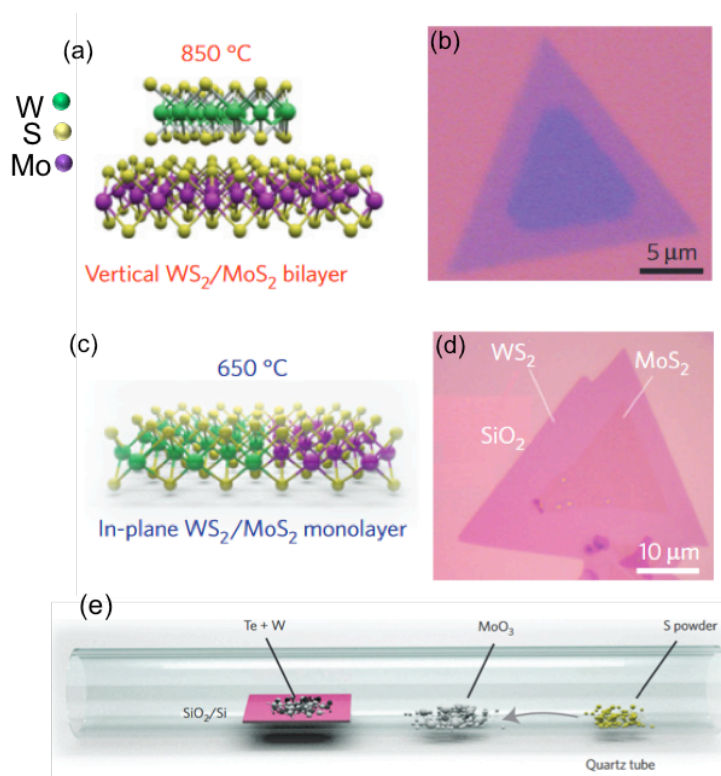


Figure 1.11: Vertical and in-plane heterostructure growth process of WS₂/MoS₂. (a) Schematic of vertical WS₂/MoS₂ growth at 850° C. (b) Optical image of vertical heterostructure showing triangle shape crystals of WS₂ and MoS₂. (c) Schematic of in-plane WS₂/MoS₂ growth at 650° C, (d) Optical image of the vertical heterostructure. WS₂ and MoS₂ can be identified with optical contrast. (e) Schematic of the heterostructure synthesis process. [Adapted from³⁴.]

sequentially vaporizing two different compounds as shown in the schematic in Figure 1.11e. The first precursor is flown through for the growth of first material and then the second precursor for the second material growth is introduced before the first precursor covers the entire substrate. As shown in the Figure 1.11, Gong et al. verified vertical and in-plane heterostructure growth of WS₂/MoS₂. Huang et al. demonstrated the lateral heterostructure growth MoSe₂-WSe₂ via vaporization and deposition of a mixture of

MoSe₂ and WSe₂ with UHP H₂.³¹ Duan et al. demonstrated WS₂-WSe₂ lateral heterostructure by sequentially vaporizing and depositing WS₂ and WSe₂ at atomic pressure, Ar flow under high temperature.³² They applied a similar growth strategy for MoS₂-MoSe₂ lateral heterostructures where they used MoO₃ as a precursor of Mo and then S and Se powders were sequentially vaporized to react with MoO₃ to produce MoS₂-MoSe₂ heterostructures. This technique holds great promise since heterostructures from most of the 2D materials that can be prepared with modified versions of this procedure.

1.5 Summary and Outlook

In this Chapter, we introduced graphene and other 2D materials. We discussed their structure, properties, methods of acquiring them, and transferring from one substrate to another and potential applications. We discussed that tBLG is most often produced as a by-product of CVD growth process. Alternatively, two aligned graphene sheets can be stacked together at an arbitrary angle with the artificial transfer process. This dissertation will discuss the underlying physics of interlayer electronic states in tBLG as a model system for 2D heterostructures.

In **Chapter 2**, we describe the ultrafast confocal TA microscopy approach we developed to map out the electron population in a single grain of material with micron spatial and femtosecond (fs) time resolution. This method will help map homogeneity, charge transfer, time dynamics, and many body interactions to figure out the potential feasibility and efficiency of devices built from the 2D material. We explain the interlayer electronic band structure of tBLG in **Chapter 3** where we end up with two conflicting models; free electron model and bound exciton model. To test the conflicting models, and

to understand the nature of the hybridized interlayer electronic states, for the first time we apply multi-photon TA microscopy approach in **Chapter 4**. Our results of electronic relaxation bottleneck and existence of dark states are best explained by the bound exciton model, which generally holds for other 2D materials and their heterostructures. To map out the exciton binding energy of excitons in tBLG, we use near-IR excited state absorption (ESA) experiment in **Chapter 5**. We measure the relatively large binding energy on the order of $\sim 0.5\text{-}0.8$ eV which is comparable to other excitonic 2D materials such as TMDs. We also observe photoluminescence (PL) emission for the first time from tBLG using 2-photon PL microscopy approach in **Chapter 5**. The measured exciton binding energy with the 2-ph TA, ESA experiment, and 2-ph PL experiment agree with each other, and they agree with the theoretically predicted value. In **Chapter 6**, we conclude our findings and discuss future directions towards applications to advance technology. We believe that tBLG can make an efficient energy harvesting device since it is a first hybrid 2D material which has high mobility owing to graphene's continuum states as well as bound exciton states from interlayer hybridization. We also discuss helicity dependent optical properties of tBLG for valleytronic devices. We conclude by explaining how we can intelligently engineer 2D heterostructures using tBLG for efficient devices that have potential to augment the landscape of materials used in solar-energy and device sensing technology.

2. IMAGING AND CHARACTERIZING 2D MATERIALS

2.1 Introduction

To study the structure and material properties of the 2D class of materials discussed in Chapter 1, including tBLG, imaging techniques are essential to visualize the defect concentration and structural variation. In this Chapter, we will review various techniques that have been developed to characterize by many groups in the 2D community. Many of these techniques have been adopted as standard imaging techniques including optical microscopy, electron microscopy, scanning probe microscopy, and others. Each of these methods provides a different type of information about the material. As a consequence, a combination of these techniques is typically necessary to acquire complete information about the material properties. These methods have been successfully applied to many 2D materials. However, for the scope of this study, we will primarily discuss these methods for imaging graphene and tBLG. We will also discuss techniques that have been developed by our group and our collaborators, including ultrafast confocal transient absorption (TA) microscopy and spectroscopy, photoluminescence microscopy, hyperspectral microscopy, wide-field Raman microscopy and dark-field transmission electron microscopy.

For the scope of this research, in tBLG characterization, we have employed a combination of imaging techniques, such as TA microscopy, hyperspectral imaging, and dark-field transmission electron microscopy. We have applied TA microscopy approach in Chapter 4, 5, appendix A, and 2-ph PL microscopy in Chapter 5. We will briefly discuss a novel technique we are developing based on C-AFM to measure space-time

(nm-fs) resolved photocurrent generation in 2D materials by combining AFM with a fs pulsed laser source.

2.2 Optical Microscopy

Optical microscopy was invented before the 18th century. It is a traditional form of imaging tool that is widely used still today. In the simplest form, this technique is used to closely view a sample through the magnification of a lens with a visible light source. Using this technique, rapid imaging of large scale samples is possible. Moreover, this method doesn't require special sample preparation and does not cause any damage to the sample. Through either reflection or transmission based optical microscopy, the light interacts with the sample, which results in spectroscopic information about the specimen's electronic and vibrational properties. Data acquisition is usually done at ambient condition and typically easier to interpret.

One drawback of optical microscopy is the limitation of spatial resolution. The spatial resolution is limited to the wavelength of light which is about few hundred nanometers for visible light. This resolution is not sufficient to study crystalline structure such as defects and grain boundaries. Nevertheless, it has been widely used for basic sample examination.

Optical microscopy has been proven a useful tool for determination of a number of layers by looking at the contrast for 2D materials like graphene and TMDs. To increase the interference effects in order to increase the contrast and make the layers visible by eye upon shining visible light on the sample, an appropriate oxide thickness on silicon can be used. This allows rapid identification of single and few layers of 2D

materials on a large scale. This technique was used for identification of single and few layer graphene after exfoliation when it was first discovered in 2004 to increase the contrast up to 10% because it is challenging to identify the number of layers by eye under the optical microscope since it absorbs 2.3% of visible light for a broad spectrum range.³⁵

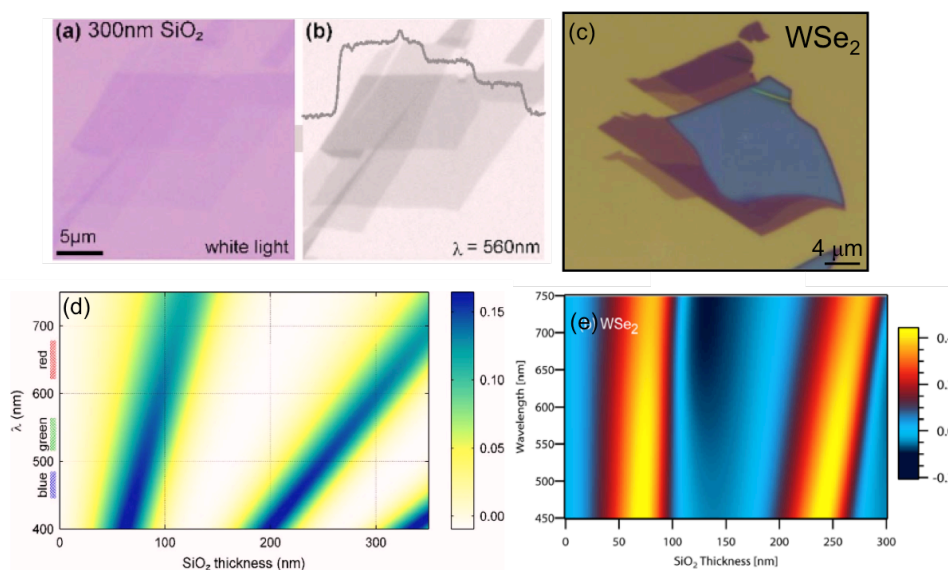


Figure 2.1: Graphene and WSe₂ optical imaging. (a) Exfoliated graphene on 300 nm SiO₂ illuminated with white light. Single and multilayer graphene is visible.³⁶ (b) Same sample is illuminated with 500 nm light. Multilayer and monolayer graphene is still visible.³⁶ (c) White light illumination on WSe₂ transferred on 270 nm SiO₂ thick substrate showing single and multilayer³⁷, calculated color plot of contrast as a function of wavelength and SiO₂ thickness for (d) Graphene,³⁶ (e) WSe₂, for both, 50-100 nm, 200-250 nm thick SiO₂ gives the best contrast.³⁷ [Adapted from ^{36,37}.]

As shown in Figure 2.1, for a given wavelength illumination, a particular oxide thickness creates the optimal contrast to identify the number of layers and thickness. This information can be further extended to identify other 2D materials by looking at specific material properties and SiO₂ thickness. This technique has been primarily used for other 2D material inspection to look for desired thickness of the material after exfoliation.³⁶

Although optical microscopy provides significant information about the shape, size, and homogeneity of the sample, it does not provide information about the crystalline structure. However, by varying the wavelength of light that excites the sample and recording the sample response, it is possible to realize more information about the spectroscopic behavior, material composition, thickness and possible photoemission of the material. This technique is discussed in more details in the following section.³⁸ On the other hand, tools like atomic force microscopy (AFM), scanning probe microscopy (SPM), back-scattered electron microscopy (BSED), angle-resolved photoemission electron spectroscopy (ARPES), and electron microscopy techniques such as transmission electron microscopy (TEM), scanning electron microscopy (SEM) are required to map out materials composition on an atomic scale.

2.3 Hyperspectral Microscopy

When a sample absorbs energy in the form of a photon, it excites an electron, and a transition can occur between two electronic states with the same momentum. The absorption spectrum of a material can be constructed by varying the wavelength of the excitation light while monitoring the sample response also known as optical spectroscopy method. This spectrum essentially corresponds to the density of states. Since insulators, semiconductors, and metals have different electronic bands and the band gap, their absorption spectrum has different signatures. From the absorption spectrum, looking at the photon energy at which the transition between absorbing and non-absorbing occurs, useful information about the band structure over a broad energy range can be measured to determine material composition.³⁹

One atom thick graphene absorbs 2.3% ($\pi\alpha$) of visible and near IR light uniformly due to its band structure as shown in the Figure 2.2.^{11,40} There is a Dirac point where the conduction and valence band meet giving it a linear dispersion relation as illustrated in Figure 2.2, the arrows indicate the optical transitions responsible for absorption (discussed further in Chapter 3). The absorption spectrum of graphene is shown in the Figure 2.2 showing multiples of 2.3% uptake for various layers of graphene.

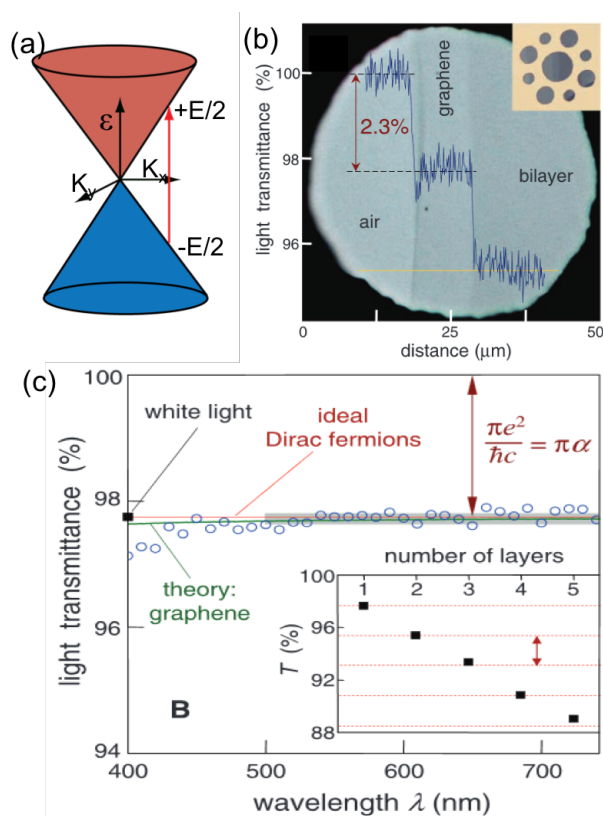


Figure 2.2: Optical absorption spectroscopy in graphene. (a) Optical transitions responsible for absorption in graphene. (b) Light transmission through suspended single and bilayer graphene. (c) Transmittance as a function of wavelength in graphene showing constant value for a visible spectrum range. Inset - decreasing transmittance as a function of the number of layers. [Adapted from¹¹.]

Optical absorption spectroscopy has been primarily used to map out electronic properties of 2D materials. However, this technique is limited to bulk or point measurements lacking the spatial resolution.⁴⁰⁻⁴² On the other hand, hyperspectral absorption technique is based on wide field illumination resulting in a diffraction limited spatial resolution.³⁸ We assembled an optical hyperspectral set up using custom built Horiba fluorimeter and Olympus microscope. This setup not only allows us to measure spatially resolved optical absorption but also spatially resolved photoluminescence of 2D materials.

The schematic of our custom built Horiba fluorimeter is shown in Figure 2.3. It can measure excitation and emission spectrum simultaneously. It can acquire fluorescence measurements at a fixed excitation or fixed radiation energy as well as 3D mapping of fluorescence counts as a function of excitation and emission energy. It consists of a wide spectrum white light source, xenon arc lamp. The light is then directed to an excitation double monochromator that can isolate monochromatic light with desired slit width. This specific wavelength of light then shines on the sample in the sample chamber or coupled to a fiber optic cable into the optical microscope for diffraction limited spatially resolved measurements. For the bulk and point absorption and emission measurements, this fiber optic cable coupling to the optical microscope is not required. In which case, the emitted light from the sample in the sample chamber is directed to the emission double monochromator to map out the emission wavelength selectively. It is then collected by either photomultiplier tube (PMT) or nitrogen cooled InGaAs detector system, which reads out the measured emission counts to the computer.

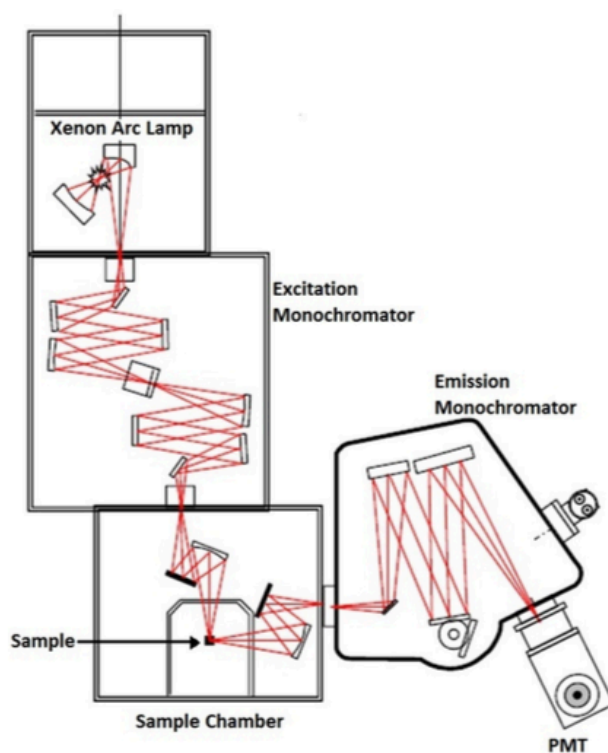


Figure 2.3: Schematic of the Horiba Fluorolog. Xenon arc lamp provides a broadband excitation light source. Double excitation monochromator allows choosing a particular wavelength of light for excitation. The light is incident on the sample in the sample chamber. The emitted light from the sample is directed to double emission monochromator, which is then sent to either PMT for visible detection or nitrogen cooled InGaAs for near-IR detection.

The schematic of hyperspectral microscopy set up is shown in Figure 2.4. For hyperspectral absorption mapping, the monochromatic light from the excitation monochromator is focused with parabolic mirrors into a UV enhanced bifurcated multimode fiber optic cable which is coupled into a modified Olympus BX60M microscope either on the side for reflection based or under the microscope for transmission based measurements. Collimated light from the fiber optic cable is focused onto the sample with a reflective objective (Edmund optics, 52x). All the images are

normalized against the bare substrate to correct for the inhomogeneous illumination on the sample from the fiber as shown in Figure 2.5.

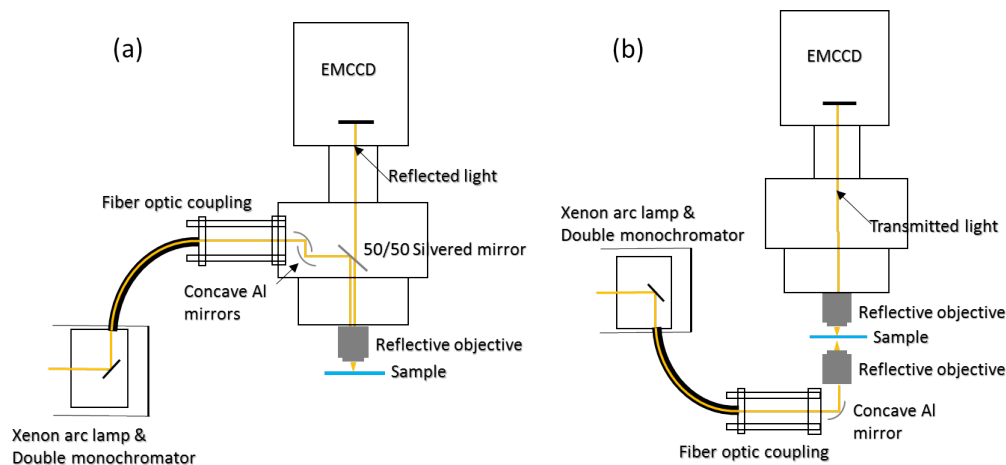


Figure 2.4: Schematic of hyperspectral microscopy. The light from Horiba fluorolog is coupled with a fiber optic cable to the microscope with a cage system assembly. Reflective optics are used to avoid chromatic aberration, EMCCD captures the signal. (a) Reflection based set up. (b) Transmission based set up.

This set up is designed for both reflection and transmission based measurements. For reflection based measurements, the monochromatic light through the fiber optic cable goes through a 30/70 beamsplitter through a cage system on the side of the microscope directing the light towards the objective focusing it on the sample. The reflected light from the sample is then directed back through the objective and the beamsplitter towards the detection system. In the transmission based measurements, the fiber optic cable couples to a parabolic mirror into a reflective objective below the sample as shown in Figure 2.4 acting as a condenser. The transmitted light through the sample is then directed to the beam detector system through a reflective objective. For both modes, all the optics between the fiber, sample, camera, and objectives are reflective based to

prevent dispersion and preserve microscope focus for a given wavelength eliminating chromatic aberration. In both cases, the light from the sample is focused onto a 512x512,

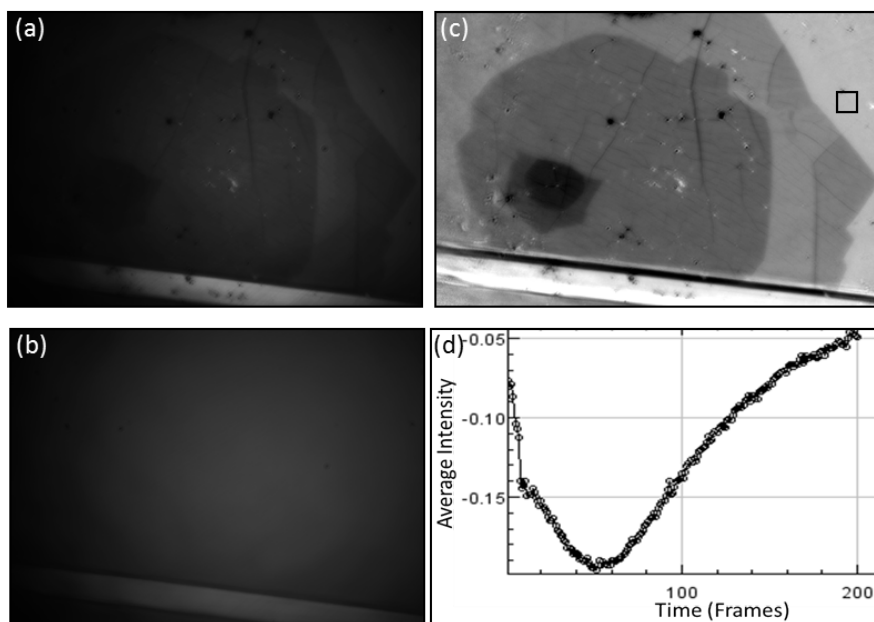


Figure 2.5: Data processing of hyperspectral images. (a) Snapshot of a CVD grown graphene sample with 300 nm illumination. (b) Image of a substrate for the same illumination as (a). (c) Sample image in (a) subtracted from and then divided by substrate shown in (b). (d) Image j snapshot of intensity as a function of number of frames for the highlighted area in (c).

16 μm , pixel sensor (QE 95%) electron-multiplying CCD (EMCCD) for detection (Princeton Instrument eXcelon3, 512 B). This provides most sensitive detection of a single photon that is incident on the sensor due to electron multiplication process. For dark noise reduction, a thermoelectric cooler is used to cool the camera to -70°C . This camera allows detection range of 300 – 1100 nm. Appropriate optical filters are used for the excitation to eliminate second order diffraction from the monochromator. This set up is also used for spatially resolved photoluminescence spectroscopy by inserting

appropriate optical filters before the EMCCD camera. For a point illumination after identifying the region of interest, sending the emission light through a bifurcated fiber to the emission monochromator and the detector system either PMT or EMCCD can also be used for PL emission measurements. This is a versatile tool, which can be used to map out absorption as a function of energy as well as emission and excitation photoluminescence as a function of energy with sub-micron spatial resolution.

For absorption measurements, we use differential reflection or transmission, which approximately corresponds to the absorption of the material as shown in equation 2.1. This process requires reflection or transmission measurements from the sample and the bare substrate. For the data processing to get differential reflection spectra and spatial mapping, image processing software ‘image j’ is used. To eliminate fluctuations in x, y and z dimension due to fluctuations from the diffuser and different output power for the different wavelengths respectively image of the sample needs to be divided by the image of the bare substrate after the dark count subtractions from the image of the sample and the substrate. The resulting normalized image is shown in Figure 2.5.

$$\frac{\Delta R}{R} \cong \frac{I'_{abs} - I_{abs} - I_{dark}}{I_{abs}} \dots\dots\dots 2.1$$

This technique is useful to map out thickness, the number of layers and material composition of 2D materials and their complex heterostructures.³⁸ It has been used to identify material composition for the lateral structure of graphene/h-BN, and other 2D material heterostructure devices. It is possible to distinguish two materials based on the optical response in one measurement.³⁸ In stacked 2D materials, due to interlayer interactions, additional optical features from different structures can be observed.^{13,43-48}

One of such examples is tBLG, which is a primary focus of this dissertation. tBLG shows extra optical absorption peaks in UV-NIR spectral region that varies with the angle.⁴⁵⁻⁴⁸ This technique is further useful for imaging tBLG to map out the relative orientation, theta, for two pieces of graphene stacked at an off axis angle.

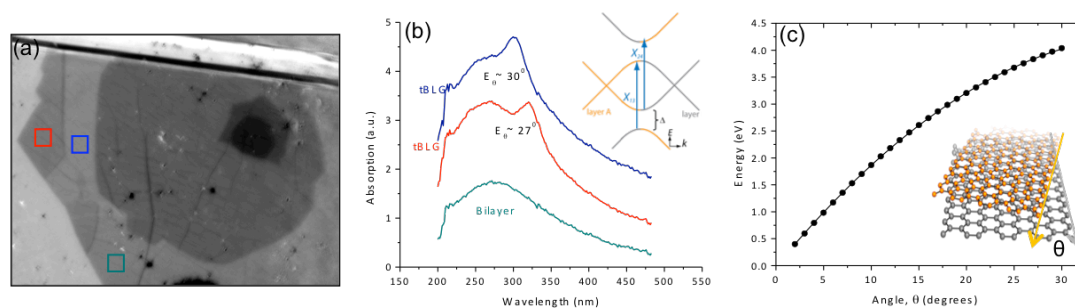


Figure 2.6: Optical imaging of tBLG. (a) Hyperspectral imaging snapshot of CVD grown multilayer graphene at ~ 300 nm illumination. It shows different regions getting dark corresponding to preferential absorption. (b) Absorption spectrum of multilayer graphene regions highlighted in (a). Saddle point exciton effects can be seen near ~ 290 nm. Extra absorption features appear for tBLG domains labeled. Inset - allowed optical transitions for tBLG. (c) Absorption peak energy increases monotonically as a function of the angle between the two layers. Inset - tBLG schematic.

tBLG is a heterostructure of two layers of graphene which can be obtained through CVD growth graphene process or artificially transferred process described in Chapter 1. The interlayer interactions in tBLG force the orbitals to hybridize creating new electronic states, which experience 20% enhancement in the oscillator strength that has been best, interpreted as van Hove singularities. This results in tunable, angle dependent absorption resonances that are not present in single layer graphene or Bernal bilayer graphene as shown in the Figure 2.6. Hyperspectral imaging allows optical identification of angles in tBLG domains with spatial resolution as well as understanding of the

excitonic effects on substrates like Si/SiO₂, SiN, fused silica and so on. This method has a better spatial resolution compared to dark field TEM. However, it has a limiting stacking angle identification range of 5°-29°. ³⁸

Analogous to the optical microscopy, this technique can be used at ambient conditions, without extra sample preparation, with little to no damage to the sample proving useful to examine complex 2D materials. However, this technique is also limited to the diffraction limited spatial resolution providing insufficient atomic structure information of 2D material and their heterostructures.

2.4 Photoluminescence Microscopy

When a material is excited with a photon, the photo-excited electrons jump to a higher lying energy state; these excited electrons relax back to the ground state releasing energy in the form of photons. The light emitted through this process is called photoluminescence (PL). ⁴⁹ For energy conservation, some amount of energy is dissipated and the photon emitted by the radiative process has less energy than the incident photon in a conventional PL. The emitted photon is called red shifted. After photon absorption, electrons typically go through various relaxation processes, which could be non-radiative before relaxing through a radiative process. It is one of the forms of light emission. PL emission at a particular energy suggests that the excited state was populated for that specific transition energy.

PL spectroscopy can be used for various applications such as bandgap characterization, detection of impurity and defects, quality of material, and recombination

mechanism. It is a nondestructive, non-contact technique to map out electronic structure of 2D materials.

The time period between absorption and emission event can vary from material to material anywhere from few femtoseconds to milliseconds. Time resolved photoluminescence spectroscopy is a technique to measure PL lifetimes by monitoring the PL decay as a function of time after photo-excitation of the sample. This method has been widely used to measure minority carrier lifetime in semiconductors.⁵⁰

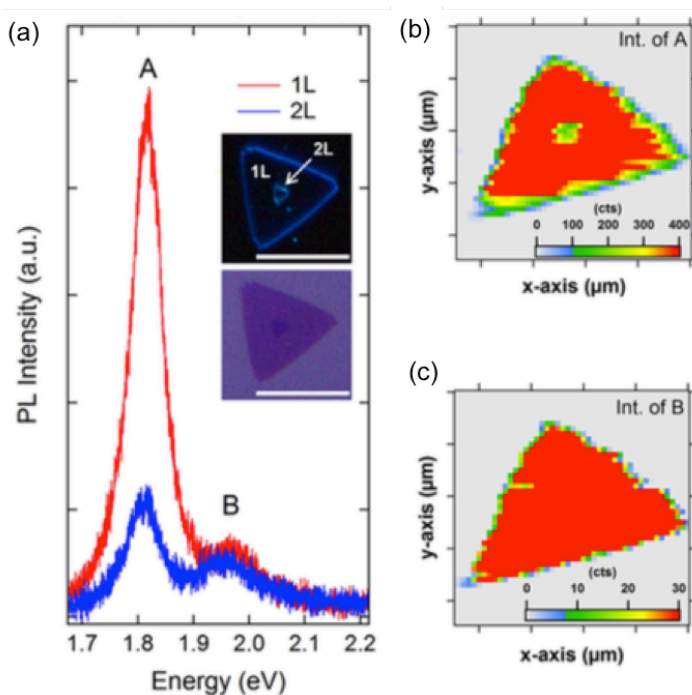


Figure 2.7: Photoluminescence map of MoS₂ single crystal. (a) PL spectra of single (red) and bilayer (blue) CVD grown MoS₂ crystal. The inset shows dark (top), and bright (bottom) field optical microscope images highlighting one and two layers. (b-c) Spatial PL intensity maps of A (b) and B (c) exciton peaks shown in (a). [Adapted from⁵¹.]

PL spectroscopy and time resolved photoluminescence spectroscopy can be combined with microscopy to map the intensity and lifetime of photoluminescence with

diffraction limited spatial resolution. PL microscopy along with PL emission and excitation spectrum has been proven useful for TMD material characterization such as electronic structure, number of layers, and defects.^{13,51-54}

TMDs have attracted attention for photovoltaic applications because recent studies showed that single layer TMD material absorbs $\sim 10\%$ of incident light on resonance as shown in Figure 1.5. Moreover, an indirect bandgap transition becomes a direct bandgap transition going from multilayer to a single layer as shown in the Figure 1.4.¹³ The photoluminescence intensity increases by two orders of magnitude for a single layer compared to bilayer MoS₂ as shown in the PL spectrum and spatial maps in Figure 2.7. This results in highly localized bound excitons with the binding energy on the order of hundreds of milli-electron volts just below the continuum bandgap energy.

This dissertation focuses on PL emission from tBLG and the mechanism behind it. PL emission mechanism from graphene and tBLG is discussed in Chapter 5. For the scope of this research, a custom built Horiba fluorimeter (see Section 2.3) was used for solution samples and homogeneous 2D material films to acquire excitation and emission spectra. For micron size 2D material PL collection, a microscopy technique either wide field geometry with a lamp excitation or confocal scanning with a laser excitation was used. For the wide field lamp excitation, hyperspectral set up discussed in Section 2.3 with either a monochromator with PMT or filter sets with EMCCD detection set up was used. For confocal scanning with the laser excitation, Ti:sapphire pulsed laser source was coupled into a microscope and scanning-galvo mirrors were used for raster scanning the laser beam over the sample. The excitation laser source was scanned to acquire PL

excitation spectrum. PL was detected with filter sets either using PMT or EMCCD camera. The details of this confocal PL setup are discussed further in Chapter 5.

2.5 Transient Absorption Microscopy and Spectroscopy

Transient absorption (TA) spectroscopy also known as pump-probe spectroscopy is a powerful technique to characterize electronic and structural properties of short-lived or transient states. An ultrafast laser pulse called the pump pulse excites a material to be studied, the material absorbs energy, and a number of excited species decay as the extra energy dissipates. Another ultrafast laser pulse called the probe pulse then arrives at the sample at a known time after the pump pulse. The probe pulse measures how the absorption of the sample was modified by the pump pulse.^{55,56} By varying the time delay between the pump and the probe pulse, the time dependent change in absorption can be measured which can provide information of carrier lifetimes. For each time delay, the transient absorption spectrum can also be recorded which provides electronic properties. Since the probe pulse arrives at the sample after some time delay with respect to the pump pulse, the population of excited states to absorb the probe pulse decreases resulting in a decrease in intensity in absorption spectrum as time goes by as shown in Figure 2.8. A motorized translation stage with a retroreflector on the stage is used to delay one pulse with respect to the other. The probe pulse should be much less intense than the pump pulse, not to influence the excited sample but only interrogate the change produced by the pump pulse in the sample.⁵⁵⁻⁵⁷

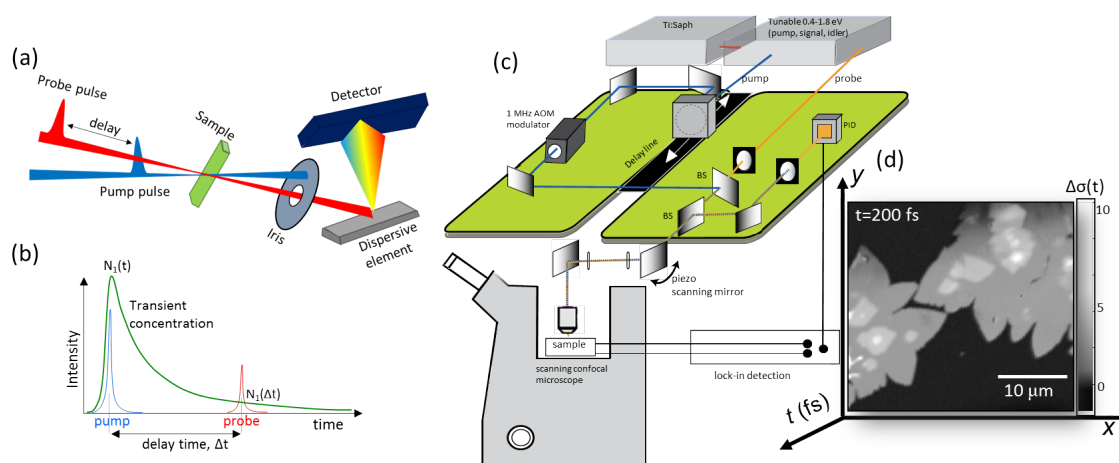


Figure 2.8: Transient Absorption spectroscopy. (a) Schematic of pump-probe experiment in transmission mode. (b) Pump beam excites the sample, probe beam arrives at the sample after some time delay and measures absorption change. (c) Optical setup for transient absorption (TA) microscopy. Sub-diffraction limited pump, and probe pulses are raster scanned, and the sample can be imaged against the laser noise floor by employing a lock-in amplifier detection synchronized to an acousto-optical (AO) modulator (1 MHz). (d) Stacked TA images for a movie of the localized electronic decay.

The schematic of a typical TA spectroscopy is shown in Figure 2.8a. Femtosecond pump pulse is produced directly from Ti:sapphire oscillator and/or amplifier system and optical parametric amplifier or harmonic generator system. UV, vis, and IR femtosecond probe pulses are generated with either an optical parametric oscillator, supercontinuum generator, or harmonic generating system. Monochromator or prism based systems are used for appropriate probe wavelength selection. The pump beam is modulated by an acousto-optic modulator. This technique can be used in transmission or reflection geometry. The transmitted or reflected probe beam is measured with an appropriate photodetector, which is connected to the lock-in amplifier. Lock-in amplifier is synchronized with the modulator to acquire measurements with pump only

and pump and probe on the sample.⁵⁵⁻⁵⁷ Spectral resolution for the measurements is obtained by placing a monochromator or spectrograph in front of the detector. The time resolution is achieved by scanning the mechanical delay stage between the pump and the probe pulse. Diffraction limited resolution is now possible combining TA with confocal scanning microscopy.

To achieve diffraction-limited spatial resolution, TA is combined with confocal scanning microscope set up as shown in the Figure 2.8b. Scanning confocal ultrafast transient absorption (TA) microscopy now enables us to simultaneously obtain near diffraction-limited spatial resolution while also having a sub-picosecond time resolution.^{58,59} This allows us to study the electron relaxation dynamics in a single-grain of graphene and other 2D materials. In Figure 2.8b-c, we show bilayer CVD graphene locally excited with a modulated (1 MHz) 140 fs pump pulse at 980 nm. We then probe graphene at 1650 nm using a second collinear probe pulse at some time-delay, t . By collecting the change in reflectance ($\Delta R(t)$) of the probe pulse, we plot the dynamics of graphene in both space and time. By stacking the frames in Figure 2.8b, we can reconstruct a ‘movie’ of photoexcited hot electrons relaxing. This electron-relaxation ‘movie’ is also a novel fast imaging technique for nanomaterials, and requires only seconds to acquire each frame.

In TA spectroscopy, the measured response of the sample is generally expressed as the absorption change given by, $\Delta A = A_{\text{exc}} - A_{\text{noexc}} = \text{Log}\left(\frac{I_{\text{noexc}}}{I_{\text{exc}}}\right)$; where, A_{exc} , A_{noexc} is the absorption of the excited and non-excited sample respectively. I_{exc} , I_{noexc} is the probe intensity of excited and non-excited sample respectively.^{60,61} The response is measured as a function of delay time and the probe wavelength; $\Delta A = \Delta A(t, \lambda)$.

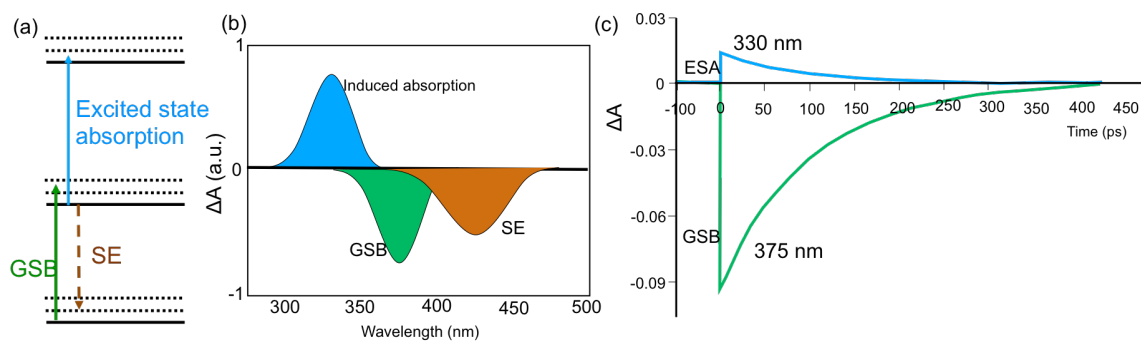


Figure 2.9: Energy level diagram, TA spectroscopy, and time dynamics. (a) Energy level diagram of a typical hypothetical molecule showing different quantum transitions. (b) Difference absorption spectrum showing excited state absorption, ground state bleach and stimulated emission response for the transitions shown in (a). (c) Time dynamics of a molecule showing positive response at 330 nm and negative response at 375 nm probe corresponding to excited state absorption and ground state bleach respectively labeled in (a), (b).

TA spectroscopy includes two main contributions relevant to this research work: ground state bleach (GSB) also known as Pauli blocking response, and induced absorption also known as excited state absorption (ESA). The charge carriers transition from the ground state to the excited state when a sample is excited with an ultrafast pump pulse. As shown in Figure 2.9, the excitation results in populating the excited state that leaves little to no charge carriers in the ground state. This depletes the ground state carriers called bleaching, giving negative ΔA as shown in the Figure 2.9b-c. This response is known as GSB. On the other hand, when the charge carrier is in the excited state can go to higher excited state by absorbing the incoming photon, ΔA becomes positive as shown in the Figure 2.9b-c. This response is known as ESA.^{55–57,60,61}

Typical time dynamics of a hypothetical molecule for a given energy are shown in Figure 2.9. Once, the material is excited; various processes can occur during relaxation.

For a typical solid state system, the system relaxes to vibrational sublevels also known as phonon modes within few fs timescale. Then, carriers thermalize among themselves within tenths of fs, charge carriers then thermalize with the lattice with few ps time scale. Typical 2D semiconductor yields long lifetimes on the order of ns time scale for resonant pump-probe excitation.

2.6 Raman Spectroscopy and Wide-Field Raman Imaging

Raman spectroscopy is a class of vibrational spectroscopy like IR spectroscopy. It provides information about molecular vibrations for identification and quantification. It involves laser light interaction with the molecular vibrations, phonons or other excitations, which shift the laser light energy up or down. The energy change of the inelastic light is mostly quantified in wavenumber, which corresponds to energy. The vibrational modes in the system can be understood from this energy shift.^{62,63}

In its simplest form, a laser beam illuminates the sample, and the scattered light is sent to a monochromator. The majority of the scattered light is elastically scattered which is known as Rayleigh scattering, which has the same frequency as the excitation laser frequency. We detect the inelastically scattered light whose energy is shifted from the incident excitation energy owing to interactions with the Raman-active vibrational modes. Elastically scattered light gets filtered out with optical filters, and the rest goes to the detector.⁶³ The intensity of the shifted light as a function of frequency gives a Raman spectrum for a particular system.

Raman scattering is typically weak, and it is difficult to separate out inelastic scattering from the elastic or Rayleigh scattered light. For carbon nanotubes, only 1 out of

10^{10} absorbed photons goes through the Raman scattering process.⁶⁴ To successfully detect Raman scattering, a monochromatic focused laser source with high intensity is typically used.⁶⁵ Micro-Raman measurements are performed to examine the region of interest on samples. Raman spectra are generally substrate dependent. As a result, appropriate care needs be taken while interpreting the measurements correctly.⁶⁶

Raman spectroscopy has demonstrated to be an advantageous technique to characterize 2D materials, specially sp^2 -bonded carbon materials since it involves interaction between electronic and vibrational excitation. As a consequence, Raman spectroscopy provides information such as disorder, doping, defects, stacking order, number of layers, and strain.⁶⁷⁻⁷⁰

Typical Raman spectrum of graphene is shown in the Figure 2.10. Raman G peak located at $\sim 1580 \text{ cm}^{-1}$ and 2D peak located at $\sim 2700 \text{ cm}^{-1}$ are the most prominent peaks. Other peaks such as D and D' represents defects in graphene which are not present in pristine graphene. These defects could be point defects, cracks, and wrinkles, or grain boundaries.^{23,71-74} When graphene layers are oriented in a minimum energy configuration like in exfoliated graphene case, Raman 2D and G peaks are reliable indicators of the number of layers.^{70,75-77} However, when two or more layers of graphene are not stacked in a minimum energy configuration, a rather complicated behavior of Raman 2D and G peaks is expected which varies as a function of the angle between the layers and excitation

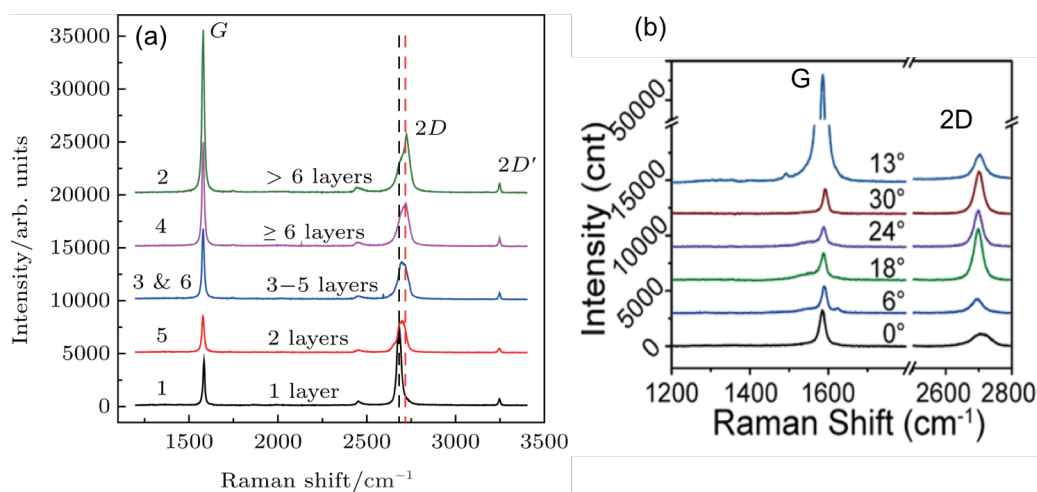


Figure 2.10: Raman spectroscopy of graphene and tBLG. (a) Typical Raman signatures of graphene with different samples with varying thickness shows prominent response labeled as G and 2D peaks, all the other peaks correspond to defects. For a single layer graphene, a sharp 2D peak is much larger in intensity than multilayer graphene. G peaks grow as a function of a number of graphene layers.⁷⁸ (b) Raman spectrum of tBLG for different twist angle. The 2D peak is evolving with an angle.⁷⁹ [Adapted from ^{78,79}.]

energy of the light source.^{46,80,81} Unlike graphene, Raman spectroscopy of 2D materials such as the family of TMDs and h-BN has not been thoroughly characterized. Absorption and photoluminescence spectroscopy has been widely used to characterize TMDs instead.

Typical Raman spectrum is measured at a single point to examine a small area of interest with a technique called micro-Raman spectroscopy as shown in Figure 2.11.^{82,83} To acquire two-dimensional spatial mapping, the focused laser spot is raster scanned across the sample. However, since Raman scattering is very weak and allowed laser intensity on the sample is small due to low sample damage threshold, this technique has low throughput. As a consequence, generating tens of micron images takes hours. Due to this limitation, it is not an efficient method for large scale, rapid imaging.⁸⁴

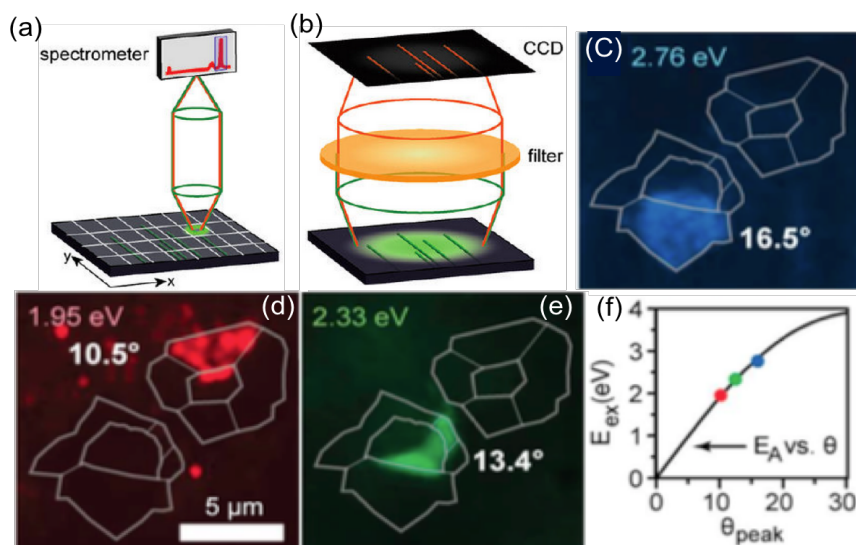


Figure 2.11: Micro Raman, widefield Raman microscopy, and Raman G-band enhancement in tBLG. (a) Schematic of micro-Raman imaging. It collects spectrum point by point with series of pixels. (b) Schematic of wide-field Raman imaging. It allows large area imaging of a specific Raman mode. (c-e) Widefield Raman G band images of tBLG domains with different angles excited with three different energies, 2.76 eV, 2.33 eV and 1.95 eV. Different pieces show preferential enhancement for a given excitation energy. (f) Excitation energy as a function of the angle between the two layers showing monotonic behavior. [Adapted from⁴⁶.]

An alternative approach is wide-field Raman imaging shown in Figure 2.11 which can be used for large scale, rapid imaging.⁸⁵⁻⁹⁰ This technique has been extensively employed in various fields of science such as materials, chemistry, and biology.^{46,68,77,80} This method starts with a sample illuminated by a large defocused laser spot, and then the Raman scattered light is sent through optical filters, and a charged cooled camera for the desired Raman band. This technique has primarily two advantages; i. laser power for illumination can be orders of magnitude more than micro-Raman imaging since the power is getting distributed to a large surface area giving a better signal to noise, ii.

illumination of larger area enable image acquisition of few hundreds of micron across in a few minutes. Diffraction limited large-area scans for different Raman bands can be achieved rather quickly for band ratio calculations.

Widefield Raman imaging has been used to characterize twist angles, θ in tBLG configuration. In tBLG configuration, two layers of graphene are stacked at an off axis angle, which creates angle tunable absorption resonances best interpreted as van Hove singularities (vHs) near avoided crossing regions (details are discussed in Chapter 3, 4). This vHs gives rise to angle tunable Raman G band enhancement and Raman 2D band modification.^{46,81} As shown in Figure 2.11, upon scanning with the different excitation laser energies on a bilayer graphene sample, the different pieces began to show Raman G band enhancement in the sample corresponding to the distinctive orientation of two graphene layers. Raman G band enhancement increases monotonically as a function of energy similar to absorption resonances discussed in Section 2.3. This technique is a powerful tool for spatial and spectral characterization of 2D materials. In particular, it is useful in examining defects, number of layers, and relative layer orientation.

2.7 Electron Microscopy

Electron microscopes (EM) can be used to image crystalline structures and the morphology of 2D materials over a large area up to few millimeters with atomic resolution. All electron microscopes control the path of electrons with electromagnetic lenses. Electromagnetic lenses primarily consist of a solenoid where the electromagnetic field is induced by passing current through it. The current through the lenses controls the

electron beam. The electron beam reaches the sample and travels through the center of a solenoid down the column of the microscope.⁴⁶

The resolution of an electron microscope is determined by the wavelength of irradiation used to form the image. Electrons that travel faster have shorter wavelengths which increase the spatial resolution. Therefore, increasing the accelerating voltage increases the spatial resolution of electron microscopes. Current spatial resolution of electron microscopes is limited to about 100 pm due to limitations of electron optics that control the accelerating voltage.⁴⁶ Although electron microscopes are widely used, they require a continuously pumped ultra-high vacuum system and cooling water supply circulation through lenses and pumps which limits imaging use in material characterization. Moreover, a special sample preparation is required for EM techniques. Suspended or thin membrane substrates are the only choices because the sample of interest must be transparent to electrons for imaging. The sample also needs to be clean for imaging, EM techniques are also destructive to the lattice and could deposit amorphous carbon on the surface.⁹¹

2.7.1 Transmission Electron Microscopy

Transmission electron microscopy (TEM) is a widely used characterization technique for 2D materials. The electron beam illuminates several micron areas of the sample and the transmitted electron beam through the sample is examined that forms an image in this imaging mode. An image is formed due to the interaction of the electron with the sample when the beam is transmitted through the sample. This technique is useful to obtain morphology, number of layers, quality of the sample, and tears down to atomic spatial resolution. Crystallinity and orientation of the sample can be achieved by

acquiring electron diffraction pattern and looking at the relative Bragg peaks intensity with this imaging technique.^{92,93}

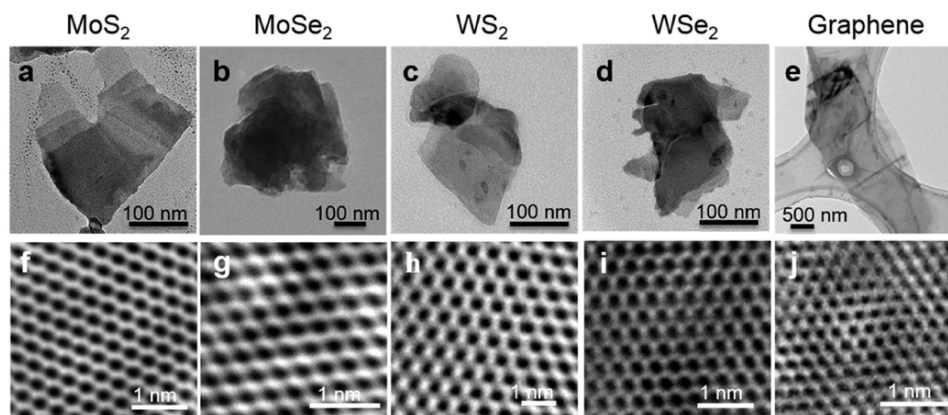


Figure 2.12: TEM images of vdW 2D materials MoS₂, MoSe₂, WS₂, WSe₂, and graphene produced with liquid exfoliation method. Top: low-resolution TEM images, bottom: high-resolution TEM images showing hexagonally symmetric structure. [Adapted from⁹⁴ .]

A single crystal of most 2D materials produces diffraction pattern with six-fold symmetry.^{23,71,72} This technique requires special sample holders, so samples need to be transferred on the TEM grids. Special TEM grids can be purchased for specific imaging conditions such as heating and cooling. TEM facilities for low resolution down to a few nm are readily available at research facilities. However, high-resolution down to angstroms TEM facilities called aberration corrected TEM are rare and difficult to get access to. Aberration corrected high-resolution TEM provides atomic scale images of 2D materials which also contains information on elemental identification of atoms.^{70,75,95} This imaging mode has been used for imaging 2D materials such as graphene, h-BN, and MoS₂ successfully.^{66,95-97} As shown in Figure 2.12, individual atoms are classified as MoS₂ and other 2D materials. Apart from rare access to high-resolution TEM facilities,

and special sample preparation procedures, this imaging mode is slow in acquiring images a few micron across making it limited to smaller scan areas.

2.7.2 Dark-Field TEM

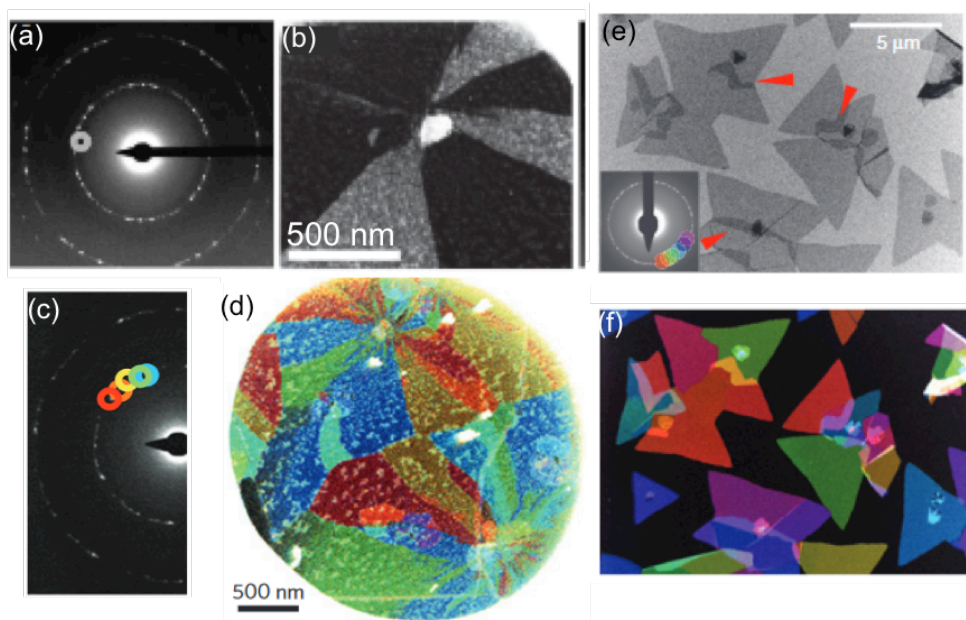


Figure 2.13: Dark field TEM imaging of 2D materials. Diffraction spots, and grain orientation. (a) An electron diffraction pattern from a suspended graphene sample with six fold symmetry. (b) For the selected aperture location in (a) circle, dark field TEM imaging shows different crystal orientation. (c-d) False color imaging of graphene with dark-field TEM showing false colored areas with various crystal orientation.²⁴ (e) White-field imaging of MoS₂ showing grain boundaries and formation of bilayer (red arrows). (f) Colored dark field TEM of (e) showing crystal orientation.⁹⁷ [Adapted from ^{24,97}.]

In the dark-field TEM mode, information about planar defects, stacking orders, particle size grain orientations of 2D materials can be visualized as shown in Figure 2.13.^{66,68,71,98,99} Once the diffraction pattern of the sample is obtained, a small aperture is placed in the diffraction plane to collect only electrons that have scattered in the selected

directions. This images sample domains that are only diffracting in this range of angles. By moving the aperture to select various diffraction spots, series of images can be acquired to map out all possible grain orientations in the sample. The final images can be superimposed to generate spatial maps of the domain structure and orientation of the sample. For example, in Figure 2.13a-c there are three sets of diffraction spots suggesting different stacking orientations in a multilayer graphene sample. DF-TEM has been widely used to determine the local atomic structure to determine the stacking angle between two layers of graphene for tBLG configuration in this dissertation.

2.7.3 Scanning Electron Microscopy

Scanning electron microscopy (SEM) produces images of a sample by raster scanning the sample surface with a focused electron beam. The electron beam interacts with atoms at various depths in the sample which produces signals that contain information about the sample's composition and surface morphology.

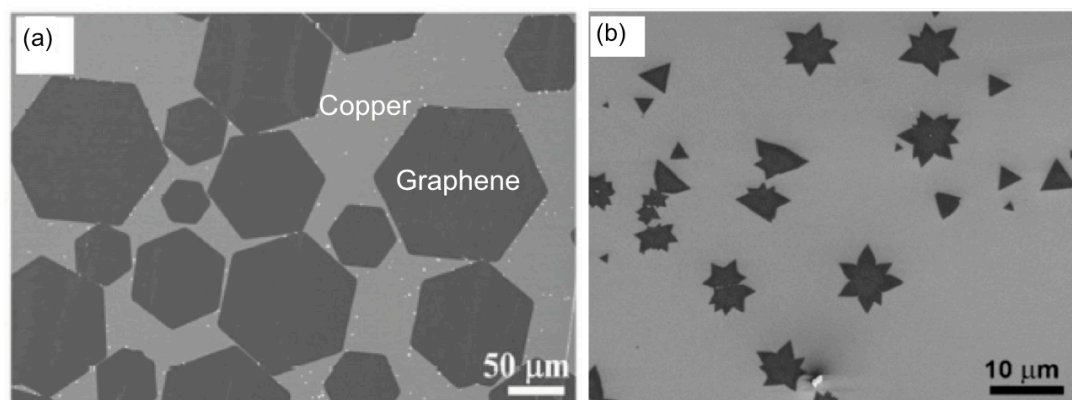


Figure 2.14: SEM imaging of CVD grown graphene and MoS₂. (a) Large graphene single crystal of average size 120 μm grown with CVD process on flat liquid Cu Surface.¹⁰⁰ (b) MoS₂ monolayers of different shapes grown with CVD method.¹⁰¹ [Adapted from^{100, 101}.]

The produced signals are secondary electrons (SE), back-scattered electrons (BSE), characteristic X-rays, light cathodoluminescence (CL), absorbed current, and transmitted electrons. Every SEM has secondary electron detectors, but not every SEM has all the other detectors for other signal detection.¹⁰² Due to the large depth of field, the spatial resolution of SEM is about tens of nanometers smaller than TEM. However, unlike TEM, large areas up to centimeters can be imaged quickly with SEM. Samples need to be metallic or transferred on a metallic substrate for SEM imaging to avoid charge accumulation. 2D materials prepared by CVD are primarily grown on a metallic substrate, so SEM has been proven rather useful in a direct imaging of materials for a quick characterization. Such characterization of CVD grown graphene on a copper substrate is shown in Figure 2.14 where single, and multi-layer graphene, morphology, and defects in the copper substrate are visible.^{103,104}

2.8 Scanning Probe Microscopy

Scanning probe microscopes (SPMs) are imaging tools for surface structure imaging including atoms of nanomaterials. SPMs do not see the sample surface directly like optical microscopes, but instead, they feel the surface with a physical probe to generate an image that represents the sample surface.¹⁰⁵

Figure 2.15 shows a basic schematic of a scanning probe microscope. It consists of a tip with radius tenths of nanometers that is mounted on the end of a cantilever. This tip is raster scanned precisely back and forth across the sample surface. When the tip approaches the sample surface, the cantilever experiences a force as shown in the Figure 2.15 by Hooke's law as, $F = -kz$, where F represents the force, k represents the stiffness

of the cantilever, and z is the distance the cantilever is bent. As a result, the cantilever is deflected. SPMs can measure the deflections due to various forces such as van der Waals forces, electrostatic forces, mechanical contacts, magnetic forces, capillary forces, chemical bonding. SPMs require a feedback loop to control the distance between the tip and sample which can be achieved with the laser deflection, and detection mechanics. An array of photodiodes is used for detection, and the laser that is reflected off the top of the cantilever into the photodiode is used to track the distance of the deflection. Due to the feedback loop, the raster scanning rate and the scan area is limited making it a slower technique.^{105,106}

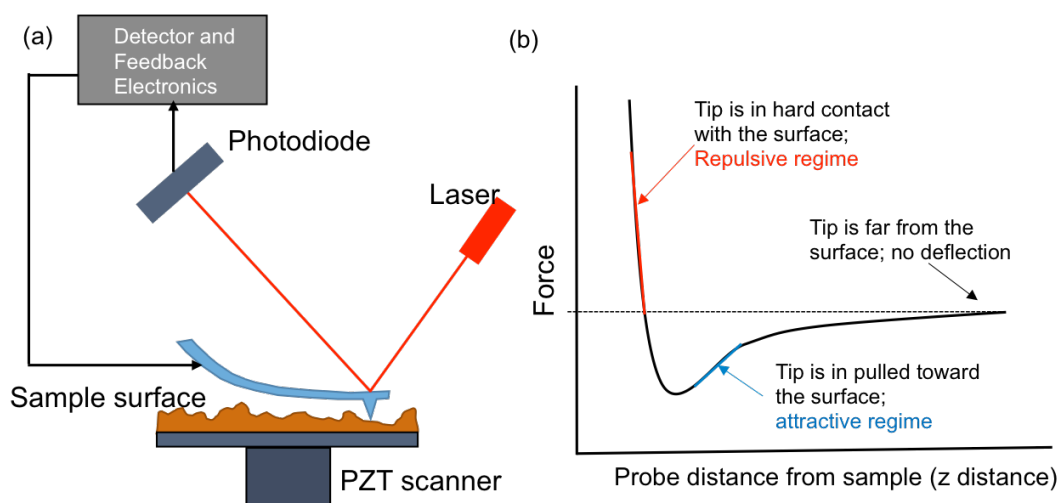


Figure 2.15: Schematic of scanning probe microscope. (a) SPM schematic. PZT scanner raster scans the sample; the cantilever deflects due to the force and the feedback loop consists of laser and photodiode that keeps control of force and tip position. (b) Force-distance curve of AFM.

There are various types of SPMs such as AFM, MFM, and STM. AFM measures electrostatic forces between the cantilever tip and the sample which provides atomic height profile in the z -direction as well as mechanical and electrical properties. MFM

measures magnetic forces. STMs measure the electrical current flowing between the cantilever tip and the sample that provides atomic surface structure and electronic properties. AFM does not require special sample preparation, any substrate is appropriate, and it can be performed under ambient conditions. On the other hand, STM requires sample preparation for cleanliness, and it is slower than AFM.

2.8.1 Atomic Force Microscopy

AFM contains a cantilever with a sharp probe at its end with a radius of about tenths of nanometers that scans the surface of the sample. Upon bringing the tip closer to the sample surface, according to Hooke's law, the forces between the tip and sample deflects the cantilever. Various forces such as van der Waals forces, capillary forces, chemical bonding, electrostatic forces, magnetic forces and so forth can be measured with AFM depending on the requirements.^{106,107} AFM is primarily used for three primary applications: (i) imaging, (ii) manipulation of atoms, and (iii) measuring forces.

Depending on the application, AFM can be operated in a number of modes for imaging. Primarily, there are two modes: (i) contact mode or a static mode where the cantilever is not oscillating, and the force between the sample and the tip is kept constant enabling quick surface imaging, and (ii) non-contact or tapping mode where the cantilever oscillates at a specific frequency.¹⁰⁸

For imaging 2D materials, tapping mode AFM is primarily used. Under tapping mode, the cantilever that oscillates at its resonant frequency is in a direct gentle contact with the surface of the sample. The cantilever raster scans the sample with a

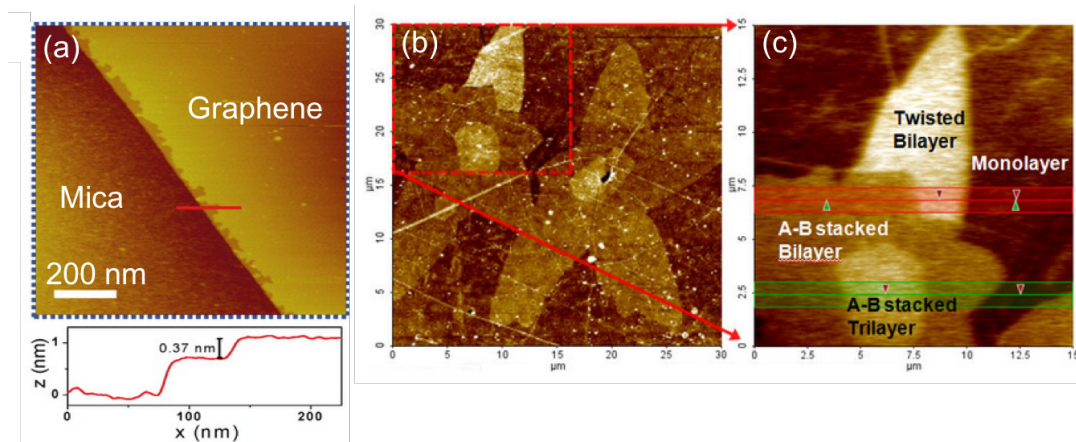


Figure 2.16: AFM imaging of multilayer and single layer graphene. (a) Graphene on the mica substrate. The height profile (bottom) for the highlighted region (red) in (a) shows 0.37 nm step going from the mica to graphene.¹⁰⁹ (b) Multilayer graphene. (c) Upon zooming in, monolayer, AB stacked bilayer & trilayer, and tBLG is visible with scanning Kelvin probe microscopy AFM.¹¹⁰ [Adapted from^{109, 110}.]

constant amplitude of the oscillation. The constant oscillation amplitude is achieved with a feedback loop with the laser deflection from the back of the cantilever of the tip to control the force and tip position. The laser position on the photodetector is used in the feedback loop tracing the surface for imaging when the tip interacts with the sample surface.¹⁰⁸ When the surface morphology or physical property changes, the tip moves up or down in the z direction which corresponds to the height of the sample surface on the sub-nm scale. Different AFM modes can be used to map out structural, electronic, and mechanical properties of 2D materials.¹¹¹ One of the examples is shown in Figure 2.16, where AFM is used to determine the number of layers by essentially mapping out the height profile of graphene.¹¹² It has been reported that AFM is not a reliable technique to determine the thickness of some 2D materials due to substrate artifacts.^{67,113} However, it

is a useful technique for surface roughness characterization and quantification of contaminants on the surface due to the sample transfer procedure.¹¹⁴

Unlike TEM and SEM, AFM does not require a special sample preparation or substrate preference, so it has been extensively used as an imaging tool in the field of material science, chemistry, biology and many more.

Conductive AFM also known as C-AFM measures the tunneling current flowing between the tip and the sample when a bias voltage is applied between the two.^{115,116} C-AFM has been widely used to map out electrical conductivity in semiconductors, carbon nanotubes, some organic materials, polymers, thin films, 2D materials for electrical defects and homogeneity characterization of material.¹¹⁷⁻¹²⁰ It works on a similar principle as STM. C-AFM uses conducting tips with a radius of a tenth of nanometers, whereas STM uses the atomically sharp metallic tip. STM uses tunneling current as a feedback signal because it does not detect forces. On the other hand, C-AFM uses cantilever deflection as a feedback signal, and it measures the tunneling current signal independent of the feedback loop.^{121,122} As a result, upon raster scanning the sample with the cantilever in contact, C-AFM produces a topography map and measures the electric current between the tip and the sample simultaneously as shown in Figure 2.17b. The schematic of C-AFM configuration is shown in Figure 2.17a when bias is applied between the sample and the tip for electrical conductivity measurement, and AFM feedback loop is established. The electrical conductivity is typically measured with an electric current amplifier with the sensitivity up to femtoampere to suppress the electric noise and detect typical picoampere electric current produced between the tip and the sample.

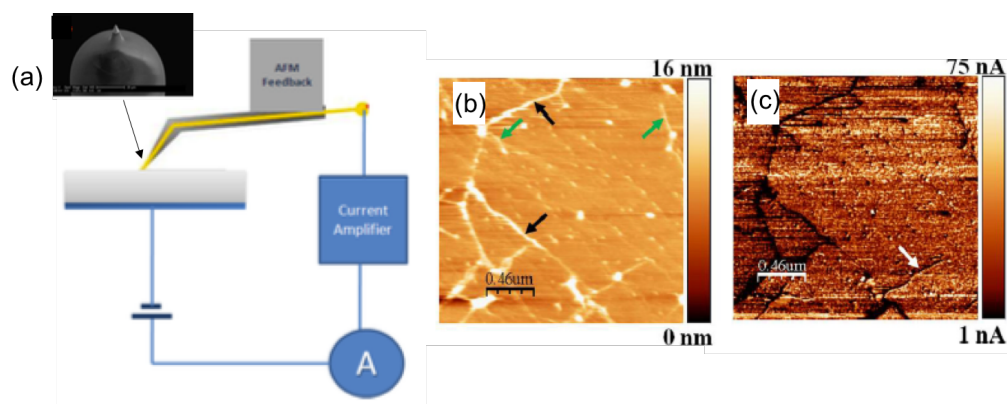


Figure 2.17: Electrical measurement schematic of C-AFM, zooming in at the tip at the end of the cantilever, topography image of 2d material left, and conductivity map on the right. [Adapted from¹²³.]

In the scope of this study, we are developing a technique that uses a MutiView2000 AFM system from Nanonics Inc. with tuning fork feedback mechanism. Double pipette tip with the distance between the two wires 3-10 μm was threaded with a platinum nanowire and mounted on the tuning fork as shown in the Figure 2.17. For electrical conductivity detection, a FEMTO current preamplifier with amplification range 10^3 - 10^{11} is used. The DC bias between the tip and the sample is applied using FEMTO current preamplifier using controller interface box with built in software or external voltage source.

To study photocurrent production down to ~ 10 nm spatial resolution in 2D materials, a vis-IR near-field microscopy system has been developed.¹²⁴ This uses a MutiView2000 AFM system from Nanonics Inc. combined with a femtosecond pulsed laser source discussed in detail in Chapter 6. This photoconductive approach allows direct visualization of nm resolved photocurrent production in 2D materials in situ. This method represents a needed diagnostic tool to quantify material's intrinsic photocurrent

internal quantum efficiency before great effort is invested in development. The knowledge achieved from this study could directly impact material considerations for next generation high-efficiency solar voltaic.

2.8.2 Scanning Tunneling Microscopy

Scanning tunneling microscope (STM) operates on the principle of quantum tunneling. The atomically sharp metallic tip is brought very close to the sample surface, and between the sample and the tip, a voltage difference is applied.^{125,126} This permits electrons to tunnel through the vacuum between the tip and the sample. This results in a tunneling current, which is a function of the tip position, applied voltage, and the local density of states of the sample that is being studied.¹²⁷ The tunneling current is monitored as the tip raster scans the sample back and forth. Since the tunneling current is exponentially sensitive to the distance between the sample and the tip, it can be used as a feedback mechanism to map out atomic scale surface topography, which also represents the local free electron density.

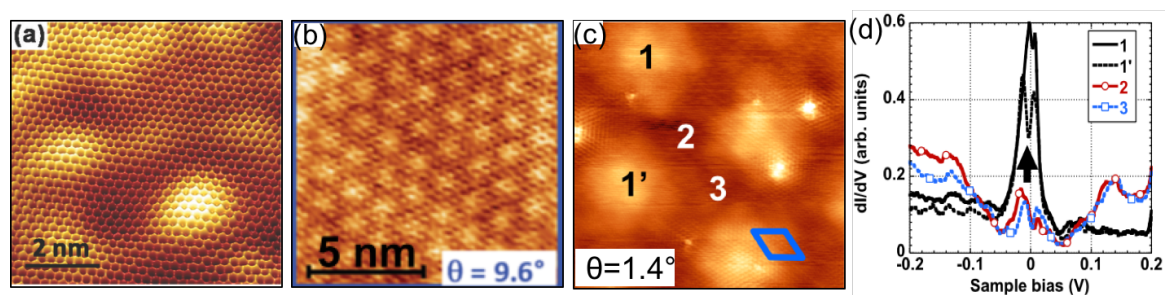


Figure 2.18: STM imaging of graphene, and tBLG showing atoms and local density of states. (a) Graphene showing atomic ripples and hexagonal structure,¹²⁸ (b) tBLG domain of 9.6° . Moire pattern is visible. (c) Moire pattern in 1.4° tBLG domain. (d) STS spectra showing vHs (arrows pointing at the peaks) in the density of states¹²⁹ [Adapted from^{128, 129}.]

STM can be operated in a scanning tunneling spectroscopy (STS) mode to acquire local density of states as a function of energy. In this mode, upon sweeping the voltage while measuring the tunneling current at a particular location produces the electronic structure information for a given location.¹³⁰ STM and STS have been widely used to study electronic properties of defects, the interstitial density of states and atomic structure of individual material or heterostructure of 2D materials.⁴²⁻⁴⁴ STM has also been used to measure interlayer interactions for bilayer graphene showing vHs in a small angle tBLG configuration sample.¹²⁵ As shown in Figure 2.18, atomic scale image of defects in CVD graphene and local density of states can be established with this technique. STM is an advantageous technique in mapping out the local density of states (LDOS). However, it measures combined LDOS of the sample and substrate making it challenging to deconvolute the sample response for obtaining the electronic structure of the sample. This technique requires special sample preparation for cleanliness, and due to the feedback loop mechanism, it is limited to small scan area.

2.9 Characterization of Twisted Bilayer Graphene

To characterize tBLG, we have employed a combination of multiple imaging techniques described earlier in this Chapter, such as optical microscopy, hyperspectral imaging, TA microscopy, and dark-field TEM. Multi-layer graphene was grown using a low-pressure CVD method on copper foil and then transferred to silicon nitride grids, silicon, or fused silica as discussed in Chapter 1. Areas containing low-angle tBLG were first identified using a combination of hyperspectral absorption imaging techniques, and

dark-field TEM. Final twist angle assignments of the bilayer patches were made by correlating the linear absorption and 1-ph TA peak spectral peaks energies.

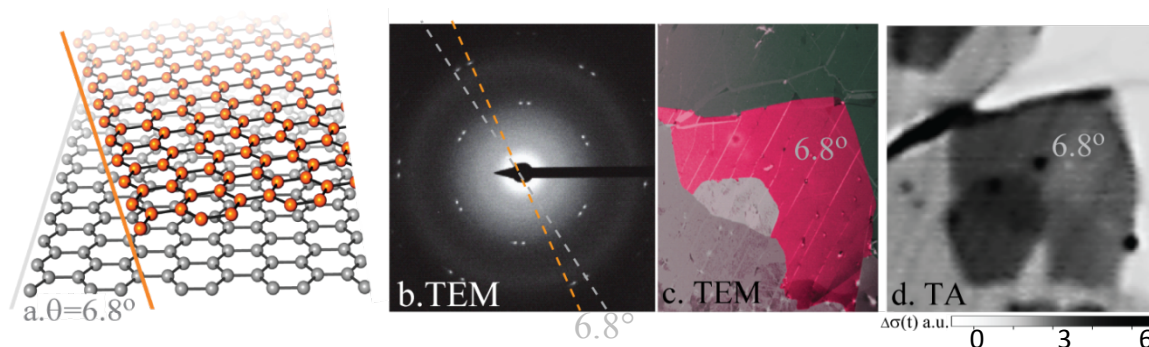


Figure 2.19: Areas containing low-angle tBLG were first identified using TA microscopy, they were then verified using hyperspectral linear absorption spectroscopy technique, and dark field TEM (DF-TEM).

Transient absorption (TA) microscopy on tBLG requires (i) identification of large-area tBLG regions, (ii) diffraction limited probe-beam resolution TA. First identification of tBLG domains was done using diffraction-limited scanning confocal TA microscopy. tBLG regions were detected by exciting above resonance and probing well-below resonance (typically at 0.8 eV), as shown in Figure 2.19. tBLG regions show a markedly enhanced TA when the resonance lies between the pump and probe beam energies, owing to the strong electronic relaxation bottleneck effect in the interlayer tBLG states. Once the regions with anomalous electronic dynamics are identified, the precise absorption resonances are measured using hyperspectral absorption imaging.³⁸ By collecting the full-frame absorption movies, specific absorption spectra can be acquired by integrating over a defined region and plotting as a function of absorbing wavelength.

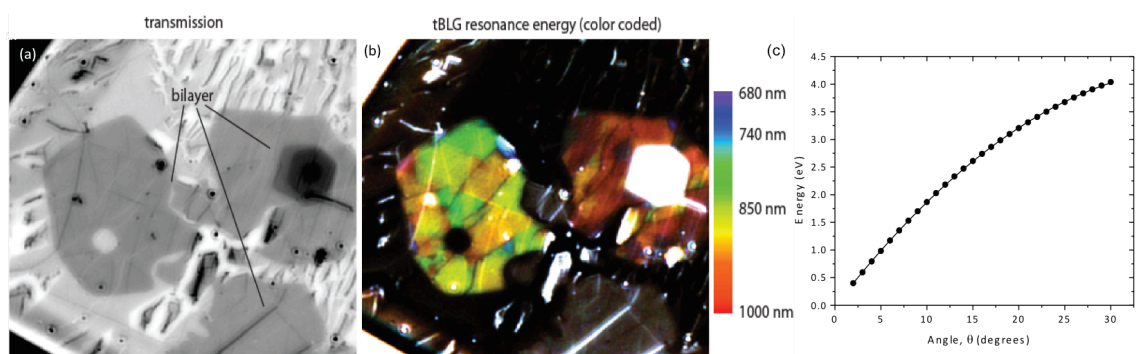


Figure 2.20: Hyperspectral microscopy characterization.³⁸ (a) Off-resonant linear absorption maps reveal large areas of bilayer absorption. (b) Hyperspectral absorption map shows two dominant absorption resonances corresponding to tBLG regions that are $\sim 6.5^\circ$ and $\sim 8^\circ$ oriented. (c) The plot of how the twist angle absorption scales with stacking angle as determined by darkfield TEM.

The correspondence between absorption resonance and twist angle has been previously established.^{38,46} Once all optical measurements were complete, dark-field TEM was used to determine precise angle assignments (see Figure 2.19), and a composite image is constructed such as the one shown in Figure 2.20. Similar results were obtained for tBLG on silicon, silicon nitride, and fused silica substrates.

2.10 Summary

In this Chapter, we discussed several imaging methods for small and large scale imaging of 2D materials. Each technique provides a different type of information about the material. As a result, a combination of these techniques is usually necessary to acquire a full-picture of a material's properties. Over the past decade, all of these characterization techniques have been successfully applied to most of the 2D class of materials. In particular, we discussed the techniques developed by our group or our collaborators, which is used heavily throughout this dissertation such as TA microscopy,

photoluminescence microscopy, optical microscopy and hyperspectral imaging. For the scope of this dissertation, we employed a combination of optical microscopy, hyperspectral imaging, TA and dark-field TEM techniques to characterize tBLG material as discussed in Section 2.9.

3. THEORY: INTERLAYER ELECTRONIC STRUCTURE

Ultrafast microscopy captures the dynamics of bound excitons in twisted bilayer van der Waals materials

Hiral Patel, Kyle Vogt, Lujie Huang, Jiwoong Park, and Matt W. Graham

SPIE (keynote invited paper), 10 pages, doi:10.1117/12.2262003, 2017

Stacking and twisting 2D van der Waals (vdW) materials can create unique electronic properties that are not accessible in a single sheet of material. For instance in tBLG, we can access both massless and massive chiral quasiparticles characteristics of graphene and bilayer graphene as well as angle tunable optical resonances that are not present in graphene or bilayer graphene. In addition, first principle simulations predict that upon optical resonant excitation of tBLG, bound exciton formation is probable due to cancelation of exciton-continuum coupling from anti-symmetric superposition of degenerate resonant transitions. Here, we discuss the theory aspect of the interlayer electronic structure and explain how bound-exciton formation is a possibility in tBLG.

This chapter is largely adapted from H. Patel *et al.*, “Ultrafast microscopy captures the dynamics of bound excitons in twisted bilayer van der waals materials”, 10 pages, keynote invited paper, SPIE, doi:10.1117/12.2262003. Here, we describe the theory of interlayer electronic structure and excitonic effects in graphene and twisted bilayer graphene.

3.1 Electronic Band Structure of Graphene in the Tight Binding Approximation

We begin with a brief review of the electronic structure of graphene to establish a common notation for discussing the interlayer electronic structure of twisted bilayer graphene (tBLG) in the later sections. The atomic structure of single layer graphene in Figure 3.1a shows distinct carbon atoms, A and B, in the unit cell. The lattice vectors are: $\mathbf{a}_1 = \sqrt{3}a_0 \left(\frac{1}{2}, \frac{\sqrt{3}}{2}\right)$, $\mathbf{a}_2 = \sqrt{3}a_0 \left(-\frac{1}{2}, \frac{\sqrt{3}}{2}\right)$ where a_0 is the nearest neighbor distance, $a_0 = 1.42 \text{ \AA}$.¹³² Out of the four valence electrons, three are used for sp^2 bonds in carbon. The fourth electron is in a p_z orbital, and there are two electrons per unit cell in a p_z orbital. Therefore, there are two orbitals, one for atom A, and one for atom B for a unit cell (there are two π - bands, one for each electron). The tight-binding model Hamiltonian: $\hat{H} = \sum_{\langle r, r' \rangle} (-t a_1^\dagger(\mathbf{r}) a_2(\mathbf{r}')) + \text{Hermitian Conjugate (HC)}$ ¹³³ can be expanded over the graphene unit cell site basis to obtain,

$$\hat{H} = \sum_{\langle r, r' \rangle} \left(-\frac{t}{N}\right) \sum_{\mathbf{k}, \mathbf{k}'}^{\text{BZ}} e^{-i\mathbf{k}\cdot\mathbf{r}} (e^{i\mathbf{k}'\cdot\mathbf{r}'} + e^{i\mathbf{k}\cdot\mathbf{r}} e^{i\mathbf{k}\cdot\mathbf{a}_1} + e^{i\mathbf{k}\cdot\mathbf{r}} e^{i\mathbf{k}\cdot\mathbf{a}_2}) a_{1\mathbf{k}}^\dagger a_{2\mathbf{k}'} + \text{HC}$$

here t represents the transfer integral corresponding to electronic hopping between atoms and the Fourier-transformed creation and annihilation operators are defined as,

$$a_1^\dagger(\mathbf{r}) = \frac{1}{\sqrt{N}} \sum_{\mathbf{k}} e^{-i\mathbf{k}\cdot\mathbf{r}} a_{1\mathbf{k}}^\dagger, \quad a_2(\mathbf{r}') = \frac{1}{\sqrt{N}} \sum_{\mathbf{k}'} e^{-i\mathbf{k}'\cdot\mathbf{r}'} a_{2\mathbf{k}'},$$

Alternatively, this can be expressed in a matrix form, with an overall phase factor of $e^{-i\mathbf{k}'\cdot(\mathbf{r}-\mathbf{r}')}$, as

$$\hat{H} = \sum_{\mathbf{k}} (a_{1\mathbf{k}}^\dagger \ a_{2\mathbf{k}}^\dagger) \begin{pmatrix} 0 & -t f(\mathbf{k}) \\ -t f^*(\mathbf{k}) & 0 \end{pmatrix} \begin{pmatrix} a_{1\mathbf{k}} \\ a_{2\mathbf{k}} \end{pmatrix}, \quad \text{where } f(\mathbf{k}) = (1 + e^{i\mathbf{k}\cdot\mathbf{a}_1} + e^{i\mathbf{k}\cdot\mathbf{a}_2}) \dots 3.1$$

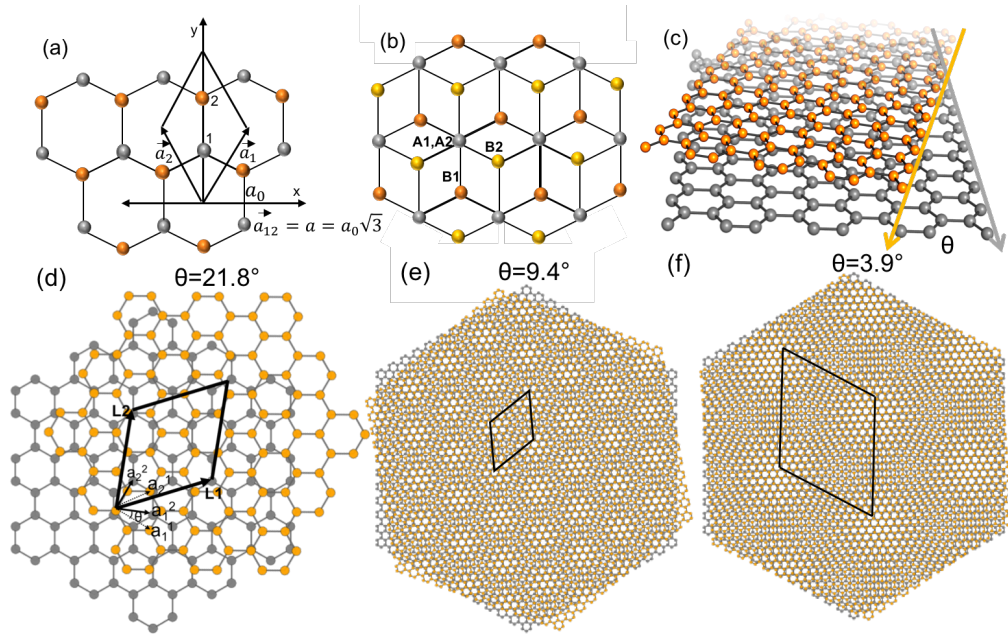


Figure 3.1: (a) Lattice structure of single layer graphene; Two carbon atoms per unit cell are labeled as 1, and 2 (gray, and orange). Primitive vectors are \vec{a}_1 , and \vec{a}_2 . (b) Lattice structure of bilayer graphene. Sub lattices for the lower layer are A1, and B1, and those for the top layer are A2, and B2, with relative positions of atoms projected onto the x-y plane. (c) Lattice structure of twisted bilayer graphene for rotation θ , (d) tBLG $\theta=21.8^\circ$, with $[(m,n)=(1,2)]$, highlighted unit cell for (e) $\theta=9.4^\circ$, (f) $\theta=3.9^\circ$.

The diagonal term H_{AA} corresponds to the orbital interactions between two A atoms, H_{BB} corresponds to the orbital interactions between two B atoms. H_{AB} , and H_{BA} represent hopping between the two sites A, and B. To find the dispersion relation, setting onsite energies, $\varepsilon_A = \varepsilon_B = 0$, and diagonalizing the Hamiltonian;

$$E^2(\mathbf{k}) = t^2 f^*(\mathbf{k})f(\mathbf{k}) = t^2(1 + e^{-i\mathbf{k}\cdot\mathbf{a}_1} + e^{-i\mathbf{k}\cdot\mathbf{a}_2}) (1 + e^{i\mathbf{k}\cdot\mathbf{a}_1} + e^{i\mathbf{k}\cdot\mathbf{a}_2})$$

$$E^2(\mathbf{k}) = t^2(1 + e^{ik_1a} + e^{ik_2a} + e^{-ik_1a} + 1 + e^{-i(k_1-k_2)a} + e^{-ik_2a} + e^{i(k_1-k_2)a} + 1),$$

$E(\mathbf{k}) = \pm t\sqrt{3 + 2\cos(\mathbf{k} \cdot \mathbf{a}_1) + 2\cos(\mathbf{k} \cdot \mathbf{a}_2) + 2\cos(\mathbf{k} \cdot (\mathbf{a}_2 - \mathbf{a}_1))}$, expressing in (x, y) components of k,

$$E(k_x, k_y) = \pm t\sqrt{1 + 4\cos\left(\frac{\sqrt{3}ak_y}{2}\right)\cos\left(\frac{ak_x}{2}\right) + 4\cos^2\left(\frac{ak_x}{2}\right)},$$

where with lattice constant $a = \sqrt{3}a_0$. This well-known dispersion relation is illustrated graphically in Figure 2a. At Brillouin zone boundaries, the function $f(k)$ goes to zero¹³². At K points, the solutions of the dispersion relation are degenerate giving zero bandgap between the valence band, and conduction band. Near K points, the transfer Hamiltonian is like the Dirac Hamiltonian, and the dispersion relation is approximately linear, which describes massless quasiparticles.¹³⁴ Monolayer graphene has a high carrier mobility due to its unique band structure, however, it doesn't have a band gap which limits its potential applications in solar cells and photovoltaic technology.

3.2 Electronic Band Structure of Bilayer Graphene in the Tight Binding

Approximation

For AB stacked or Bernal bilayer graphene, there are interlayer $2p_z$ orbital interactions between the atoms of the unit cell of the upper layer (1) and lower layer (2). In Figure 3.1b we illustrate the lattice structure of bilayer graphene along with the relative positions of atoms projected onto the x-y plane. In this bilayer structure, there are now clearly four distinct atoms (A1, B1, A2, and B2). Their electronic coupling can be approximated by considering the intralayer contributions (A1/B1, B1/B2), and the new nearest-neighbor interlayer contributions corresponding to A1/A2 and B1/B2 shown in

Figure 3.1b.¹³³ Taking four distinct atoms into account (A1, B1, A2, B2) in the tight binding model, Castro et al. and Neto et al. show that the Hamiltonian can be re-expressed as

$$\hat{H} = (-t) \sum_{\langle i,j \rangle} [a_i^\dagger b_j + a_j^\dagger b_i + \text{HC}] - \gamma \sum_{\langle i,j \rangle} [a_i^\dagger a_j + \text{HC}] + \varepsilon \sum_{\langle i,j \rangle} [a_j^\dagger a_j + b_j^\dagger b_j]^{4,5}$$

Here, ε represents the onsite energies, $-t = \langle \varphi_{A1} | \hat{H} | \varphi_{B1} \rangle$ is the intralayer transfer integral for electronic hopping between A1 to B1, and A2 to B2 and $-\gamma$ represents the hopping between A1 to A2 ($\langle \varphi_{A1} | \hat{H} | \varphi_{A2} \rangle$), and B1 to B2 ($\langle \varphi_{B1} | \hat{H} | \varphi_{B2} \rangle$).

Using the Fourier transformed operators;

$$a_i^\dagger(\vec{r}) = \frac{1}{\sqrt{N}} \sum_{\vec{k}} e^{-i\vec{k} \cdot \vec{r}_{Ai}} a_{\vec{k}}^\dagger, \quad b_i^\dagger(\vec{r}) = \frac{1}{\sqrt{N}} \sum_{\vec{k}} e^{-i\vec{k} \cdot \vec{r}_{Bi}} b_{\vec{k}}^\dagger, \quad \text{and defining vectors}$$

$$\vec{r}_{Ai} = \vec{R}_i^{A1}, \quad \vec{r}_{Bi} = \vec{R}_i^{A1} + \vec{r}_j, \quad \vec{r}_{A1} = \vec{R}_i^{A1} + \vec{r}_4 \quad \text{we can simplify,}$$

$$a_i^\dagger b_i = \frac{1}{N} \sum_{\vec{k}\vec{k}'} e^{-i\vec{k} \cdot \vec{R}_i^{A1}} a_{\vec{k}}^\dagger e^{i\vec{k}' \cdot (\vec{R}_i^{A1} + \vec{r}_j)} b_{\vec{k}'} = \frac{1}{N} \sum_{\vec{k}\vec{k}'} e^{-i(\vec{k} - \vec{k}') \cdot \vec{R}_i^{A1}} e^{i\vec{k}' \cdot \vec{r}_j} a_{\vec{k}}^\dagger b_{\vec{k}'} =$$

$$\frac{1}{N} N \delta_{\vec{k}\vec{k}'} e^{i\vec{k}' \cdot \vec{r}_j} a_{\vec{k}}^\dagger b_{\vec{k}'} = e^{i\vec{k} \cdot \vec{r}_j} a_{\vec{k}}^\dagger b_{\vec{k}}, \quad \text{similarly, we get,}$$

$$a_i^\dagger a_i = \frac{1}{N} \sum_{\vec{k}\vec{k}'} e^{-i\vec{k} \cdot (\vec{R}_i^{A1} + \vec{r}_4)} a_{\vec{k}}^\dagger e^{-i\vec{k}' \cdot \vec{R}_i^{A1}} a_{\vec{k}'} = e^{-i\vec{k} \cdot \vec{r}_4} a_{\vec{k}}^\dagger a_{\vec{k}}, \quad \text{and}$$

$$a_j^\dagger a_j = \frac{1}{N} \sum_{\vec{k}\vec{k}'} e^{-i(\vec{k} - \vec{k}') \cdot \vec{R}_i^{A1}} a_{\vec{k}}^\dagger a_{\vec{k}'} = a_{\vec{k}}^\dagger a_{\vec{k}},$$

with the simplified terms using equation 3.1, it has been shown the approximate Hamiltonian for bilayer graphene is,

$$\hat{H} = (-t) \sum_{\vec{r}_j} [e^{i\vec{k} \cdot \vec{r}_j} a_{1\vec{k}}^\dagger b_{1\vec{k}} + e^{i\vec{k} \cdot \vec{r}_j} a_{2\vec{k}}^\dagger b_{2\vec{k}} + e^{-i\vec{k} \cdot \vec{r}_j} b_{1\vec{k}}^\dagger a_{1\vec{k}} + e^{-i\vec{k} \cdot \vec{r}_j} b_{2\vec{k}}^\dagger a_{2\vec{k}}] - \gamma [e^{-i\vec{k} \cdot \vec{r}_4} a_{2\vec{k}}^\dagger a_{1\vec{k}} + e^{i\vec{k} \cdot \vec{r}_4} a_{1\vec{k}}^\dagger a_{2\vec{k}}] + \varepsilon [a_{1\vec{k}}^\dagger a_{1\vec{k}} + a_{2\vec{k}}^\dagger a_{2\vec{k}} + b_{1\vec{k}}^\dagger b_{1\vec{k}} + b_{2\vec{k}}^\dagger b_{2\vec{k}}];$$

which can alternately be expressed in matrix form as,

$$\hat{H} = \sum_{\vec{k}} (a_{1\vec{k}}^\dagger \ b_{1\vec{k}}^\dagger \ a_{2\vec{k}}^\dagger \ b_{2\vec{k}}^\dagger) \begin{pmatrix} \varepsilon_{A1} & -t\mathbf{f}(\mathbf{k}) & -\gamma & 0 \\ -t\mathbf{f}^*(\mathbf{k}) & \varepsilon_{B1} & 0 & 0 \\ -\gamma^* & 0 & \varepsilon_{A2} & -t\mathbf{f}(\mathbf{k}) \\ 0 & 0 & -t\mathbf{f}^*(\mathbf{k}) & \varepsilon_{B2} \end{pmatrix} \begin{pmatrix} a_{1\vec{k}} \\ b_{1\vec{k}} \\ a_{2\vec{k}} \\ b_{2\vec{k}} \end{pmatrix} \dots\dots\dots 3.2$$

Where, $f(\mathbf{k}) = e^{i\mathbf{k}\cdot\mathbf{r}_1} + e^{i\mathbf{k}\cdot\mathbf{r}_2} + e^{i\mathbf{k}\cdot\mathbf{r}_3}$, and $\varepsilon_{A1}, \varepsilon_{B1}, \varepsilon_{A2}$, and ε_{B2} are onsite energies on atomic sites A1, B1, A2, and B2 respectively. The nearest neighbor vectors are:

$$\mathbf{r}_1 = a_0 \left(\frac{1}{2\sqrt{3}}, \frac{1}{2}, 0 \right), \quad \mathbf{r}_2 = a_0 \left(\frac{1}{2\sqrt{3}}, -\frac{1}{2}, 0 \right), \quad \mathbf{r}_3 = a_0 \left(-\frac{1}{\sqrt{3}}, 0, 0 \right), \quad \mathbf{r}_4 = b_0(0,0,1); \text{ giving}$$

$$f(\mathbf{k}) = e^{\frac{ik_x a_0}{2\sqrt{3}}} \left(e^{\frac{iky a_0}{2}} + e^{-\frac{iky a_0}{2}} \right) + e^{-\frac{ik_x a_0}{\sqrt{3}}} = e^{\frac{ik_x a_0}{2\sqrt{3}}} 2\cos\left(\frac{ky a_0}{2}\right) + e^{-\frac{ik_x a_0}{\sqrt{3}}}$$

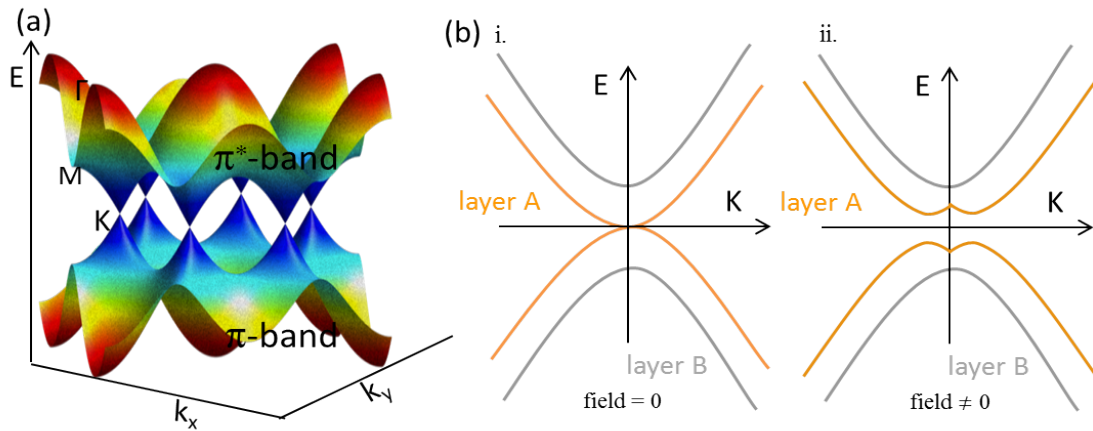


Figure 3.2: Band structure of graphene and bilayer graphene. (a) Representation of the band structure for single layer graphene. It shows linear bands for low energy. (b) The band dispersion shows quadratic bands near the K-point in bilayer graphene (i) without applied field, (ii) opening of a band gap upon applied vertical electric field.

The 2 X 2 blocks in the upper-left side and the lower-right side of the Hamiltonian in equation 3.2 represents the intralayer coupling, which looks similar to the monolayer Hamiltonian terms. The 2 X 2 blocks in the upper-right side, and the lower-left side of the

Hamiltonian represents interlayer coupling, where the parameter γ describes the coupling between orbitals A1, A2, and/or B1, B2.¹³⁵ The parameters $\gamma = 0.14$ eV, $t = 3.16$ eV, and $\epsilon_{A1}, \epsilon_{B1}, \epsilon_{A2}, \epsilon_{B2} = 0$ in equation (2) have been obtained using infrared spectroscopy.¹³⁶ The well-known free electron band structure of AB stacked bilayer graphene is roughly illustrated in the Figure 3.2b.

Without bias V , $2p_z$ orbital interactions between four atomic sites are responsible for four bands in the dispersion relation as shown in Figure 3.2b i, two for the conduction band, and two for the valence band. The valence band pairs and conduction band pairs are split by the amount of about 0.4 eV, which is an interlayer coupling energy. The splitting occurs due to the strong bonding, and anti-bonding between atomic orbitals A1, A2, and/or B1, B2. The hopping between A1, A2, and/or B1, B2 is responsible for low energy bands. The tight binding model is in good agreement with DFT calculations in the low energy limit.¹³⁷⁻¹³⁹ Wang et al. showed that with a potential bias V between two layers of graphene, it is further possible to see the shift in electrochemical potential between the layers as shown in Figure 3.2b ii.^{44,135,140}

3.3 Effective Free Electron Model: Electronic Band Structure of tBLG

Lastly, we complete our review of the free electron graphene models by considering of the structure of twisted bilayer graphene defined by two layers of AA stacked bilayer graphene rotated around a common site by an arbitrary angle θ . Random orientation in bilayer graphene is rarely obtained when exfoliated monolayer graphene occasionally fold over. As discussed in Chapter 1, tBLG is primarily acquired through CVD growth. There was some earlier theoretical interest looking at theta dependent band

structure properties.

The two lattice vectors for AA stacked bilayer graphene with $\theta = 0^\circ$ are just $\mathbf{a}_1 = a_0 (1,0)$ and $\mathbf{a}_2 = a_0 \left(\frac{1}{2}, \frac{\sqrt{3}}{2}\right)$. For non-zero angles the lattice vectors are more complicated because they must span the new superlattice, and are given stacking angle indexed vectors; $\mathbf{a}_1^1 = \mathbf{R}\left(-\frac{\theta}{2}\right)$, and $\mathbf{a}_1^2 = \mathbf{R}\left(\frac{\theta}{2}\right)$.¹⁴¹ Rotation angle $\theta = 0^\circ$ produces AA stacked bilayer graphene and $\theta = 60^\circ$ corresponds to AB bilayer graphene stacking. Rotation angle θ and $-\theta$ produce a similar band structure.

Physical structure with finite size until cell repeating infinitely is necessary for theoretical band structure calculation. However, tBLG does not have a periodic structure in general because of mismatch between the uniformity of layers with respect to each other. One way to define tBLG structure is taking a Bernal stacked bilayer graphene and rotating one layer by an angle θ with respect to the other layer followed by translation of the top layer by an arbitrary vector. This process can define tBLG commensurate structure with periodic unit cell as well as tBLG incommensurate structure with no unit cell defined.

The structure is periodic also known as commensurate structure only for some special angles with a well-defined unit cell. Such a periodic lattice structure (commensurate) of tBLG for rotation angles $\theta = 21.8^\circ$, and $\theta = 9.4^\circ$, $\theta = 3.9^\circ$ is shown in Figure 3.1d-f. Many other θ values provide tBLG structures with thousands of atoms and for every commensurate tBLG structure there many incommensurate structures. This limits band structure calculations for all possible angles with some standard computation procedures. Since a small variation in angle would result in a completely different unit

cell, it is important to define a rigid unit cell for theoretical calculations. However, as shown by Brown et al. with DF-TEM images of CVD grown tBLG¹²⁵, there could be some spatial variation of fraction of a degree, so to best experimentally define the angle an average value should be taken in to account.

When the rotation angle is small, the interference between two lattice vectors in two layers gives rise to the pattern called the ‘moiré pattern’ with periodicity inversely proportional to θ .¹⁴¹ The unit cell is relatively big for small rotation angles as seen in Figures 3.1e-f. The plot of unit cell size vs. θ for tBLG structure is shown in Figure 3.3 which shows how the unit cell size increases rapidly when θ approaches 0° or 60° due to large periodicity of the ‘moiré pattern’.¹⁴¹ The lattice vectors for a given angle are:

$$\mathbf{L}_1 = m\mathbf{a}_1^1 + n\mathbf{a}_2^1; \text{ (for layer 1),; (for layer 2) } \mathbf{L}_2 = R\left(\frac{\pi}{3}\right)\mathbf{L}_1 \text{ and the lattice constant is}$$

$$L = |\mathbf{L}_1| = |\mathbf{L}_2| = \frac{|m-n|a}{2\sin\left(\frac{\theta}{2}\right)}, \text{ where } m, n \text{ are integers.}^{142}$$

For electronic states near the Fermi level, only p_z orbitals needs to be taken into account in the tight binding model. For twisted bilayer graphene, neighbors are rotated with respect to each other (unlike Bernal AB stacking). Therefore, we now have to consider both the $pp\pi$ and the $pp\sigma$ terms to account for the new interlayer interactions between atomic orbitals. As shown by Shallcross et al.,^{48,141} the Hamiltonian can be written as,

$$\hat{H} = (-1) \sum_{\langle i,j \rangle} t(R_i - R_j) |R_i\rangle \langle R_j| + \text{HC} \dots\dots\dots 3.3$$

where, $t(R_i - R_j)$ is the transfer integral. The transfer integral matrix equations for each

type of interlayer orbital interactions are given by: $V_{pp\pi} = -\gamma_0 e^{q\pi\left(1 - \frac{d}{a_0}\right)}$, and $V_{pp\sigma} =$

$\gamma_1 e^{q_\sigma \left(1 - \frac{d}{a_1}\right)^{26}}$, with the ratio $\frac{q_\sigma}{a_1} = \frac{q_\pi}{a_0}$. Where, a_0 is the nearest neighbor distance, a_1 is the interlayer distance, d is the distance between two orbitals, γ_0 is the transfer integral between nearest neighbors, and γ_1 is the transfer integral between nearest neighbor atoms that are located vertically. Combining these terms, the combined transfer integral is; $-t(\mathbf{R}_i - \mathbf{R}_j) = V_{pp\pi} \left[1 - \left[\frac{(\mathbf{R}_i - \mathbf{R}_j) \cdot \mathbf{z}}{d} \right]^2 \right] + V_{pp\sigma} \left[\frac{(\mathbf{R}_i - \mathbf{R}_j) \cdot \mathbf{z}}{d} \right]^2$ with, $a_0 \approx 0.14 \text{ nm}$, $a_1 \approx 3.35 \text{ \AA}$, $d \approx 0.335 \text{ nm}$, $\gamma_0 \approx 2.7 \text{ eV}$, $\gamma_1 \approx 0.48 \text{ eV}$, as obtained from literature²⁶. Using the above transfer integral, the dispersion relation can be obtained from the determinant of the Hamiltonian of equation 3.3.¹⁴³ A rough illustration of the resulting free electron interlayer band structure of tBLG is shown in Figure 3.3b. There is an anti-crossing where bands of two layers meet. This anti-crossing is a result of interlayer interactions between the layers.

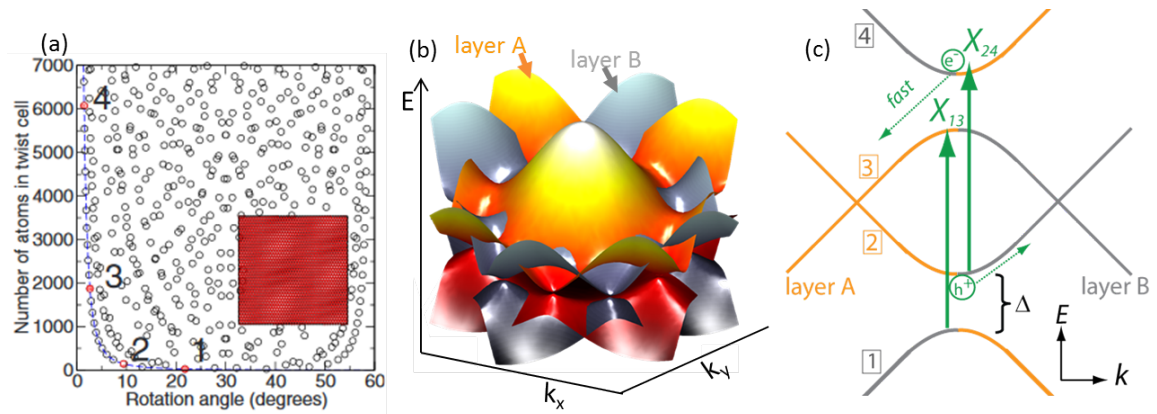


Figure 3.3: (a) Unit cell size as a function of twist angle. The lower bound for the unit cell size increases rapidly as angle decreases. Inset shows the moiré pattern for labeled cell, [Adapted from¹⁴¹.] (b) tBLG free electron band-structure. (c) Cross-sectional view of tBLG shows vHs transitions X_{13} , X_{24} between avoided crossing regions.

Figure 3.3c sketches the cross-section view of the band structure, showing the van Hove

singularity (vHs) transitions X_{13} and X_{24} . The bands near K, and K' come from single layer graphene (layer 1, and layer 2), and they are folded into the same Brillouin zone. These bands don't mix with each other giving rise to the linear dispersion relation near K, and K'. Near the M point, there is a splitting in energy due to anti-crossing of the bands. The allowed optical transitions are also shown. The band structure of tBLG for different rotation angles look similar, however, the overall energy decreases by minimizing the rotation angle. The splitting energy near the M-point is of the order of interlayer coupling between the two layers, which is about 0.2 eV for all possible rotation angles.¹³² Majority of early theoretical and experimental studies found that most properties of tBLG changes smoothly with angle θ .^{48,141,144,145} For rotation angles $< 1^\circ$, parabolic dispersion is obtained. For rotation angles around 1° , the bands are flat near the Fermi level. There is a transition from parabolic to linear dispersion for rotation angles $1^\circ \leq \theta \leq 2^\circ$. For angles above 10° and up to the symmetric point of 30° , the dispersion is linear as in single layer graphene at the K point.¹⁴⁶ Although computations can only be performed on a small unit cell tBLG with specific angles, the results gained from the calculations can be extended to understand properties of other angles in tBLG.^{48,142}

3.4 Bound Exciton Model for tBLG

3.4.1 Excitonic Effects in Nanomaterials

In some low dimensional materials such as metallic single walled carbon nanotubes¹⁴⁷ and monolayer graphene,^{41,42,148} it has been shown that the line-shape of the optical absorption does not follow the single particle, free electron model. This can be explained by considering electron-hole interactions or excitonic effects while modeling.

Generally, metallic materials are thought to have a strong electron coupling with the lower lying continuum states making it almost impossible to have excitonic features. The excitonic effects are very strong in a low dimensional system due to confinement and reduced screening. As a consequence, even a metallic system, graphene has a rather large exciton band renormalization near M-point as shown in Figure 3.4 at 4.6 eV. As shown in Figure 3.4, the model that takes into account e-h interactions better fits the data.^{41,42,148}

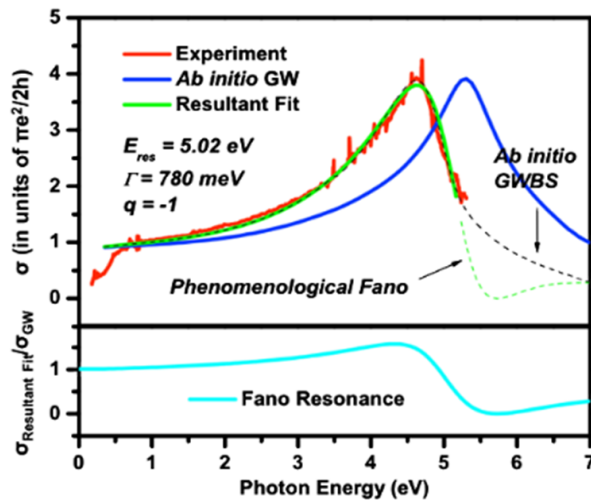


Figure 3.4: Excitonic effects in graphene. The experimental optical conductivity of graphene in red shows saddle point excitonic effect. AB initio GWBS (dashed black) and phenomenological Fano (green) provides best fit to the data (red) Fano model fitting from GW calculations in green. [Adapted from⁴¹.]

3.4.2 Fano Resonance and Bound Excitons

The asymmetric peak is the best fit to a Fano model. Fano resonance arises when slow varying background also known as continuum interferes with a narrow-band resonance or bound state. The amplitude and phase of this background scattering vary much slowly with energy than the resonant scattering near resonant energy. This

variation and interference create an asymmetric line profile, which is a characteristic of a Fano resonance.²³ To fit the data in Figure 3.4, the model considers excitons as discrete states that are coupled to the lower lying continuum of single particle states resulting in an asymmetric line-shape owing to the band renormalization. These are resonant exciton states known as Fano resonance. Fano resonance effect has been observed in various nanomaterials, such as carbon nanotubes, graphene, nanoparticle assemblies.^{41,150,151}

Early work on tBLG with STM shows vHs as sharp peaks in the density of states as a function of energy (see Chapter 2).¹²⁵ They experience 20% enhancement in the oscillator strength and are responsible for angle dependent optical response in tBLG. As shown by Havener et al,¹⁵² optical absorption of tBLG shows that the spectrum is better modeled if excitonic effects are considered in the calculations. The question remains: are the excitons in tBLG resonant or bound? The excitons in monolayer graphene are resonant, so the eigenstates are delocalized, and short lived. Bound excitons are localized and have long lifetimes. Long lifetimes are important for higher efficiency devices in solar or photovoltaic technology. However, a metallic system is not expected to have bound excitons due to large screening effects.

To answer the question theoretically if tBLG has bound or resonant excitons and can be used for higher efficiency devices,¹⁵³ calculated spatial wave functions of various excitonic states in tBLG. Their results suggest that the excitons associated with the absorption resonance peak are resonant, and in addition to the resonant states, there are bound exciton states located ~ 400 meV below the absorption resonance. This was unexpected due to scattering between the discrete states and the lower lying continuum states.

We will now discuss the details of modeling excitonic effects in tBLG upon photoexcitation. Upon photoexcitation of tBLG, exciton effects may manifest themselves owing to Coulombic interactions of e-h pairs. To theoretically model the many-body excitonic effects, it is necessary to solve the BSE as shown by Rohlfing et al.¹⁵⁴: $(E_{ck} - E_{vk})A_{vck}^S + \sum_{v'c'k'} \langle vck | K^{eh} | v'c'k' \rangle A_{v'c'k'}^S = \Omega^S A_{vck}^S$, where, A_{vck}^S is the exciton wave function in k-space, Ω^S is the exciton eigenenergy, K^{eh} is the e-h interaction kernel, and $|vk\rangle, |ck\rangle$ are the hole and electron states, respectively.

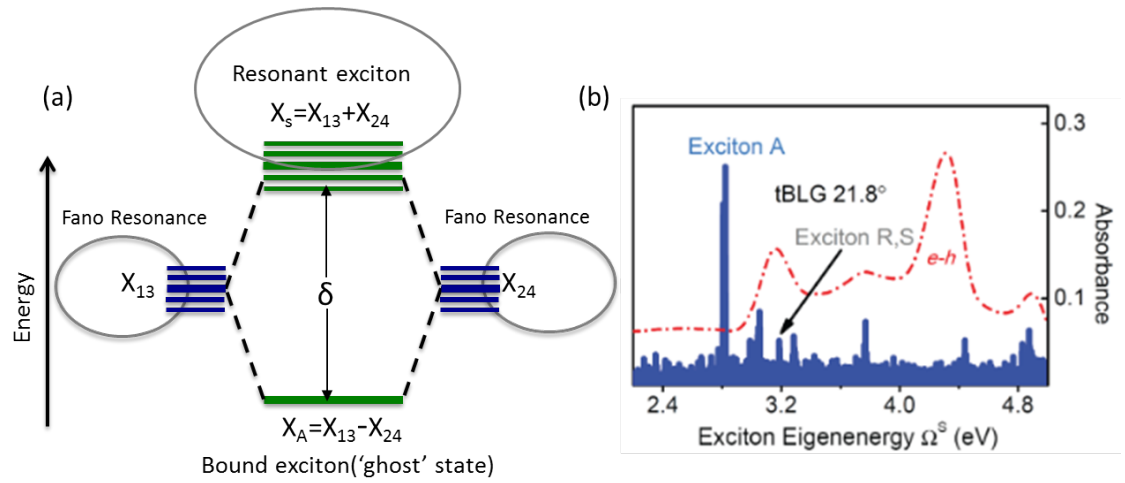


Figure 3.5: Bound Exciton model. (a) Upon resonant optical excitation, degenerate Fano resonance states X_{13} and X_{24} rehybridize producing a higher energy resonant exciton state X_s and lower energy bound exciton state X_A . (b) e-h attractive energy spectrum shows prominent spikes corresponding to resonant excitons labeled R, S and bound excitons labeled A below absorption resonance for 21.8° domain. Red shows calculated absorption spectrum. [Adapted from ¹⁵³.]

In order to predict possible bound exciton states, it is important to know the e-h attractive energy E_a^S , which roughly corresponds to the binding energy, and recently the first-principle BSE simulations in Liang et al.¹⁵³ reported that $E_a^S = 0.5$ eV for 21.8°

tBLG. Specifically, Liang et al. solved for

$E_a^S = \langle S | K^{eh} | S \rangle = \sum_{vck} (E_{ck} - E_{vk}) |A_{vck}^S| |A_{vck}^S| - \Omega^S$, which is the net exciton kinetic energy plus the weighted single-particle band energy difference between electrons and holes.¹⁵³ To simplify the direct analysis of the first principle BSE simulation, low-energy effective model is often further assumed, giving a simpler perturbed Hamiltonian that is analogous to Equation (1), specifically;¹⁵⁵

$$H(k) = \begin{pmatrix} H_0(k, 0) & T^+ \\ T & H_0(k - \Delta K, \theta) \end{pmatrix}, \text{ with}$$

$$H_0(k, 0) = \hbar v_F \begin{pmatrix} 0 & e^{-i\theta}(k_x - ik_y) \\ e^{i\theta}(k_x + ik_y) & 0 \end{pmatrix}, \text{ where } T = \Delta \begin{pmatrix} 0 & 1 \\ 1 & 0 \end{pmatrix} \quad (4)$$

The average interlayer interaction between AB and BA stacking order is described by matrix T with interlayer coupling strength Δ . The low-energy effective model is best for small-twisting angles because the linear Dirac-Fermion dispersion is preserved. Using the BSE and the low effective model, Liang et al.¹⁵³ found that upon resonant excitation of tBLG, you can access degenerate Fano resonant transitions X_{13} , X_{24} shown in Figure 3.3c which then effectively rehybridize as depicted in Figure 3.5a. The symmetric superposition of the two degenerate transitions give rise to a higher energy state and anti-symmetric superposition give rise to the lower energy state ('ghost' state, see Figure 3.5). The constructive interference couples with the lower lying continuum, which broadens the resulting resonant bright excitonic state. The antisymmetric superposition cancels the coupling between the lower lying continuum making it a localized bound excitonic state. The so-called ghost Fano resonance effect was found in quantum dot molecules.¹⁵⁶ The Fano resonant exciton states are found to be optically bright states, and the bound exciton

state is optically dark state. The dark state cannot be accessed directly with 1-ph excitation, however, multi-photon optical excitation or magnetic field can be used to access the dark state. For the scope of this research, multi-photon TA microscopy measurements were performed to explore the existence of the dark state experimentally as discussed in Chapter 4.

This model is appropriate for small twist angle, however, the double resonance of transitions and the destructive interference plays crucial role in existence of strongly bound excitons.¹⁵³ The formation mechanism of this dark state X_A is very general, and may hold exciting promise for other twisted stacked 2D vdW materials.

4. TUNABLE OPTICAL EXCITATIONS IN TWISTED BILAYER GRAPHENE FORM STRONGLY BOUND EXCITONS

Hiral Patel, Robin W. Havener, Lola Brown, Yufeng Liang, Li Yang, Jiwoong Park,
and Matt W. Graham

Nano Letters, **2015**, 15, pp 5932-5937

When two sheets of graphene stack in a twisted bilayer graphene (tBLG) configuration, the resulting constrained overlap between interplanar 2p orbitals produce angle-tunable electronic absorption resonances. By applying a novel combination of multiphoton transient absorption (TA) microscopy and TEM, we resolve the electronic structure and ensuing relaxation by probing resonant excitations of single tBLG domains. Strikingly, we find that the transient electronic population in resonantly excited tBLG domains is enhanced many fold, forming a major electronic relaxation bottleneck. 2-photon TA microscopy shows this bottleneck effect originates from a strongly bound, dark exciton state lying ~ 0.37 eV below the 1-photon absorption resonance. This stable coexistence of strongly bound excitons alongside free-electron continuum states has not been previously observed in a metallic, 2D material.

4.1 Introduction

This Chapter is largely adapted from H. Patel *et al.*, “Tunable optical excitations in twisted bilayer graphene form strongly bound excitons”, *Nano Letters*, 15, 5932-7. Here, we discuss the multi-photon ultrafast transient absorption microscopy study of single grain twisted bilayer graphene for the first time and show the formation of bound excitons upon resonant excitations.

Photoexcited electrons in graphene relax energetically far faster than the e-h separation timescale, making many electronic and optoelectronic applications prohibitive.^{143,157–159} While similar fast, picosecond relaxation timescales are also observed in Bernal stacked bilayer graphene (bBLG)¹⁶⁰, slower relaxation might be possible in twisted bilayer graphene (tBLG). In tBLG, an off-axis interlayer twist angle (θ) gives rise to band anticrossings and van Hove singularities (vHs, Figure 4.1b).^{68,125,161} Near such vHs, previous studies show that optical absorption increases by $\sim 20\%$ and is peaked at an energy, E_θ .^{46,47,68,125,129,152,162–166} This absorption resonance peak increases monotonically with θ (see Chapter 2).³⁸ To date however, the properties of photoexcited electrons in vHs remain unexplored beyond the Raman and linear absorption characterization. Here, we apply space, time, and energy-resolved 1-photon (1ph) and 2-photon (2-ph) transient absorption (TA) microscopy to both spectrally map the excited state electronic-structure of tBLG and image the ensuing electronic dynamics.

4.2 Free Electron Vs. Bound Exciton Model

The single-particle band structure for tBLG can be understood by superimposing two graphene Brillouin zones, rotated by a twist angle θ , as shown in Figure 4.1a.^{167,168}

The vertical line cutting through the two Dirac points of the graphene layers (Figure 4.1b) shows the band anticrossing near the degeneracy with an energy splitting (Δ), and four possible vHs transitions between the graphene sub-bands labeled 1 through 4. These optical transitions experience a large joint density of states between the valance bands (1 & 2) and the conduction bands (3 & 4), but only 1 \rightarrow 3 (denoted X_{13}) and 2 \rightarrow 4 (X_{24}) transitions are allowed due to selection rules.^{48,152}

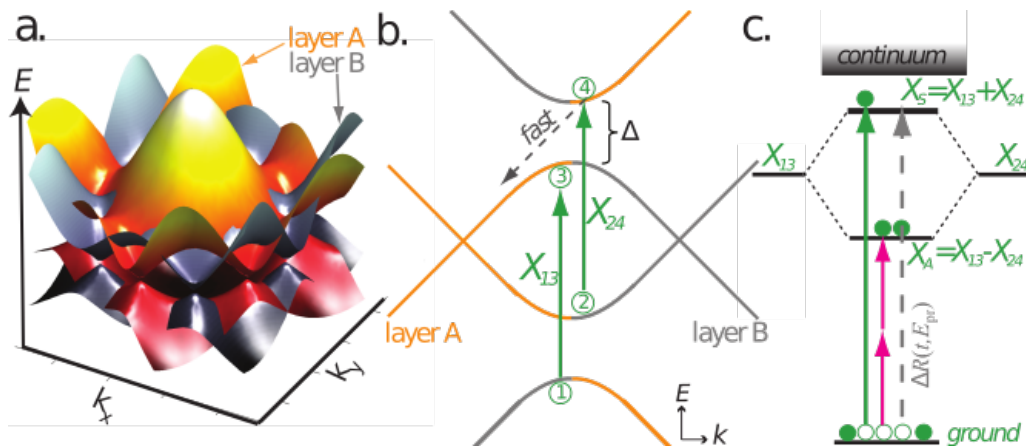


Figure 4.1: (a) tBLG free-electron interlayer band-structure. (b) Cross-sectional view interlayer vHs resonances, X_{13} and X_{24} , between band anti-crossing regions. (c) Alternatively, the degenerate X_{13} and X_{24} states may rehybridize, giving a 1-ph state above, and a 2-ph allowed exciton state below. TA (arrows) interrogates the electronic population (circles).

Outwardly, the X_{13} and X_{24} transitions shown in Figure 4.1b are degenerate vHs similar to graphene's M-point saddle-point exciton.^{41,48,167,168} In this case, Coulombic attraction between e-h pairs would augment both X_{13} and X_{24} transition energies and produce an asymmetric, Fano optical lineshape.^{150,169} Since such unbound Fano excitons couple to continuum states of graphene,¹⁶⁹ this model predicts the 1-ph TA response from

tBLG will decay quickly, with an amplitude and rate similar to single-layer graphene (dotted arrow in Figure 4.1b).

Alternatively, previous studies suggest that inclusion of bound-exciton effects are necessary to simulate the nearly gaussian tBLG optical absorption lineshape.^{38,153} While one can consider unbound excitonic states for X_{13} and X_{24} independently, such a picture is incomplete because the two states occur at the same energy and momentum, a direct result of the electron-hole symmetry at the vHs in tBLG. A more complete description was given in recent work reported by Liang et al. that predicts formation of stable, strongly bound ($E_B \sim 0.5$ eV) excitons.¹⁵³ These first-principles calculations suggest that interlayer excited states in tBLG are better described by renormalized symmetric ($X_S = X_{13} + X_{24}$) and anti-symmetric ($X_A = X_{13} - X_{24}$) excitonic states.¹⁵³ In this model, illustrated in Figure 4.1c, X_S corresponds to the optical tBLG resonance at E_θ , and is an unstable exciton.^{38,68} Conversely, X_A is only 2-ph accessible and is calculated to be a strongly-bound, localized excitonic state.¹⁵³ The remarkable stability predicted for the X_A state results from the deconstructive coherence between the two degenerate Fano resonances rigorously canceling coupling with graphene continuum states. Such a state is termed a 'ghost Fano' resonance. While similar phenomena have been weakly observed in quantum dot and carbon nanotube systems, such strongly bound exciton states have never been observed in a 2D metallic system.^{153,156,170} If such ghost Fano excitons are present in tBLG, weak exciton-continuum coupling is expected to enhance the local electronic population, giving longer relaxation dynamics for the 1-ph (X_S) and 2-ph (X_A) TA response.

4.3 TA Microscopy on Single tBLG Domains

In this work, we obtain the TA spectra and dynamics of single tBLG domains, and map out the different 1-ph and 2-ph electronic transitions predicted by the contrasting vHs and strongly-bound exciton models in Figure 4.1. We further correlate ultrafast TA microscopy with the precise local atomic stacking and grain boundaries, by employing darkfield TEM to definitively assign a twist angle to the absorption resonance, E_θ .¹⁷¹ Our experimental TA microscopy approach is outlined in Figure 4.2a.

The 1-ph TA map in Figure 4.2a shows a prominent patch of 6.8° oriented tBLG that is surrounded by non-twisted CVD graphene on a silicon nitride membrane substrate. This map was obtained by raster scanning a diffraction-limited pump and probe pulse pair over the graphene. We tuned our 140 fs pump pulse to be resonant with the 6.8° domain at $E_{\text{pump}} \sim E_\theta \sim 1.3$ eV. After a delay time t , we detect the differential TA ($\Delta R(t) \propto \Delta \sigma(t)$) (see Chapter 2 and Section 4.9) of a collinear probe pulse and construct time-dependent TA maps point-wise. Using probe energies ($E_{\text{pr}}=0.8$ eV) well below the resonance E_θ , in Figure 4.2a graphene gave an interband decreased absorption response (i.e. Pauli blocking of probe beam) everywhere at all time delays.

4.4 Electronic Relaxation Bottleneck

Our TA maps can be interpreted as 'movie frames' that closely approximate the relative photoexcited electronic population at a particular probe energy and time-delay (see Chapter 2). The 6.8° tBLG region labeled in Fig. 4.2a has a \sim two-fold stronger TA Pauli blocking response than the adjacent 0° stacked regions. However, the corresponding

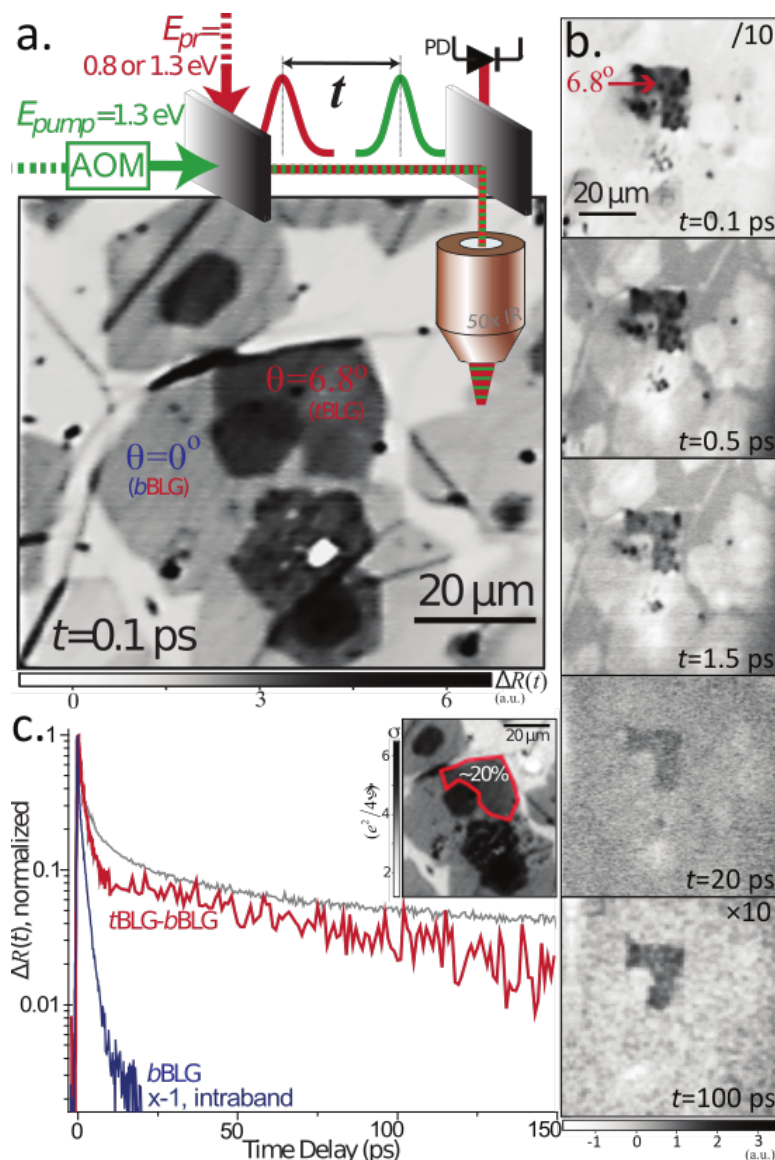


Figure 4.2: tBLG electronic relaxation bottleneck. (a) Ultrafast scanning TA microscopy of multilayer graphene. The TA Pauli blocking response is $> 2 \times$ enhanced for the 6.8° tBLG domain. (b) On-resonance TA maps at $E_{\text{pump}} \sim E_{\text{pr}} = E_\theta$ show a TA response localized to the 6.8° domain is present for $t > 100 \text{ ps}$. The surrounding graphene gives only a weak transient intraband response (opposite sign). (c) TA relaxation kinetics of the bBLG and tBLG regions labeled (vs. SWNT E_{11} state, gray). Corresponding linear absorption map at 1.3 eV shows tBLG (red) is only $\sim 20\%$ stronger than in bBLG (inset).

linear absorption map in Figure 4.2c only shows a $\sim 20\%$ resonant enhancement. To account for this discrepancy, electrons in interlayer tBLG avoided crossing regions must relax much slower than the surrounding non-twisted graphene bilayers, suggesting an intrinsic electronic relaxation bottleneck.

In Figure 4.2b, we repeat the 1-ph measurement but instead resonantly probe the electronic population at E_0 ($E_{\text{pump}}=1.33$ eV, $E_{\text{pr}}=1.26$ eV probe). Compared against the corresponding linear absorption map in Figure 4.2c (inset), the TA maps differ in both sign and absolute amplitude. Strikingly, only the 6.8° tBLG domain gives a strong TA Pauli blocking response. Meanwhile, the surrounding graphene in Figure 4.2b gives a weak, short-lived graphene intraband TA response signified by its opposite sign. This suggests that interlayer tBLG electrons are decoupled from the intraband transient response that dominates the TA map everywhere else in Figure 4.2b. Surprisingly, the subsequent TA movie frames show excited carriers are present even >100 ps after initial excitation. Both observations definitively show that interlayer electrons excited at E_0 experience a major bottleneck restricting electronic relaxation. Such a strong and long-lived electronic signal in tBLG disagrees with the continuum Fano resonance model (Figure 4.1b), but can be explained by an excitonic model (Figure 4.2c) where weak exciton-continuum coupling allows for stable exciton formation.¹⁵³

To isolate the relaxation rates intrinsic to interlayer tBLG electrons excited at E_0 , we plot tBLG-bBLG (red) in Figure 4.2c by subtracting the much weaker (and opposite signed) intralayer electronic TA response (blue). A similar approach has been previously used to decouple linear absorption spectra, as $\sigma_{\text{tBLG}} - \sigma_{\text{BLG}}$.^{46,152} A least-squares deconvolution exponential fit of the kinetic decay requires only a biexponential fit that

decays with lifetimes of 1.4 ± 0.1 ps and 66 ± 4 ps. These lifetime components are remarkably long for any electronic state within a metallic system.

If electronic carriers in tBLG are unbound excitons, the TA (red) in Figure 4.2c must relax at a rate similar to bBLG (navy), providing that phonons with $E > \Delta$ (dotted arrow in Figure 4.2b) are available to scatter carriers through the anti-crossing gap (Δ) illustrated in Figure 4.1b.¹⁴³ Comparison of the short-time tBLG kinetics against bBLG in Figure 4.2c (red) reveals the absence of the dominant fast sub-ps electron relaxation components associated with graphene electron thermalization and optic phonon emission.⁴⁷ Remarkably, the shortest interlayer tBLG lifetime is 1.4 ps, which is similar to graphene's rate-limiting relaxation rate that is often associated with disorder-assisted or supercollision relaxation.^{143,172} The absence of the sub-ps relaxation processes, and the emergence of this long ~ 66 ps decay in tBLG relaxation kinetics, suggests that some electrons are decoupled from graphene's continuum states, as predicted by the strongly bound exciton model.¹⁵³

The unexpected TA bottleneck we observe in tBLG may be compared against semiconducting single-walled carbon nanotubes (SWCNTs), a similar carbon system with constrained 2p orbital interactions. It is established that SWCNTs have 1-ph and 2-ph excitonic states resulting from (chiral) angle dependent overlapping 2p orbitals.^{173–175} Figure 4.2c (gray) directly compares the E_{11} exciton relaxation rate of (6,5) chirality SWCNTs against tBLG (red). While the short time behavior differs greatly, Figure 4.2c shows the longer components of both traces decay at a similar rate, suggesting that the dynamic phonon environment causing E_{11} exciton relaxation in SWCNTs might be of a

similar nature to the interlayer exciton-phonon interactions causing exciton relaxation in tBLG.

4.5 One and Two Photon TA Spectrum and Maps

We can better distinguish between competing vHs and bound exciton models outlined in Figure 4.3a, by exploiting the 2-ph selection rules required for the predicted dark tBLG exciton state, X_A .^{48,153} To search for possible dark state transitions, we used a different sample of CVD bilayer graphene. The linear absorption map shown in Figure 4.3b (inset) reveals a series of tBLG domains with twist angles of either $\sim 6.5^\circ$ (yellow) or $\sim 8^\circ$ (red), corresponding to $E_\theta \sim 1.25$ eV and 1.52 eV respectively. Figure 3b plots the 2-ph TA spectrum obtained using IR pump energies ranging from $E_{\text{pump}} = 0.49$ to 1.15 eV, and a 8° resonant probe at $E_\theta \sim E_{\text{pr}} = 0.56$ eV. We observe two clear TA peaks centered at 1.18 eV and 1.82 eV that originate from resonantly enhanced 2-ph absorption. Specifically, as illustrated in Figure 4.3ai, we observe these dark states through resonant 2-ph enhanced Pauli blocking of the depleted ground state. Moreover, our ability to probe electronic population of optically dark state requires that X_S and X_A states share a common ground state; an inherent feature of a bound exciton model.¹⁷⁵ tBLG exciton state, X_A .^{48,153} To search for possible dark state transitions, we used a different sample of CVD bilayer graphene. The linear absorption map shown in Figure 4.3b (inset) reveals a series of tBLG domains with twist angles of either $\sim 6.5^\circ$ (yellow) or $\sim 8^\circ$ (red), corresponding to $E_\theta \sim 1.25$ eV and 1.52 eV respectively. Figure 4.3b plots the 2-ph TA spectrum obtained using IR pump energies ranging from $E_{\text{pump}} = 0.49$ to 1.15 eV, and a 8°

resonant probe at $E_\theta \sim E_{pr} = 0.56$ eV. We observe two clear TA peaks centered at 1.18 eV and 1.82 eV that

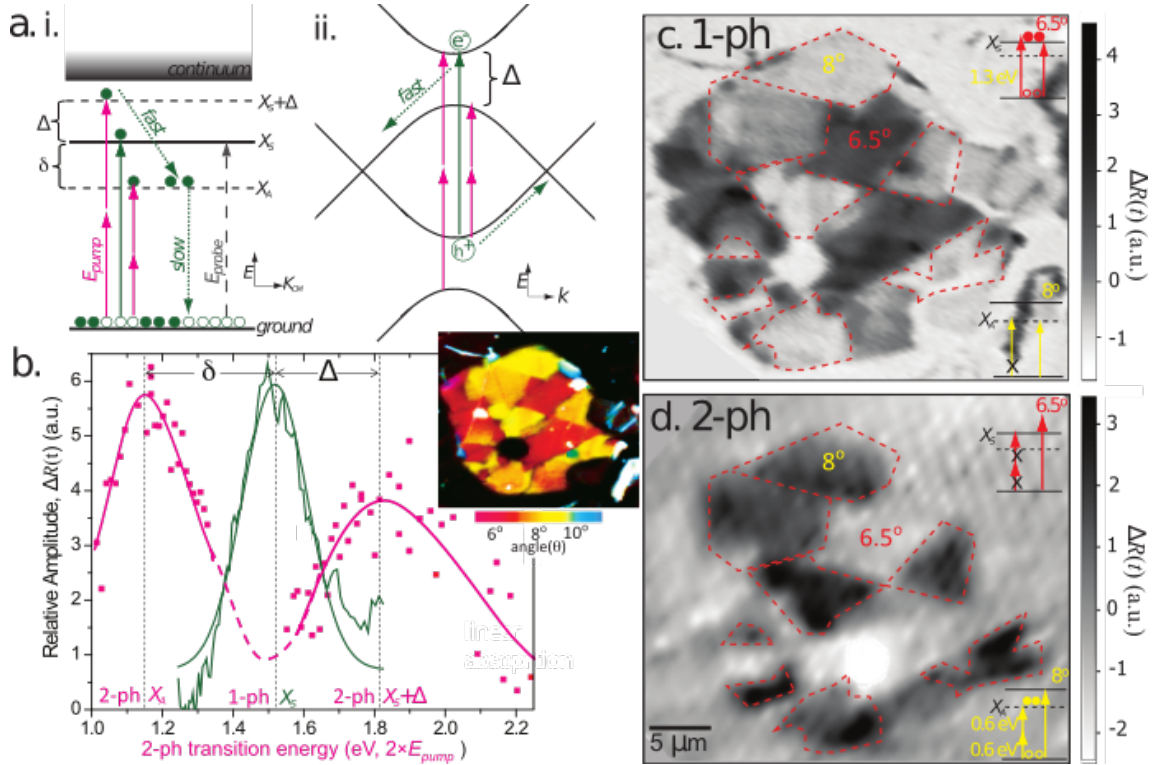


Figure 4.3: 1 photon vs. 2 photon absorption of $\sim 6.5^\circ$ and $\sim 8^\circ$ tBLG domains. (a) Competing models; (i.) bound exciton model, (ii.) continuum model. (b) 8° tBLG 2-ph transition TA spectrum (magenta), and 1-ph linear absorption spectrum (green, $\sigma_{tBLG} - \sigma_{bBLG}$). The first 2-ph peak fits best to a Gaussian lineshape centered at $\delta = 0.37$ eV below E_θ , the second peak has a Fano lineshape centered at $\Delta = 0.33$ eV above. (inset, map of the tBLG absorption resonance vs. twist angle) (c) 1-photon TA map, at $E_{pump} = 1.3$ eV shows a strong electronic bleach only from the resonantly excited 6.5° domains. (d) Conversely, a 2-ph TA map at $E_{pump} = 0.6$ eV shows a ground state bleach only from the 8° domains (dotted outlines). Combined, these maps demonstrate that the (X_S) state is 1-ph allowed and (X_A) state is only 2-ph allowed.

originate from resonantly enhanced 2-ph absorption. Specifically, as illustrated in Figure 4.3ai, we observe these dark states through resonant 2-ph enhanced Pauli blocking of the

depleted ground state. Moreover, our ability to probe electronic population of optically dark state requires that X_S and X_A states share a common ground state; an inherent feature of a bound exciton model.¹⁷⁵

The lowest peak in Figure 4.3b indicates that enhanced 2-ph absorption took place via a discrete, low-lying transition centered at 1.18 eV. Comparing the 2-ph peak against the 1-ph absorption resonance at $E_0 = 1.52$ eV (green, Figure 4.3b), we readily obtain the energy-state splitting parameters of $\delta = 0.37$ eV and $= 0.33$ eV. This 0.37 eV energy splitting closely matches the theoretically predicted $\delta \approx 0.4$ -0.5 eV, state splitting calculated for 21° tBLG.¹⁵³ Such a large bright-dark state energy splitting is much greater than the analogous state splitting in SWCNTs, and explains why photoluminescence has not yet been observed from resonantly excited tBLG domains.

To completely map the selection rules associated with tBLG electronic transitions, we compare the 1- and 2-ph TA microscopy response of 6.5° and 8° oriented domains in Figure 4.3c-d. Figure 4.3c maps-out the 1-ph TA response for $E_{\text{pump}} = 1.3$ eV, $E_{\text{pr}} = 1.2$ eV at $t = 0.3$ ps. Despite the X_A state being 1-ph resonant with the $\sim 8^\circ$ tBLG (dotted red outlines), we observed only a weak intraband response as was seen for bBLG regions previously (Figure 4.2b). This confirms that the X_A transition is not 1-ph accessible. In contrast, the 6.5° tBLG domains give a strong Pauli blocking response because E_{pump} is resonant with X_S .

2-ph resonant transitions of single tBLG domains are imaged in Figure 4.3c, by tuning our pump pulse energy to roughly half the predicted 8° X_A state energy (see Figure 4.3a), or $E_{\text{pump}} = 0.6$ eV. Comparison of the TA maps in Figure 4.3c against 3d show all of the 8° tBLG domain excitations that were forbidden under 1-ph excitation conditions

are now allowed for a 2-ph excitation. Conversely, all the 6.5° tBLG domain excitations that were observed under 1-ph excitation conditions now appear dark (inaccessible) under two-photon excitation. Using state parity, we assign the two-photon accessible dark states in Figure 4.3d to electronic carriers populating the X_A state of 8° tBLG. Together, Figure 4.3c and 4.3d show that the X_S bright state is two-photon forbidden, and the dark X_A state is only two-photon allowed. These strongly enforced selection rules follow the parity expectations of a roughly hydrogenic-like, strongly-bound exciton model advocated by recent first-principle simulations.¹⁵³

The 2-ph spectral peak centered at 1.82 eV in Figure 4.3b has not been previously predicted or observed. This peak has a broader, asymmetric shape, that fits better to a Fano lineshape expected from the unbound exciton model.^{41,42} In contrast, the other 1-ph and 2-ph peaks in Figure 4.3b fit best to a gaussian lineshape, a common characteristic of bound excitonic transitions. Accordingly, we infer that the two-photon absorption near 1.82 eV is best assigned to an unbound state transition labeled $X_S+\Delta$ in Figure 4.3ai. Conversely, the two-photon absorption resonance lying $\delta = 0.37$ eV below is best characterized as the X_A bound exciton or ghost Fano resonance peak predicted by Liang et al.¹⁵³ as supported by (i.) its asymmetric energy spacing (i.e. δ vs. Δ), (ii.) Gaussian lineshape, (iii.) long electronic lifetime and (iv.) parity enforced two-photon selection rules for the X_A and X_S transitions.

Using both explicit calculations based on the Bethe-Salpeter equation and effective low-angle continuum model, Liang et al. predicted radically different electronics properties emerging for both the theorized X_S and X_A exciton states.¹⁵³ Specifically, the symmetric X_S state was found to have delocalized wavefunctions and a

negligible binding energy. Conversely, the antisymmetric state X_A is predicted to be optically dark, insensitive to e-h charge screening, and strongly bound.¹⁵³ While certain phonons can scatter bound excitons into the lower-lying continuum states, the exciton-continuum coupling for the X_A is predicted to be vanishingly small, and roughly intensive to charge screening effects.¹⁵³ Accordingly, both theory and our TA microscopy now support that fast exciton dissociation becomes unfavorable in the X_A state of tBLG, enabling stable and meta-stable bound exciton states to form.

4.6 One and Two Photon Relaxation Kinetics

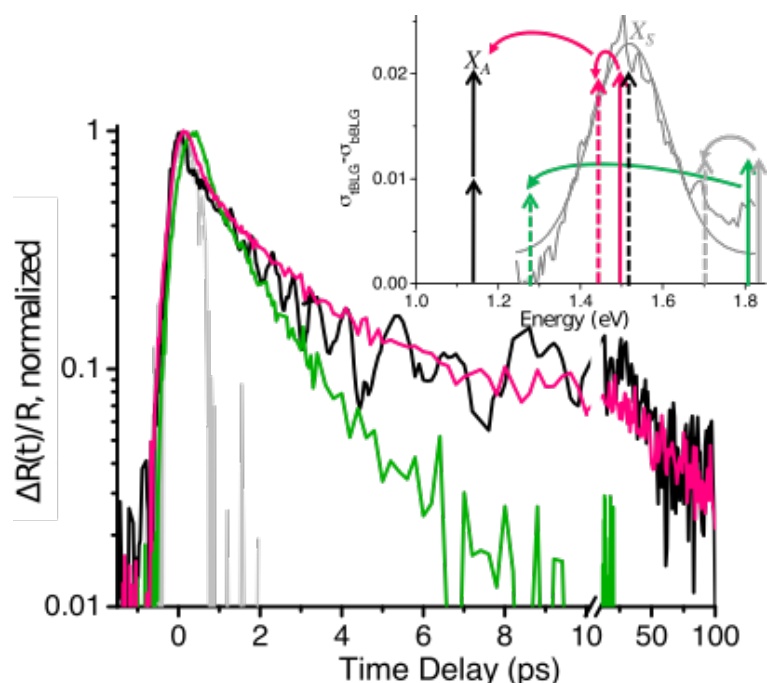


Figure 4.4: Resonant vs. non-resonant electronic relaxation for 8° tBLG. The vertical pump (solid arrows) and probe (dashed arrows) combinations labeled on the absorption spectrum (inset) of 8° tBLG, correspond by colour to the normalized 1-or 2-ph. relaxation kinetics plotted.

Next, we compare the 1-ph X_S (pink) vs. 2-ph X_A (black) electron relaxation kinetics measured for 8° tBLG in Figure 4.4. We find that the normalized TA relaxation kinetics for one-photon and two-photon resonant excitations are nearly identical. These matching kinetics indicate that both signals originate from the same depleted common ground state, and that the electrons are impulsively transferred from the bright (X_S) to the dark (X_A) state as illustrated in Figure 4.4ai. Such fast kinetic $X_S \rightarrow X_A$ relaxation is consistent with theory showing that X_S is an unstable exciton state.¹⁵³ As a control, in Figure 4.4 (gray) we show that the relaxation kinetics are impulsive when both E_{pump} and $E_{\text{pr}} > E_\theta$, indicating that only free electron states are probed above resonance. Lastly, we consider the case of $E_{\text{pr}} < E_\theta < E_{\text{pump}}$, and find the long-decay components are consistently absent, suggesting resonant optical excitation may be required to form a long-lived stable exciton. Nonetheless, the off-resonance tBLG kinetic relaxation (green) is still significantly enhanced in amplitude and lifetime compared to the bBLG TA response (Figure 4.2c). This suggests that an electronic relaxation bottleneck effect is still present even when tBLG is optically excited above resonance.

4.7 Summary

By definitively isolating the interlayer electronic dynamics of 1- and 2-ph resonant optical transitions in tBLG, we have uncovered a fine-structure of bound (X_A) and unbound (X_S , $X_S + \Delta$) exciton states that agrees well with recent simulations.¹⁵³ Specifically, we employed a novel form of diffraction-limited TA microscopy to obtain the intrinsic spectra and dynamics of single tBLG domains under a variety of resonant and non-resonant pump/probe combinations. In Figure 4.2b, we show a TA-movie of

electronic population that reveals the striking contrast between the bound-exciton carriers in the tBLG region and the free-electron population in the surrounding graphene. These results suggest that the photoexcited tBLG interlayer electrons are initially decoupled from scattering into graphene continuum states, and experience a significant electron relaxation bottleneck. In particular, resonantly excited carriers in tBLG give much stronger TA amplitude with longer relaxation kinetics for both the short (~ 2 ps) and long relaxation timescales (~ 70 ps). This bottleneck is best explained by the existence of strongly-bound excitons in a ‘ghost Fano’ state that we explicitly resolve using 2-ph TA microscopy.¹⁵³ Our results imply that tBLG may be a unique hybrid electronic material where free-electron metallic character can coexist alongside stable exciton states. The work further opens up possible new avenues for carrier extraction that combine the high conductivity of metallic intralayer-electrons, with the enhanced electronic population that is now established for the interlayer electrons in tBLG.

4.8 Methods

Multi-layer graphene was grown using low pressure CVD method on copper foil and transferred to silicon nitride grids (see Chapter 1).¹⁷⁶ Areas containing low-angle tBLG were first identified using, a combination of hyperspectral absorption imaging technique, and dark field TEM (DF-TEM).³⁸ Final twist angle assignments of the bilayer patches were made by correlating the linear absorption and 1-ph TA peak spectral peaks energies (see Chapter 2).⁴⁶

tBLG bright (X_S) and dark (X_A) states and their corresponding electronic dynamics were measured using 1-and 2-ph confocal scanning TA microscopy.¹⁷⁷ Collinear pump-and probe pulses were obtained from two independently tunable outputs

of an ultrafast system composed of Ti:saph oscillator (Coherent Chameleon Ultra II, 80 MHz, wavelength range 680-1080 nm) pumping an optical parametric oscillator (APE-Compact, wavelength range 1000-4000 nm). For one-photon TA measurements requiring pump and probe pulse doubly resonant with the bright (X_S) transition, a white-light supercontinuum probe was instead used. Cross-correlation of the pump and probe after the objective yielded a FWHM pulse duration of 142 fs.

After a mechanical delay stage, both the pump, and the probe beams were aligned in a collinear geometry, raster-scanned by piezo-scanning mirror and coupled into a confocal scanning microscope via a 50X IR-region enhanced, achromatic objective (NA=0.65). One and two photon transient absorption signals were detected by measuring the probe beam on with a TE cooled InGaAs detector connected to a Zurich HF2LI lock-in amplifier. The pump beam was modulated at either 0.25 or 1 MHz using a AO-modulator (Gooch & Housego) to enable high-frequency lock-in detection of the differential reflectivity. Appropriate optical filters were used in front of the detector to block the pump beam. The pump and probe spot sizes on the sample were determined to $\sim 1.5 \mu\text{m}$, by fitting to a confocal scanning reflection profile of deposited gold pads. The fluence of the probe power was 5% of the pump fluence. Except where specified, all the measurements were done at 295 K. The probe power was fixed at ($\sim 1 \times 10^{12}$ photons/cm²) for the pump power dependence measurements. Microscope objective/transmission corrections curves were measured and rigorously taken into account for all the wavelengths, after each measurement.

4.9 Supporting Information

A) The *intralayer* transient optical conductivity (i.e. single-layer graphene TA)

In transient absorption microscopy, we measure the change in the amplitude of the reflected probe-beam at a probe energy E_0 , in the absence (R_2) and presence (R_1) of a pump beam. Under optical excitation conditions, transient reflectivity is related to the optical conductivity by^{157,178}:

$$\frac{\Delta R(t, E_0)}{R} = \frac{R_2 - R_1}{R_1} = \frac{4}{n_s^2 - 1} \frac{4\pi}{c} \sum_i \text{Re}[\sigma_i(E_0, T_e(t)) - \sigma_i(E_0, T_1)]$$

Both interband and intraband processes contribute to the total optical conductivity

$$\sigma_{\text{TOT}} = \sigma_{\text{inter}} + \sigma_{\text{intra}}$$

When the Fermi populations are evaluated (to first order) it has been shown that^{46,179}:

$$\frac{\Delta R(t)_{\text{inter}}}{R} \propto \tanh\left(\frac{E_0 \pm E_F}{2k_B T_e(t)}\right) - \tanh\left(\frac{E_0 \pm E_F}{2k_B T_1}\right) \dots\dots\dots(4.1)$$

$$\frac{\Delta R(t)_{\text{intra}}}{R} \propto \frac{\Gamma k_B T_e(t)}{(E_0 \pm E_F)^2 + \Gamma^2} - \frac{\Gamma k_B T_1}{(E_0 \pm E_F)^2 + \Gamma^2} \dots\dots\dots(4.2)$$

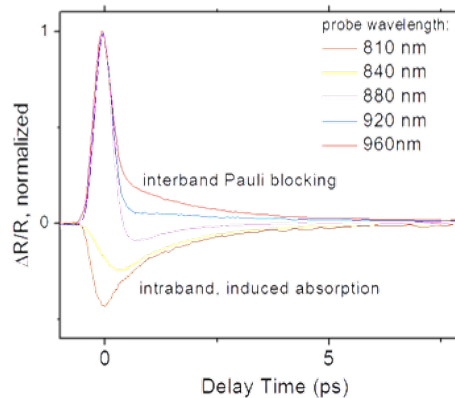


Figure 4.5: At a fixed pump carrier density, we measured the pump-probe response of a CVD graphene over probe energies where the intraband response contributes.

The absolute sign of the intraband and interband transient signals are opposite, permitting experimental separation.¹⁷⁹ Sign conventions used in this Chapter are opposite to the ones used in Chapter 2. As an example, we are assigning the bleach response a positive sign and ESA a negative sign. We attribute the bleach to the transient interband optical conductivity, and the excited state absorption (ESA) to intraband transitions as discussed in Chapter 2.

As observed in previous works¹⁷⁹ we observed that intraband contribution is best determined by its absolute sign (under the specific sample and carrier densities used in our experiment). For probe energies < 1.3 eV, we have shown in Figure 4.5 the relative intraband kinetic contribution is weak, and can be approximately ignored. When probe energies are > 1.3 eV, we can remove this contribution for the TA kinetics by plotting, $\Delta\sigma_{\text{tBLG}}(t) - \Delta\sigma_{\text{bBLG}}(t)$, approximately leaving just the transient optical conductivity of the interlayer electrons. A similar approach ($\sigma_{\text{tBLG}} - \sigma_{\text{bBLG}}$) has been recently used to analyze the properties of linear absorption microscopy.³⁸

B) The *interlayer* transient optical conductivity

Currently, there exists no closed-form expression for the transient optical conductivity near the tBLG optical absorption resonance. In the limit that the two layers of graphene are electronically decoupled, the transient optical conductivity, $\Delta\sigma(t)$ is obtained by evaluating the Fermi-Dirac electronic population at the desired energy (see A). In the opposite regime, the layers of tBLG could be strongly coupled and form bound exciton states. These resultant strongly correlated electron-hole pairs are predicted

to be initially decoupled from the exciton states below, and have a well-defined, common exciton ground state.

Generally, the relative magnitude of a pump-probe or transient absorption (TA) response is given by, $\Delta\sigma(t, E_{pr}) \propto n(t)[\sigma_{ESA}(E_{pr}) - \sigma_{SE}(E_{pr}) - \sigma_0(E_{pr})]$; where $n(t)$ is the electronic carrier population occupying the probed state energy (E_{pr}), σ_{ESA} , σ_{SE} and σ_0 are the absorption cross-sections of the excited state absorption (ESA), stimulated emission (SE) and the ground state spectral bleach at an incident probe energy, E_{pr} . The ESAs (e.g. intraband absorption in graphene) gives the opposite (negative) $\Delta\sigma(t)$ sign, while the “ground state bleach” response is positive signed, arising from interband Pauli blocking effects.

In the free carrier model, Pauli blocking is referred to the photo excited holes or electrons lying at the same energy of the probe beam, leading to decreased absorption (positive signal by our convention). In the bound exciton model, Pauli blocking chiefly refers to decreased probe beam absorption from a depleted ground exciton band. Excitons tend to inherently have very narrow electronic distribution in their center of mass momentum space, $K_{cm} = (k_e + k_h)/2$, enabling us to approximately treat the ground and excited states as a discrete energy broadened by static and dynamic environmental interactions. In such a bound-exciton model, from the carrier density in the above equation can be found that $\Delta\sigma(t)$ decays approximately exponentially in time, according to the rate equation: $\frac{dn}{dt} = P\delta(t) - \frac{n}{\tau}$; where, P is the incident photon flux, $\delta(t)$ approximates our 140 fs excitation pulses, and τ is the exciton relaxation lifetime of the

X_A state. If there are multiple states (e.g. X_A and X_S) or multiple relaxation pathways there will be multiple lifetimes τ_1 and τ_2 in the rate law.

C) Bernal stacked graphene vs. off-resonant tBLG electronic dynamics

This research concerns the interlayer electronic properties of resonantly excited tBLG. However at most twist angles, light will photoexcite electrons below the tBLG resonance. The data in Figure 4.6 give interband transient bleach signals, which was acquired at a 1.25 eV pump and 0.95 eV probe. In Figure 4.3c, we compare against single layer graphene (black), and show that, the tBLG amplitude (green) is twice as large and the electronic dynamics are virtually indistinguishable. Consequently, we conclude that presence of high energy resonance states, do not appreciably change the electronic dynamics of low lying states; as expected.

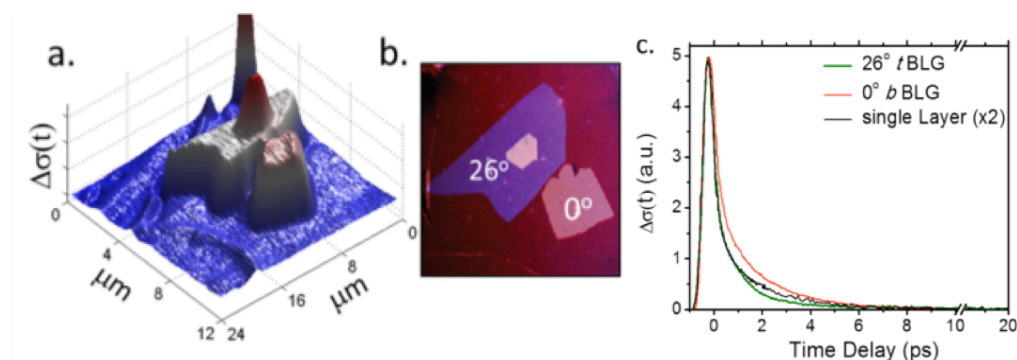


Figure 4.6: Bernal vs. twisted, off-resonance. (a) Transient absorption microscopy map at $t=200$ fs shows relative electron populations in 1, 2 and 3 layer graphene. (b) Corresponding darkfield TEM map, (c) 0° stacked graphene has marginally slower electron cooling rate than single-layer or twisted bilayer when pumped and probed far below resonance.

Interesting, we find the Bernal stacked graphene has systematically longer dynamics than single layer graphene in other two configuration presented. This suggests

that subtle band bending associated with *b*BLG, may serve to (*marginally*) slow the overall relaxation rate of the Fermi-Dirac distribution. Previous bilayer graphene TA studies did not have access to twist angle information, so precise comparison of the dynamic response under identical excitation condition were not possible. This work focuses on the electronic bottleneck behavior of resonantly excited tBLG electronic carriers, and the subtle below resonance excitation behaviors are not discussed in depth here.

D) Resonant vs. non-resonant TA maps

To further confirm the bottleneck behavior, Figure 4.7 shows scanning TA microscopy maps of graphene for resonant (a), and non-resonant excitation (b, and c). Enhanced TA Pauli blocking response (positive signed) is observed from $\sim 6^\circ$ tBLG domain ((a) green arrow) for resonant pump (1.33 eV), and probe (1.23 eV) excitation, however, the surrounding graphene gives opposite signed, intraband response. On the other hand, when the electron population is probed above (Figure 4.7 (b)), or below

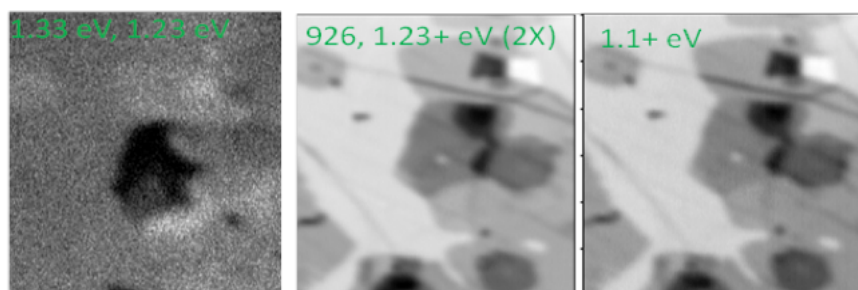


Figure 4.7: Resonant vs. non-resonant TA microscopy map: scanning TA map of graphene. (a) Resonant excitation. (b), and (c) Non-resonant excitation.

(Figure 4.7c) the resonance, the relative electron population localized to the $\sim 6^\circ$ tBLG domain decreases, which is consistent with the TA relaxation dynamics discussed earlier

(Figure 4.2). These observations suggest that when interlayer electrons are excited at resonance (E_0), the tBLG carriers are decoupled from the lower lying continuum states, creating stable exciton states, suggesting that the resonant excitation conditions may be necessary for the bound exciton state formation.

E) Lattice Temperature Dependence

TA can also contain transient behavior that results from thermal induced shifts to absorption peaks. In tBLG however, these temperature induced absorption shifts appear to be very weak compared to the strong electronic response observed. In Figure 4.8a-b, we measured the linear absorption of tBLG at 295K and 5K and show that there is no detectable shift within our noise limit.

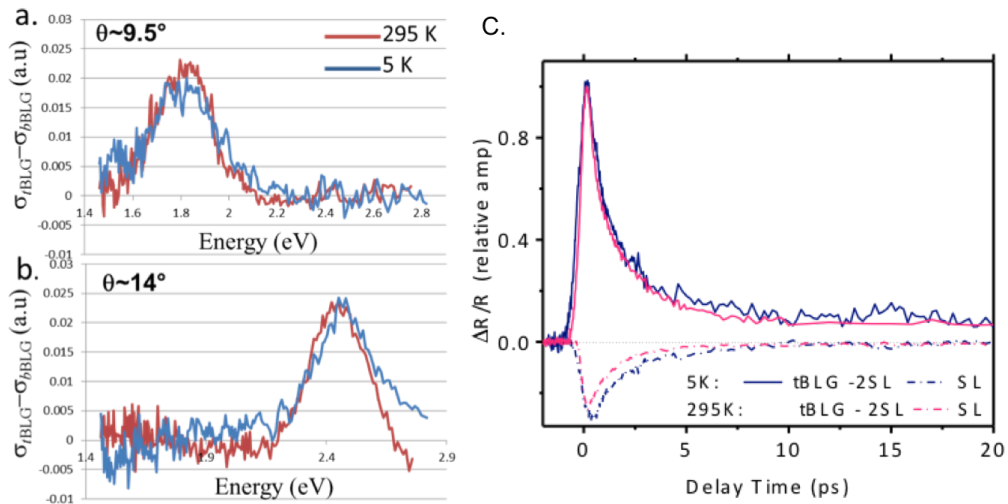


Figure 4.8: 295 K and 5 K linear absorption spectra for (a) 9.5° and (b) 14° tBLG. (c) Lattice temperature leaves the twisted bilayer relaxation kinetics unaltered. 1.33 eV pump, 1.26 eV probe for 6.8° oriented tBLG. The single layer (SL) component is subtracted.

Likewise, in Figure 4.8c we show transient absorption measurement at 295 K (pink) and 5 K (navy) and find that the interlayer relaxation dynamics are also roughly

lattice temperature insensitive. Specifically, since the 5 K (navy curve) experienced a much larger laser induced lattice temperature change, we would expect a much large amplitude contribution at low temperatures, if the long component was thermally induced. However we instead observe that the interlayer dynamics are identical to the 295 K case.

We conclude that since thermal induced absorption shifts cannot be observed over a $\sim 300\text{K}$ lattice temperature ramp, the tBLG TA absorption components we report in this work is likely not thermal in nature. The dynamics are also roughly insensitive to photon flux, as further discussed in (G), and no TA sign-flips were observed when the blue tBLG spectral edge is probed instead of the red edge.

F) Substrate Dependence

We also measured the linear, and TA response of tBLG on silicon, silicon, nitride, and fused silica substrate, and both the linear, and TA response was similar.

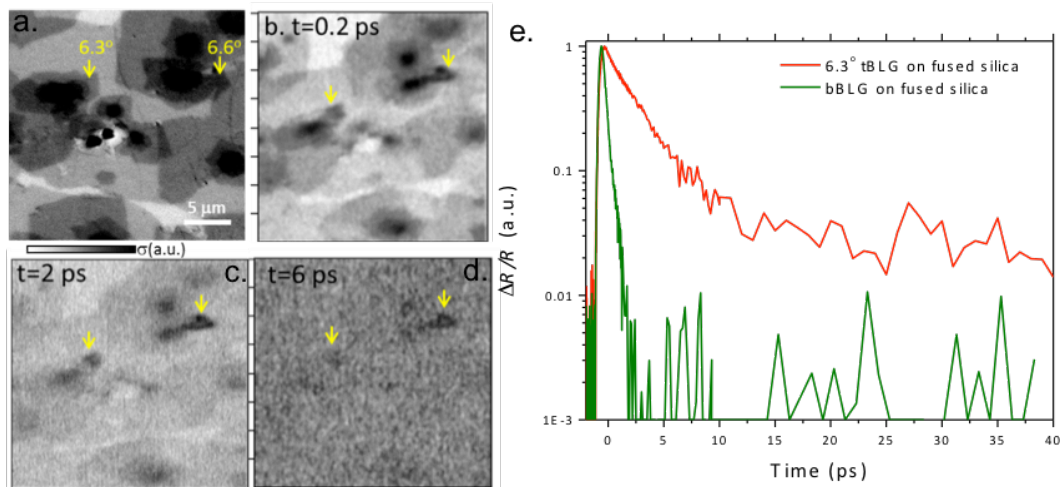


Figure 4.9: a-d. One-photon on-resonance TA movie frames on a fused silica substrate. For resonant pump, and probe combination ($E_{\text{pump}} \sim E_{\text{probe}} \sim E_\theta$), positive signed, TA Pauli blocking response (ground state depletion) is enhanced for the 6.3° , and 6.6° tBLG domains (yellow arrows). e. One photon TA relaxation kinetics: TA electron relaxation

dynamics of 6.3° tBLG domain (red), and bBLG (green) labeled on a fused silica substrate.

Figure 4.9a-d shows one-photon scanning TA movie frames of tBLG domains on a fused silica. The strong, enhanced interband (Pauli blocking) TA signal is localized to the 6.3° , and 6.6° tBLG domains (yellow arrows).

The excited carriers in 6.3° , and 6.6° tBLG domains stay excited even at 6 ps after the initial excitation, whereas the excited carriers in the surrounding graphene decay away. Figure 4.9e shows one-photon long-lived, TA relaxation kinetics of 6.3° tBLG domain (red), and opposite signed, short-lived, TA relaxation kinetics of bBLG on a fused silica. The relaxation kinetics, and the decay lifetime are similar to that of the tBLG, and bBLG domains on SiN substrate reported in the Figure 4.2c, confirming that the interlayer electronic response is invariant to the substrate, and it is electronic in nature.

G) One and Two-Photon Dynamics and Maps

Figure 4.10a shows normalized relaxation kinetics of 7.5° , 6.8° , 8° , and 5.1° tBLG domains for resonant excitation. Both one-, and two-photon on, and off resonance TA were performed on various tBLG domains with angles ranging from 5° to 10° . The long-lived components were consistently present for both one-, and two-photon resonant excitations. The measured long-lived, strong, positive signed, Pauli blocking response of various tBLG domains suggests that the resonant excited interlayer electrons experience electronic relaxation bottleneck as discussed in the earlier sections (Figure 2c), in contrast to short lived, weak, negative signed, intraband response from bBLG.

Figure 4.10b shows relative electron population in 6.5° , and 8° tBLG domains for fixed probe energy of 1.40 eV, and two-photon pump energy 1.04 eV (blue), 1.16 eV (black), and 1.31 eV (green) labeled. The strong two-photon positive signed signal from

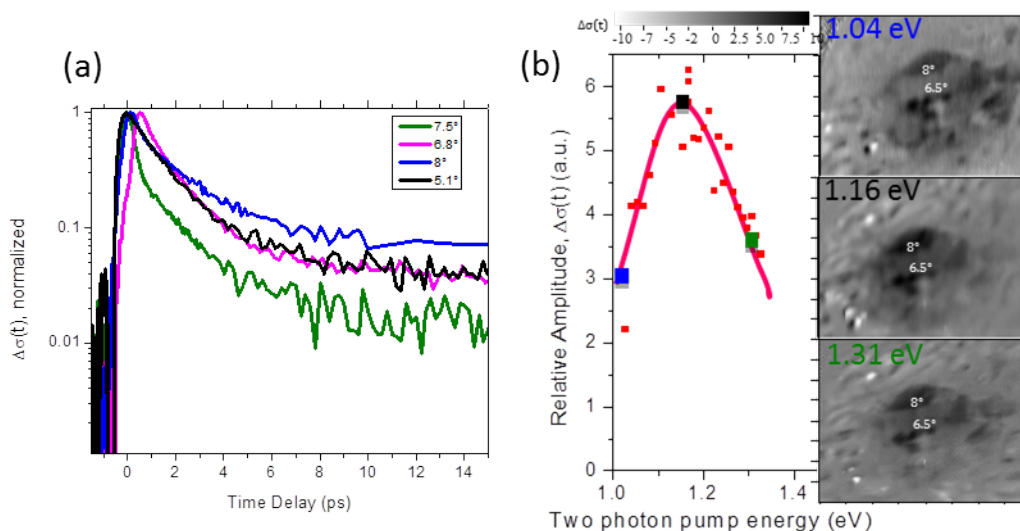


Figure 4.10: (a) For resonant pump, and probe combinations, long-decay components are consistently present for various tBLG domains. (b) Two-photon transient absorption maps for a fixed probe energy (1.40 eV), and pump energy 1.04 eV, 1.16 eV, and 1.31 eV.

8° tBLG domains corresponds to the TA Pauli blocking response (electronic bleach), and the weak, two-photon negative signed signal from 6.5° tBLG domains corresponds to the intra-band response as discussed in the manuscript. The amplitude of the TA Pauli blocking response from 8° tBLG domains is relatively weak as we tune the two-photon pump energy slightly below ((a) 1.04 eV, blue), or above ((c) 1.31 eV, green) the two-photon resonance ((a), 1.6 eV, black). This observation is consistent with the electron kinetics reported in the Figure 4.4. Our observations suggest that the electron population stay excited for longer if excited at two-photon resonance, which again suggests that the resonant excitations may be important for formation of stable, bound exciton state.

H) One and two-photon flux dependence

Figure 4.11 suggests that Auger annihilation contributes strongly to the TA power dependence of tBLG. Auger exciton annihilation effects are commonly including the electron dynamics of strongly-bound excitonic systems such as (SWCNTs), with the

following characteristic kinetics: $\frac{dn}{dt} = P\delta(t) - \frac{n}{\tau} - \frac{\gamma n^2}{2}$

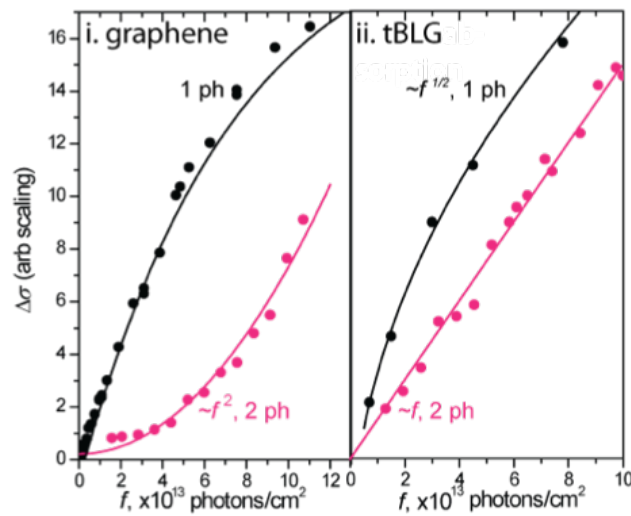


Figure 4.11: Transient absorption signal vs. photon flux, f . *i.* Graphene, showing Fermi-Dirac and quadratic fits, *ii.* tBLG TA, showing square root function and linear fits for 1-photon, and 2-photon excitation respectively.

Here, P is the incident photon flux, $\delta(t)$ approximates our 140 fs excitation pulses, τ is the exciton relaxation lifetime of the X_A state, and γ the exciton annihilation rate constant. In the short-time limit, when exciton density is high annihilation is the dominant term, the above equation may be approximated by, $n_0 = \sqrt{\frac{2P}{\gamma}}$. This suggests, that if the tBLG TA signal comes for bound exciton states, the TA amplitude may scale with the square root of photon flux for a one-photon excitation, and linearly for two-

photon excitation. Accordingly, for tBLG, we observe in Figure 4.11*ii* a characteristic square root amplitude dependence that is seen in analogous systems like the SWCNTs. Consistent with dominant exciton annihilation, we find the two-photon tBLG response grows only linearly with photon flux.

As a control, we also show in Figure 4.11*i*, the graphene interband TA power dependence fit to graphene's characteristic Fermi-Dirac electronic filling function. Conversely, the two-photon TA fits to a quadratic function for delay times near $t=0$, as required. We conclude that underlying square root behaviors observed suggest Auger annihilation processes in tBLG. This is further in agreement with a bound excitonic model, and suggests further parallels between tBLG and s-SWCNTs, motivating future investigations.

5. PHOTOLUMINESCENCE FROM STRONGLY-BOUND INTERLAYER EXCITONS IN TWISTED BILAYER GRAPHENE

Hiral Patel, Lujie Huang, Cheol-Joo Kim, Jiwoong Park, and Matt W. Graham

OSA Technical Digest, doi:10.1364/CLEO-QELS-2017-FTh1F.5

And

In Preparation, 2017

We observe resonant photoemission from graphene with emission energies that tune with the stacking angle of both CVD-grown and artificially-stacked twisted bilayer graphene (tBLG). This signal is best assigned to photoluminescence from strongly-bound interlayer exciton states transitions whose energy tunes monotonically with twist-angle. Photoluminescence from the tBLG domain is only observed if the optical excitation creates bound interlayer excitons by resonant excitation. In contrast, optical excitation of the metallic continuum-states only produces broad, hot-carrier photoemission and fast dynamics that are largely indistinguishable from the monolayer graphene response. Such unusually stable interlayer exciton states in a system that is otherwise metallic result from the effective rehybridization of two established degenerate van-Hove singularity-like transitions to create an optically-dark exciton state that is dynamically-stabilized by vanishing electronic continuum coupling. In support this interlayer exciton theory, our applied methods of intraband transient absorption microscopy and two-photon photoluminescence excitation spectra of bright and dark transitions map out the exciton fine-structure and long-lived dynamics. Both of our measurements independently quantify the exciton binding energies that range from 0.4-0.7 eV. Our results suggest that resonantly excited tBLG has a novel metallic-semiconductor hybrid physics that results from bound interlayer excitons that can coexist alongside the graphene continuum states.

5.1 Introduction

This Chapter is largely adapted from H. Patel *et al.*, “A fine structure of strongly-bound interlayer exciton states in twisted bilayer graphene”, OSA Technical digest, doi: 10.1364/CLEO_QELS.2017.FTh1F.5 and H. Patel *et al.*, “Photoluminescence from strongly-bound interlayer excitons in twisted bilayer graphene”, in preparation. Here, we discuss photoluminescence emission from interlayer exciton states of twisted bilayer graphene and map out the exciton binding energy with intraband transient absorption microscopy for the first time.

The rotation angle between two layers with respect to each other provides an extra degree of freedom to drastically alter electronic and optical properties of van der Waals 2D materials. As such, a system twisted bilayer graphene (tBLG) is created upon rotating two stacked layers of graphene at an off-axis angle. It has proven to be of particular interest due to modified unique electronic characteristics that were unthought-of. Earlier studies of tBLG with scanning tunneling spectroscopy, optical absorption, and Raman spectroscopy provided evidence of angle dependent electronic and optical properties such as van Hove singularities in the low energy electronic density of states^{125,129,164}, tunable optical absorption resonances^{14,38,46,47,80,81,152}, and tunable Raman G band enhancement^{80,81,180}. Recent theoretical and experimental studies on tBLG predicted and measured electronic relaxation bottleneck resulting in long lifetimes due to the presence of strongly-bound excitons in metallic tBLG due to “ghost” Fano resonance effect.^{153,181}

However, to date, all optical investigations on tBLG have been limited to optical absorption, Raman, and recently transient absorption (TA). Nevertheless, no light

emission from tBLG has been reported. The absence of emission can be understood due to lack of a band gap. Recent theoretical and experimental studies predicted and measured evidence of strongly-bound excitons in a metallic tBLG due to “ghost” Fano resonance effect.¹⁵³ The long-lived dynamics shed light on the possible slow process of light emission since relaxation through e-e, and e-ph interactions is slower than expected before.

5.2 Photoluminescence from tBLG -2-ph PL Microscopy

In this work, we report the first observation of tunable photoluminescence (PL) in tBLG upon femtosecond laser excitation. The observed emission is at higher energy than the excitation energy, and its emission energy changes with the angle between the two graphene sheets. The pump power dependence of the PL is linear suggesting annihilation processes similar to other excitonic systems such as transition metal dichalcogenides (TMDs) and carbon nanotubes (CNTs)¹⁸²⁻¹⁸⁷. Although tBLG is a semimetal, owing to its unique band symmetry, bound excitons are formed with the binding energy on the order of ~ 0.7 eV which is responsible for long-lived dynamics.^{153,181} As a consequence, the relatively slow process of light emission is possible because excited carriers fully relax through slower e-e and e-ph interactions. Our analysis further suggests that PL from tBLG arises when exciting dark state resonantly with 2-photons, populating the long lived dark state which then thermally populates the bright state for photoemission.

Our experiments were performed with a 80 MHz Ti:sapphire oscillator pumping an optical parametric oscillator with the energy range of 0.31 eV-1.82 eV with 140 fs pulse duration. The schematic of our experiments is outlined in Figure 5.1ai. For the PL

experiment, the beam is coupled to a microscope and focused onto the sample with an objective, and the confocal scanning mirrors were used to raster scan the beam over the sample to acquire large area illumination. The PL was collected in the backscattered direction, and the spatial PL maps were acquired with a cooled EMCCD camera using appropriate optical filters in front of the camera to block the excitation energy. The PL excitation spectrum was acquired by scanning the excitation energy. All the measurements were performed in either atmosphere or nitrogen purge environment at room temperature unless specified.

tBLG was obtained with as grown CVD method or artificially transferred CVD grown single layer material. For artificially transferred tBLG, graphene was grown with an aligned CVD growth method on a copper substrate^{24,176}. The copper foil with graphene is then cut into two pieces and then is transferred in a tBLG configuration to a SiN or fused silica substrate with the artificially transferred process discussed in Chapter 2. This method can result in a large domain tBLG material.¹⁸⁸ The samples were characterized using the combination of hyperspectral absorption, transient absorption, and dark field TEM^{38,152,181} to locate twisted domains. The final angle assignment of the domains was done using a well-established method looking at linear absorption peak energies.⁴⁶

Low energy electronic band structure of tBLG in Figure 5.1a ii shows an opening of avoided crossing regions upon stacking and rotating two layers of graphene. Near avoided crossing regions, we get degenerate optical transitions which give rise to interlayer van Hove singularities (vHs) that are tunable with the stacking angle θ . Figure 5.1c shows a snapshot of an optical hyperspectral absorption image of an artificially transferred tBLG sample on SiN that has different domains (highlighted) with twist

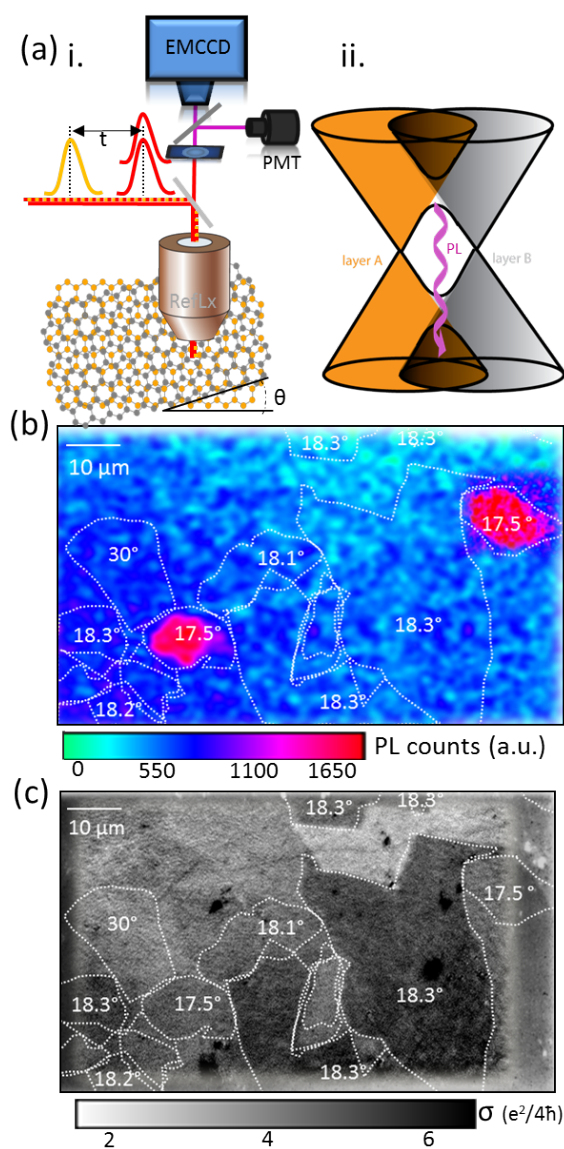


Figure 5.1: Two-photon photoluminescence. (a) i. Ultrafast 2-photon photoluminescence microscopy experiment, ii. tBLG bandstructure. (b) Spatial 2-ph PL map of tBLG domains showing enhanced photo emission localized in 17.5° domains upon 2-ph resonant excitation of the dark state (X_A state) of 17.5° domains. (c) Linear absorption map showing various tBLG domains.

angles 16.9° - 30° . For the first time, upon near-IR femtosecond laser excitation, a weak photoluminescence response was detected at a higher energy than the incident photons. Surprisingly, for a given excitation energy, only two domains (17.5°) emit PL whereas the surrounding domains are off resonant as shown in Figure 5.1b. Upon exciting with 1.2 eV, the emission energy of ~ 2.8 eV corresponds to the absorption resonance of the 17.5° domains. The spatial PL map is shown in Figure 5.1b with ~ 1.24 eV excitation energy; two 17.5° domains show localized enhanced photo emission whereas surrounding domains are off-resonant.

The observed photoluminescence from tBLG has different characteristics compared to what is known for graphene.¹⁸⁹⁻¹⁹¹ In pristine graphene, a broadband nonlinear PL was reported across the visible range (1.7-3.5 eV) with higher emission energy than the excitation energy that is different from the conventional or 2-ph PL.^{189,190} The emission is best explained by the excited electrons thermalizing by optical phonons producing carriers with transient temperatures more than 3000 K. Recently, excitonic photoluminescence from graphene on a copper substrate was reported with sharp emission lines at ~ 3.16 eV with 4.7 eV ultrafast laser excitation. This emission is due to the hybridization of π -orbitals of graphene and d-orbitals of Cu creating large optical transition probability (vHs) shifting the saddle point M of graphene. The vHs results in a strong electron-phonon coupling upon laser irradiation leading to photoluminescence.¹⁹¹

5.3 tBLG Photoluminescence Mechanism

PL and bound excitons are generally not expected in a metallic material like tBLG or metallic CNTs as a result of extensive screening effects. However, in a 1D metallic

CNTs, due to low screening and strong quantum confinement of electron and hole, bound exciton with a binding energy of the order of 50 meV were predicted and observed.^{192,193}

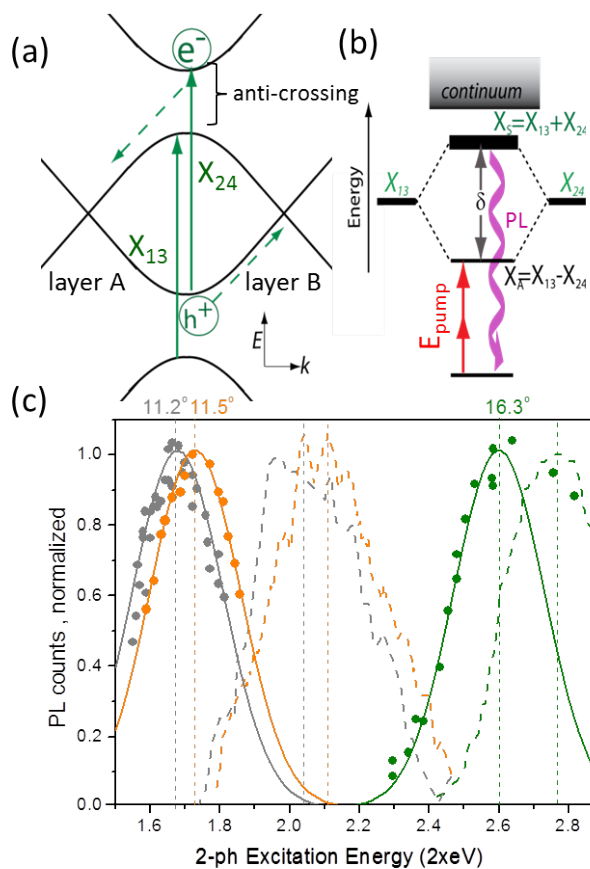


Figure 5.2: Tunable photoluminescence. (a) Electronic bandstructure cross-sectional view showing tunable, degenerate interlayer optical transitions X_{13} and X_{24} . (b) In the rehybridized model, they split into symmetric, bright (X_S) and antisymmetric, dark (X_A) exciton states. Energy diagram of the bound exciton model outlines the emission process from the X_S state upon two-photon excitation of the X_A state. (c) 2-ph PL excitation spectrum showing tunable PL (solid lines) with the absorption resonance (dashed lines). Dark and bright state splitting, $\delta \sim 0.15$ eV for 16.3° domain (green), and $\delta \sim 0.38$ eV for 11.2° (gray) and 11.5° (orange) domain.

Owing to bound excitons, and the presence of dark states, low PL quantum yield was reported for metallic CNTs.¹⁹³ We now examine the possible mechanism in detail that is responsible for the tunable PL in tBLG. Figure 5.2a shows the alignment of bands when two graphene sheets are stacked at off axis angle. Two Dirac cones are formed from each graphene sheets and owing to the hybridized orbitals; bands create avoided crossing regions producing optical transitions X_{13} and X_{24} .^{166,167} These transitions are degenerate in energy and momentum in the k-space. Previous studies show that there is $\sim 20\%$ enhancement in the oscillator strength, and the absorption peak energy is tunable with the angle between two graphene sheets.^{38,46,125,129,152,164} These transitions were traditionally interpreted as van Hove singularities.^{125,152} Alternatively, upon resonant excitation of the degenerate transitions, X_{13} and X_{24} , they rehybridize to form a bonding and an anti-bonding state. This rehybridized picture is shown in Figure 5.2b. X_{13} and X_{24} are Fano resonant states, which means they are coupled to the lower lying continuum states. Upon constructive coherence between X_{13} and X_{24} , a higher energy state X_s is formed which is still coupled to the lower lying continuum states due to the combination of the two Fano states. On the other hand, upon deconstructive coherence between the states X_{13} and X_{24} , a lower energy state X_A is formed which cancels the lower lying continuum contribution.^{153,181} Owing to this dark state, the formation of bound excitons and long-lived dynamics were predicted theoretically by Liang et al.¹⁸¹ and experimentally observed by Patel et al.¹⁵³ In particular, we have a model where carriers are excited by bright multiple transitions, and they relax impulsively to the bound exciton state or dark state where they can relax at a slower rate due to this ‘ghost’ Fano effect which cancels the electron-continuum coupling. Although, the mechanism of bound exciton formation

in a 2D metallic tBLG is due to unique band symmetry and rehybridization of Fano resonance states unlike low screening in metallic CNTs, photo-emission is possible.

5.4 Photoluminescence Excitation Spectrum and Spatial Maps

Upon tuning the excitation energy to the red edge and using combinations of different optical filters in front of the EMCCD camera for PL detection, we observed light emission from several other tBLG domains. The PL excitation spectrum (solid lines) in Figure 5.2c shows enhanced light emission peaks located at different energies, ~ 2.61 eV, ~ 1.73 eV, and ~ 1.67 eV for 16.3° , 11.5° and 11.2° domain respectively, suggesting tunable nature of the PL emission with the tBLG domain angle. The absorption spectrum (dashed lines) of the measured domains is shown in green for the 16.3° domain, orange for the 11.5° domain and gray for the 11.2° domain. This gives the splitting energy between the absorption resonance peak energy and the emission peak energy ~ 0.15 eV for the 16.3° domain, ~ 0.38 eV for 11.2° and 11.5° . The observed enhanced emission could correspond to the two-photon Raman response from tBLG, since one-photon Raman enhancement is well documented in graphene. However, for Raman enhancement in graphene, the red-shifted (Stokes) and blue-shifted (anti-Stokes) components are known to have the splitting energy of ~ 0.2 eV for both Stokes and anti-Stokes response.^{162,194,195} Our splitting energy of ~ 0.15 eV for the 16.3° and ~ 0.38 eV for 11.2° and 11.5° domains for possible Stokes shift instead of 0.2 eV rules out the possibility of Raman enhancement effect.

To further verify PL and to explain the mechanism of the photoemission, we tune our excitation energy to the blue edge to map out the PL excitation spectrum

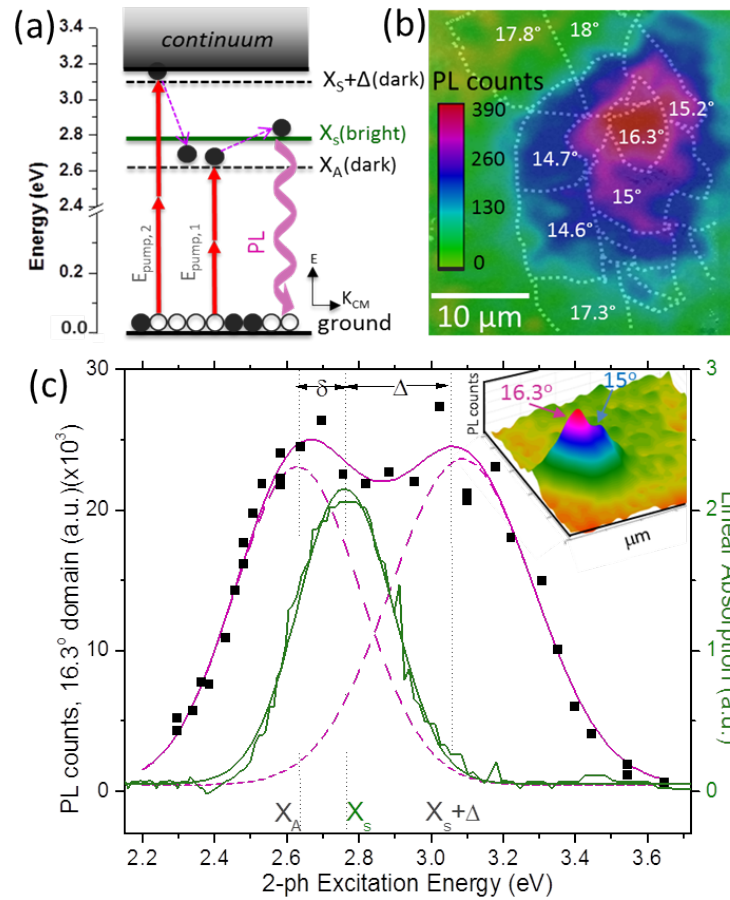


Figure 5.3: 2-photon emission. (a) Energy diagram of the bound exciton model outlines the emission process from the X_S state upon two-photon excitation of the X_A state. (b) Spatial two-photon PL map of tBLG domains shows enhanced photo emission from 16.3° and 15° domains for 2-ph resonant excitation of the X_A state. (c) 2-ph PL excitation spectrum (black) shows a bimodal distribution with two peaks centered at 2.6 eV, and 3.1 eV around the 1-ph linear absorption (green). (inset). 3D PL map of the 16.3° domain piece measured.

(Figure 5.3c). Spatial PL map of tBLG domains in Figure 5.3b show enhanced photoemission response that is localized to the 16.3° domain whereas the surrounding domains are off resonant. In Figure 5.3c, the PL excitation spectrum (magenta) for a 16.3° domain shows a bimodal distribution with two peaks located at ~ 2.61 eV and ~ 3.1 eV

around absorption resonance at ~ 2.76 eV (green). Inset in Figure 5.3c shows a 3D PL map for the measured piece in Figure 5.3b. We get the splitting energy of ~ 0.34 eV between the absorption resonance and the higher energy PL emission further ruling out the Raman enhancement possibility. Besides, the Stokes components are known to have a higher intensity than the anti-Stokes response as seen in other materials such as graphene and single walled CNTs (SWCNTs)^{189,195}.

Further, Stokes and anti-Stokes response are known to be symmetric around the absorption as reported by Souza et al., and Liu et al.^{189,195} Our results suggest that the enhanced response resembles the photoluminescence and rules out the possible two-photon Raman response as evidenced by, (i) splitting energy between absorption resonance and the emission peaks with lower energy peak ~ 0.38 eV for 11.2° and 11.5° domains (Figure 5.2c), ~ 0.15 eV for 16.3° domain and higher energy peak ~ 0.34 eV for 16.3° domain and not 0.2 eV for both Stokes and anti-Stokes responses as expected for a graphene like system (Figure 5.3b). (ii) Enhanced emission response at lower and higher energy is not symmetric around absorption resonance (Figure 5.3b). (iii) Lower and higher lying enhanced emission peaks have similar intensity.

We can explain the detected PL origin in tBLG with the bound exciton model proposed by Patel et al., and Liang et al.^{153,181} shown in Figure 5.3a. In this model, we have an optically dark state one above and one below the absorption resonance. With the two-photon fs laser excitation of tBLG, we can access these dark states. Upon 2-photon excitation of the higher lying dark state $E_{\text{pump}2}$ in Figure 5.3a, the charge carriers impulsively relax to the lower lying dark state X_A . Since the dark state X_A is a long-lived exciton state¹⁸¹, upon 2-ph excitation $E_{\text{pump}1}$ and $E_{\text{pump}2}$ in Figure 5.3a, we believe that the

bright state is thermally getting populated and carriers relax down to the ground state with a radiative decay of photons with the absorption resonance energy. As a consequence, upon resonant 2-ph excitation of the dark states located above and below, we observe enhanced emission at ~ 2.61 eV and ~ 3.1 eV for the 16.3° domain (Figure 5.3c) and the tunable nature of the PL emission with the domain angle (Figure 5.2c).

5.5 Power Dependence – PL and TA

The observed PL intensity had linear pump fluence dependence. Figure 5.4a. (Red) displays 2-ph PL intensity versus pump fluence for tBLG exhibiting linear behavior suggesting auger annihilation effect (exciton annihilation) which are common

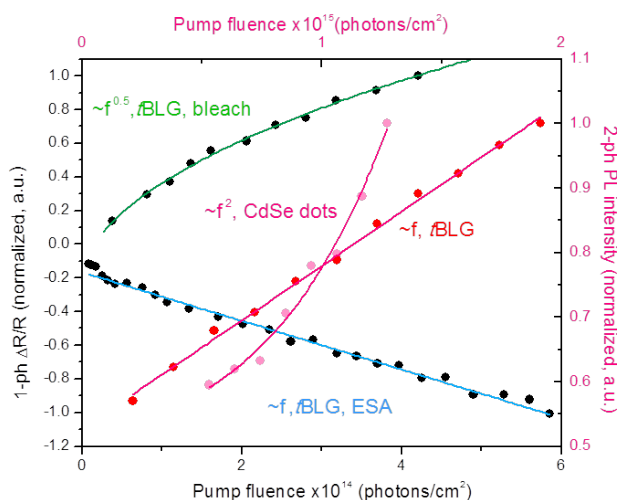


Figure 5.4: tBLG intraband, 2-ph TA, and 2-ph PL microscopy. TA and PL response vs. photon flux. tBLG TA showing square root function for GSB and linear function for ESA upon 1-ph excitation. tBLG PL showing linear function and CdSe quantum dots showing quadratic function for 2-ph excitation.

for a strongly-bound excitonic system such as SWCNTs and TMDs.^{182–187} As a control,

we see expected quadratic pump power dependence for 2-ph PL excitation of CdSe quantum dots as shown in Figure 5.4a (magenta). Our observed PL from tBLG rules out the possible SHG response as verified by; (i) the linear 2-ph PL power dependence as supposed to the expected quadratic fluence dependence for SHG response as seen in other vdW 2D materials and GaAs^{196,197}, (ii) for emission collection, optical filters in front of EMCCD blocks the possible SHG generation contribution in the signal.

5.6 Exciton Binding Energy with Near-IR Intraband TA Microscopy

We further map out the binding energy of the excitons responsible for the PL emission in tBLG. We performed 1-photon near-IR intraband TA, and 2-photon interband TA microscopy outlined in Figure 5.5a. Relative electron population in a single grain tBLG domain was obtained with a collinear pump, and probe beam in reflection geometry by raster scanning diffraction limited 140 fs tunable beam over the sample. Once the pump beam excites the sample, after a delay time t , we measure differential TA ($\Delta R(t) \propto \Delta \sigma(t)$) of a probe pulse to construct time-dependent TA differential reflection maps point by point (discussed in Chapter 2). The acquired maps are approximated by the relative photoexcited electronic population for a given probe energy and delay time between the pump and the probe. The beam is parked on the region of interest, once the tBLG domain is located with confocal scanning.

As shown in Figure 5.5, to investigate 7.8° tBLG domain, the pump beam is set to be on resonance with the 7.8° domain ($E_{\text{pump}} \sim E_\theta \sim 1.54$ eV). With near to mid-IR probe energy (0.4 eV-1.6 eV), the carriers are then promoted to the higher lying state.

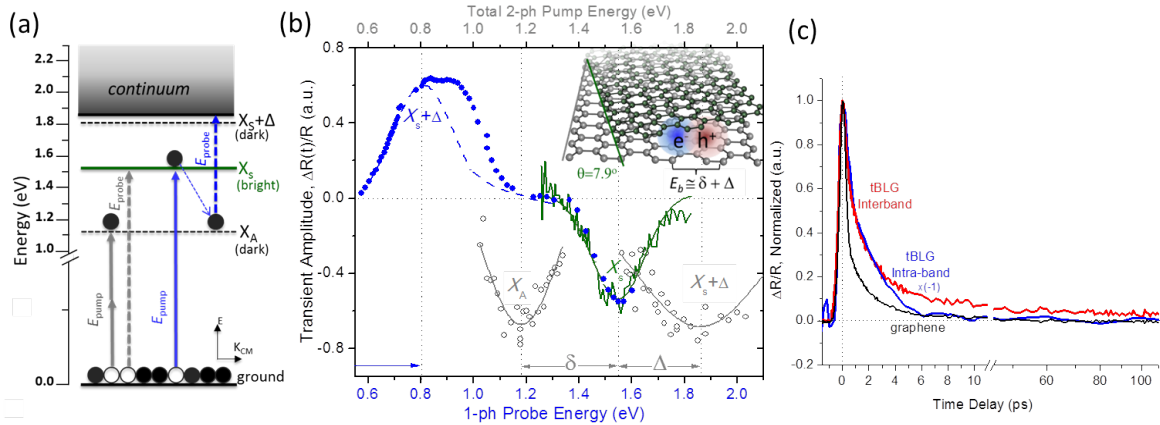


Figure 5.5: tBLG intraband and 2-ph TA microscopy. (a) TA measurements on a 7.9° tBLG domain: (Blue) 1-ph resonant pump of X_S state with near-IR intraband ESA tunable probe to quasi-continuum states, $X_S + \Delta$. (Gray): 2-ph tunable pump, X_S resonant probe. (b) 1- and 2-ph TA spectra corresponding to (a), with linear absorption spectrum in green. (c) Interband (red) and intraband (blue) dynamics showing long-lifetimes for interband transition.

We now vary the probe energy, and for the desired probe energy, pump-probe time dynamics of 7.8° tBLG domain as well as graphene were recorded. To isolate the dynamics intrinsic to the interlayer tBLG, graphene contribution is then subtracted out for each probe energy.^{46,47,129,152} For a given time delay, differential reflection intensity versus probe energy is plotted as shown in Figure 5.5b. Expectedly, the ground state bleach response matches well with the linear absorption at 1.54 eV confirming the reliability of the measurements further validating the model. We also observed a broad feature corresponding to the excited state absorption response at ~ 0.8 eV suggesting intraband transitions to the quasicontinuum state. This suggests the exciton binding energy of ~ 0.8 eV.

For comparison with the 2-ph TA microscopy, we excite the dark state X_A of 7.9° on resonance with 2-ph and probe the bright state X_S , by varying the pump energy we can map out the spectrum as shown in Figure 5.5b (gray). We find enhanced ground state bleach response for 2-ph excitation at 1.18 eV and 1.82 eV (gray) around resonance absorption at 1.54 eV (green). We can estimate the binding energy by taking: $\delta+\Delta \sim 0.7$ eV. Both of these measurements; near-IR intraband TA and 2-ph TA microscopy of exciton binding energy in 7.9° tBLG domain agree well with each other. We can additionally estimate the exciton binding energy from the 2-ph PL measurements in Figure 5.3c as $\delta+\Delta=0.5$ eV for 16.3° . The Exciton binding energy of ~ 0.7 eV for the 7.9° domain with TA measurements and the exciton binding energy of ~ 0.5 eV for the 16.3° domain with PL measurements further agree with the theoretically predicted value of 0.7 eV binding energy for 21° tBLG domain.¹⁵³The measured exciton binding energy in tBLG is comparable to other 2D excitonic materials like TMDs and is larger than the measured binding energy of 100-200 meV in semiconductor SWCNTs, and 50 meV in metallic CNTs^{175,193,198-200}. Such a large exciton binding energy opens up new avenues for excitonic applications.

Upon looking at the charge carrier dynamics in tBLG, we find long-lived interband response with lifetimes of ~ 70 ps versus ~ 5 ps for the intraband response as shown in Figure 5.5c. For comparison, we plotted short-lived (~ 5 ps) intraband dynamics of graphene. Our observations of long interband and short intraband response further enforce the bound exciton model.

Figure 5.4 shows pump power dependence of 1-ph TA ground state bleach and

ESA response of tBLG. Contribution from graphene has been subtracted out to obtain intrinsic characteristics of tBLG.^{46,47,129,152} Square root dependence for ground state bleach and linear dependence for excited state absorption response further suggest Auger annihilation effect which is common for a strongly-bound excitonic system such as s-SWCNTs and TMDs.¹⁸²⁻¹⁸⁷

5.7 Summary

In summary, we reported light emission from tBLG for the first time with ultrafast laser excitation in 2-ph photoluminescence microscopy. The observed emission is tunable with the absorption resonances of the tBLG domain. This photoemission is visible in as-grown CVD samples as well as artificially transferred samples and is independent of the substrate used. This luminescence is possible owing to the long lifetimes and bound excitons in tBLG. The relatively slow process of light emission is possible because excited carriers fully relax through slower e-e interaction and e-ph interaction. Our analysis further suggests that PL from tBLG arises when exciting dark state on resonance with 2-photons, populating the long-lived dark state which then thermally populates the bright state for photoemission. We further map out the exciton binding energy with near-IR intraband transient absorption microscopy and 2-ph photoluminescence microscopy. We find the binding energy on the order of 0.5-0.8 eV which is comparable to other 2D excitonic materials like TMDs and relatively larger than the measured binding energy of 100-200 meV in semiconductor SWCNTs, 50 meV in metallic CNTs.^{175,193,198-200} Our results support that tBLG is a first novel 2D hybrid material with bound excitons with

large binding energy alongside continuum states. This work holds promise for excitonic applications for light harvesting technology and optoelectronics device development.

5.8 Methods

tBLG was obtained with as grown CVD method or artificially transferred CVD grown single layer material. For artificially transferred tBLG, graphene was grown with an aligned CVD growth method on a copper substrate.^{24,176} The copper foil with graphene is then cut into two pieces and is then transferred in a tBLG configuration to a SiN or fused silica substrate with the artificially transferred technique described in Chapter 1 and 2. This technique can result in large domain tBLG material¹⁸⁸. The samples were characterized using the combination of hyperspectral absorption, transient absorption, and dark field TEM^{38,46,181} to locate twisted domains. The final angle assignment of the domains was done using well-established methods looking at linear absorption peak energies (see Chapter 1 and 2).

For the excited state absorption experiment and 2-ph photoluminescence measurements, synchronized Ti: Sapphire oscillator (Coherent Chameleon Ultra II) with wavelength range 680 - 1080 nm, 80 MHz repetition rate and optical parametric oscillator with wavelength range 1000 – 4000 nm was used. Excited state absorption experiment was done with confocal transient absorption microscopy.¹⁸¹ A collinear pump and a probe beam were obtained with the synchronized Ti: Sapphire oscillator with the OPO. The pump beam was modulated at 1 MHz with an AO-modulator (Gooch & Husego). The probe fluence power was 5% of the pump power. For the pump power dependence measurements, the probe power was fixed at ($\sim 1 \times 10^{12}$ photons/cm²). The beams were aligned to the mechanical delay stage, then raster scanned by the piezo-scanning mirror

and then coupled to a confocal scanning microscope with a 50X-IR objective, NA = 0.65. 140 fs FWHM pulse duration was measured by the cross correlation of the pump and probe under the objective. The spot size of the pump and the probe beams were measured to be $\sim 1.5 \mu\text{m}$ on gold pad features by fitting the reflection profile. TE cooled InGaAs detector connected to Zurich HF2LI lock-in amplifier was used to detect the transient absorption response. Appropriate optical filters in front of the detector were used to let only the probe beam through blocking the pump beam.

For the 2-ph photoluminescence microscopy measurements, the pump beam was obtained either through oscillator or OPO. The beam is then raster scanned by the piezo-scanning mirror and then coupled to a microscope with a 50X-IR objective, NA = 0.65. The back reflection of the sample was obtained with the TE cooled InGaAs detector. Long pass optical filters were used in the line before the microscope to block possible 2ω light from the laser source. The emitted photoluminescence was measured with cooled EMCCD camera (ProEm InGaAs, Princeton Instruments). Short pass and band pass optical filters were used in front of the camera for emission detection. All the measurements were performed at 295 K unless specified. Microscope objective transmission corrections, the spectral response of the detection system, and spectral characteristics of the optical filters were taken into account for each wavelength.

6. CONCLUSIONS AND OUTLOOK

6.1 Summary

The physics of 2D vdW materials and their heterostructures has recently been an area of intense study. Material properties of vdW materials change drastically as you go from 3D to 2D.^{2,3} Stacking and twisting 2D vdW materials creates further unique properties that are not accessible in a single material. Graphene is a unique 2D material from a family of carbon materials that has shown remarkable properties and applications in many areas of research and technology.^{2,3,112,201} Further, when two sheets of vdW material such as graphene are stacked at an off-axis angle creating a tBLG configuration, electronic properties are modified. As such, there are countless possibilities of designing vdW heterostructures that incorporate graphene and tBLG with other 2D materials with engineered properties. This dissertation provides a framework for imaging and studying the underlying physics of light matter interactions in such heterostructures. In particular, we focus on understanding many body interactions and their implications experimentally by filming the journey of electrons from excitation to relaxation and extraction with μm -fs space-time resolution in tBLG. We focus on better understanding the electronic properties of tBLG that may enable the development of new homo- or hetero-structure materials for a solar and photovoltaic technology.

Stacking two sheets of graphene at an off axis angle forces orbitals to rehybridize resulting in angle tunable optical absorption resonance.^{125,152} Early work on tBLG was limited to optical absorption and Raman studies. However, this dissertation focuses on

what happens beyond absorption to learn about many body interactions from interlayer interactions. We reported a novel technique, multi-photon confocal TA microscopy approach. With the developed technique, we film the journey of electrons upon fs laser excitation from excitation to relaxation and extraction in a single grain of tBLG. Surprisingly, we find that even being a semimetal, tBLG form electron relaxation bottleneck that are not present in graphene or Bernal stacked bilayer graphene. Looking closer to explain this behavior theoretically, we find that upon resonant excitation of tBLG, owing to the interlayer interactions, Fano resonance exciton states are also known to be present in graphene rehybridization.¹⁵³ The symmetric rehybridization of the two fano states form a resonant exciton state (bright state) that is still coupled to the continuum, and anti-symmetric rehybridization of the two Fano states form a stable, bound exciton state (dark or ‘ghost’ state) that is theoretically decoupled from the continuum states. In particular, we now have a model where carriers are excited by bright multiple transitions and relax impulsively to the bound exciton state where they relax at a slower rate. We further confirmed the existence of the dark state with TA multi-photon selection rules and bright-dark state splitting energy against the theoretical predictions. For the first time, this research shows that tBLG is a hybrid 2D material that forms relaxation bottleneck and is able to create bound exciton states alongside continuum states. We now believe, we have a better understanding of the interlayer interactions and the nature of rehybridized electronic states in this material.

To further investigate the nature of the excitonic states and the exciton binding energy in tBLG, we provide a framework using a near IR excited state transient absorption microscopy technique. This technique was used to study binding energy in

carbon nanotubes and some TMDs materials²⁰²⁻²⁰⁴, which can be further extended to study binding energy in other 2D materials from the TMDs family and others. We excite the bright state on resonance with a pump pulse and then promote the charge carriers to the higher lying state with near IR probe pulse. Upon measuring the excited state absorption manifold in tBLG, we reported the exciton binding energy on the order of $\sim 0.5-0.8$ eV. This binding energy is an order of magnitude larger than the binding energy of ~ 0.05 eV reported for metallic CNTs.¹⁹³ Our binding energy value agrees well with the theoretically predicted value of 0.72 eV for 21° domains. The measured exciton binding energy in tBLG is comparable to other 2D excitonic materials like TMDs and is larger than the measured binding energy of 100-200 meV in semiconductor SWCNTs as well as the reported value of 50 meV in metallic CNTs.^{193,198,199} This large exciton binding energy opens up a new avenue for excitonic applications.

Long-lived dynamics and bound exciton formation with relatively large binding energy in tBLG suggests potential photoemission owing to a combination of radiative and non-radiative decay of the carriers. We reported light emission from a semimetal, tBLG for the first time. This work provides a framework for understanding light emission in a semimetal tBLG, which can be extended to other 2D materials. We developed a unique 2-photon photoluminescence microscopy with confocal scanning and EMCCD detection. The observed photoluminescence energy is tunable with the absorption resonance energy. Our analysis suggests that photoemission arises when exciting dark state on resonance with 2-photons, populating the long-lived dark state which then thermally populates the bright state for photoemission. Although tBLG is a semimetal, due to its unique band symmetry, the bound exciton formation and long-lived dynamics make photoemission

possible. The relatively slow process of photoemission is further possible because excited carriers fully relax through slower e-e interaction and e-ph interaction. The emission was observed on as grown multilayer CVD graphene samples as well as artificially prepared samples and is independent of the substrate used. Our results hold promise for excitonic applications for light harvesting technology and optoelectronic device development discussed further in the future work.

6.2 Future Outlook

6.2.1 Introduction

Here, three potential future directions of the research presented here are discussed. It was demonstrated in the earlier Chapters that 2D materials hold promise for efficient energy harvesting technology. In particular, tBLG was found to create electronic relaxation bottleneck, and due to the unique band symmetry, bound excitons are a possibility alongside continuum states. It is possible to take advantage of these unique properties. In this Chapter, we first discuss how bound excitons can be efficiently extracted as a current generation in tBLG. In particular, the photocurrent properties of tBLG can provide useful insights to learn about intrinsic quantum efficiency for solar voltaic material development. For this study, near-field scanning optical microscopy (NSOM) AFM capabilities will be combined with the ultrafast pulsed laser source to map out current producing grains with sub-nm spatial resolution upon photon irradiation.

Second, tBLG is a non-centro symmetric system possessing properties of a chiral like molecule. As a consequence, it is possible to observe polarization and handedness of light depend optical properties in tBLG. The precise control over the position of each

layer down to the atomic scale could provide a powerful tool to create nanodevices with unique chiral properties. This could potentially have applications in polarization optics, and valleytronics. For this study, optical properties such as absorption, TA, photoluminescence, and photocurrent generation will be measured as a function of polarization and handedness of light.

Third, owing to promising optoelectronic properties of TMDs, there has been a major effort to create heterostructures by stacking two different materials to create desired properties. The rotation between the two materials further provides an extra degree of freedom to influence the interlayer coupling thus creating unique properties that are not accessible in a single material. The family of 2D materials has increased appreciably. There are a number of possible combinations for stacking and twisting 2D vdW materials to produce similar interlayer electronic states for next generation optoelectronics. For this study, materials will be chosen intelligently based on the interlayer coupling to engineer 2D material heterostructures with a twist between the two layers. Using ultrafast space-time maps of carrier relaxation as well as photocurrent generation will be measured to identify potential efficient 2D heterostructure devices.

6.2.2 Femtosecond Resolved Near-field Photocurrent Generation

Future work involves measuring the efficiency of tBLG devices to answer how the bound excitons can be efficiently extracted at a light harvesting interface. In particular, it is centered around the detailed study of the electronic and photocurrent properties of vdW material, tBLG. We predict that devices based on a twisted bilayer will have proportionally higher efficiencies because they retain the high mobility of graphene,

but the bilayer excitons should live long enough to extract efficiently. To demonstrate how strongly bound exciton states in twisted bilayer graphene can be harvested as a photocurrent, the following studies will be performed: (i) with the NSOM microscope (Figure 6.1a-b), IR-near-field microscopy will be developed to study current production down to ~ 10 nm spatial resolution. (ii) it will be further integrated with the femtosecond (~ 100 fs) time-resolution capabilities. This technique can further be extended to selectively resolve nano-femto photocurrents for the first time by combining ultrafast-photocurrent techniques (fs PC resolution). This tool will enable us to understand current generation in single grains to quantify a material's intrinsic photocurrent internal quantum efficiency (IQE) for solar voltaic material development. With this technique, space-time images of electron dynamics will be obtained from the point of excitation to the current extraction to uncover fundamental pathways and principles for efficient energy extraction in 2D materials. Near-field imaging of photocurrent spatial expansion and flow can be achieved with electro-conducting tuning fork tip combined with near and mid-IR TA microscopy.

In the scope of this study, a MutiView2000 AFM system from Nanonics Inc. with tuning fork feedback mechanism will be used. Double pipette tip with the distance between the two wires 3-10 μm was threaded with a platinum nanowire and mounted on the tuning fork as shown in the Figure 2.17. The system uses the resonance frequency

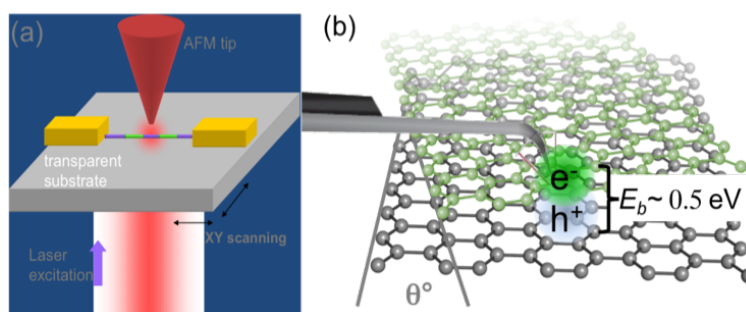


Figure 6.1: (a) Near-field optical microscope setup. (b) tBLG will have its interlayer states mapped out in the spatial domain using photoconductance based near-field current mapping.

of a tuning fork. For electrical conductivity detection, a FEMTO current preamplifier with an amplification range of 10^3 - 10^{11} will be utilized. The DC bias between the tip and the sample will be applied using a femto current preamplifier, and controller interface box with built in software or external voltage source.

This photoconductive approach allows direct visualization of nm resolved photocurrent production in 2D materials in situ.²⁰⁵ We will identify (i) the steps in photo charge generation process that are primary bottlenecks for tBLG device efficiency, (ii) for the first time, near-field microscopy technique will be employed combined with the ultrafast laser source to resolve photocurrent generation down to ~ 10 nm in tBLG. This method can be extended to other 2D materials, and it represents a needed diagnostic tool to quantify a material's intrinsic photocurrent IQE before great effort is invested in development. The knowledge gained from this study could directly impact material considerations for next generation high-efficiency solar voltaic. Research into understanding current generation in single grains of vdW material to quantify a material's intrinsic photocurrent internal quantum efficiency will be an invaluable contribution for

engineering higher performance material for solar voltaic technology to meet the energy needs.

6.2.3 Polarization and Handedness Dependent Optical Properties of tBLG

Spintronic devices need control over spin polarization of the system to access and manipulate information.^{206–209} 2D vdW materials can provide a platform for spin and valleytronic owing to their unique structure. In the electronic band structure of these crystals, a local minimum in the conduction band or local maximum in the valence band is referred to as a valley. The hexagonal 2D materials such as tBLG and group –VI TMDs have inversion-asymmetric honeycomb lattice structures, which produces two inequivalent yet degenerate in energy momentum-space valleys +K and –K. This creates pseudospin systems equivalent to electron spin.²¹⁰ Now, in addition to charge and spin, there is an extra valley degree of freedom. Through valley dependent optical selection rules, circularly polarized light excitation can generate large spin-valley polarizations.^{210–213} For practical spin-valleytronics, spin-valley polarization lifetimes need to be longer for efficient electron-hole separation. There has been some recent development in engineering heterostructures to realize large spin-valley polarization lifetimes by studying observables such as circular dichroism (CD), photoluminescence (PL), and photocurrent with helicity dependent excitations.

Recently, there was a study on tBLG where the left and right handed graphene bilayers were created, and a strong CD with the highest ellipticity value was reported. Also, the CD peak energy and the response sign was reported to be tunable with the angle between the two layers and polarity.¹⁸⁸ These properties arise from a large in-plane magnetic moment associated with the interlayer optical transition. Figure 6.2a shows a

CD spectrum which is essentially the polarization change of transmitted light of left and right handed tBLG showing enhanced responses labeled with A and B for a 16.5° domain whereas single layer graphene does not show negligible values. The peak energies correspond to the interlayer transitions, and they shift sign for left and right handed tBLG domains. The inset shows CD response for incident energy as a function of energy. This study demonstrates chiral dependent properties of tBLG exploring spin and valley degree of freedom.¹⁸⁸ Figure 6.2b shows helicity dependent photoluminescence in a 2D heterostructure of MoSe₂-WSe₂ with the twist angle nearly aligned, the conduction band of MoSe₂ aligns with the valence band of Wse₂. Under sigma + polarized excitation, dominantly co-polarized interlayer exciton PL emission is seen.

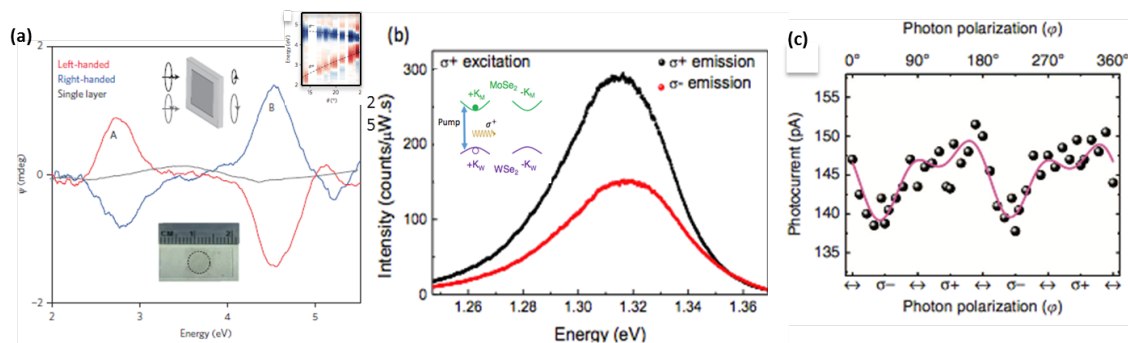


Figure 6.2: Optical activity, photoluminescence, and photocurrent in as a function of handedness of light. (a) CD spectrum shows strong peaks (labeled) from the right and left handed tBLG domains. The inset shows CD as a function of angle and excitation energy.¹⁸⁸ (b) PL emission from MoSe₂-WSe₂ heterostructure with σ^+ polarized excitation. Inset shows carriers are pumped into the σ^+ valley.²¹⁴ (c) Photocurrent as a function of polarization of incident light on resonance showing different valley currents due to σ^+ and σ^- excitation.²¹⁵ [Adapted from ^{214, 215}.]

The inset shows that the carriers are into the K^+ valley with the optical pump. This study suggests interlayer charge transfer processes would preserve spin-valley polarization.²¹⁴

Another study with photocurrent as an observable further demonstrates spin coupled valley dependence of optical properties. Figure 6.2c shows photocurrent as a function of the angle of circular polarization of photon in MoS₂. For off-resonant excitation, there was no change seen in the sigma+ and sigma- excitation in the photocurrent. On the other hand, upon resonant excitation, photocurrent exhibits a clear difference between sigma+ and sigma - excitations corresponding to spin-coupled valley currents in K+ and K- respectively. These results shed light into the opto-valleytronic device community.²¹⁵

Although Kim et al.¹⁸⁸ demonstrated chiral behavior in tBLG, there has not been any study on helicity dependent carrier lifetimes, PL, and photocurrent on tBLG.

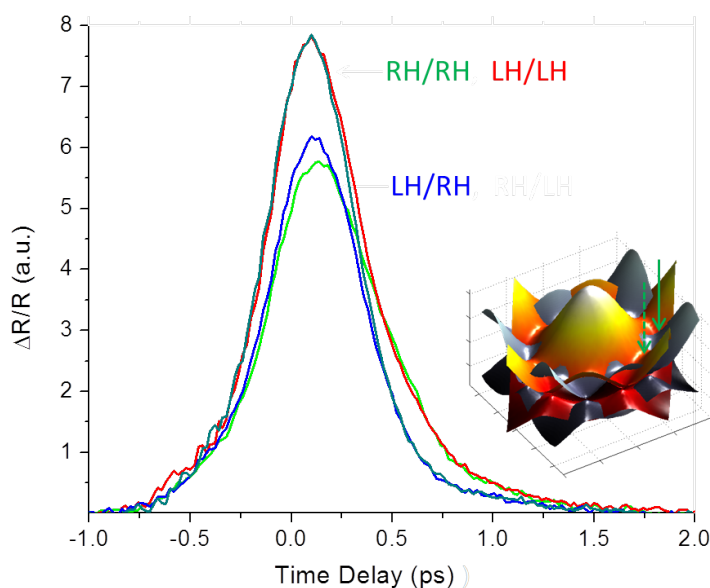


Figure 6.3: Helicity dependent off-resonant time dynamics of tBLG. Same helicity pump and probe beam produce larger intensity as compared to the opposite helicity pump and probe beam.

tBLG may provide useful insight owing to the hybrid nature with bound excitons alongside continuum states through helicity dependent optical properties for the spin and

valleytronic applications. As a preliminary study, we have performed TA experiment to study carrier lifetimes and see how helicity effects it. Figure 6.3 shows time dynamics of tBLG for off resonant pump and probe beams. Right handed pump and probe beam produce a similar response as left-handed pump and probe beam. Whereas Left handed pump, right handed probe or the other way around gives lower intensity than the same helicity pump and probe beam. We will obtain resonant time dynamics and TA spectrum with same and opposite helicity pump and probe beam to complete this study. Similar studies will be performed for photoluminescence, and photocurrent generation to understand the spin-valley coupled currents and spin-valley polarization. This work may shed light on the potential useful application in spin polarization for reading, writing and transferring information.

6.2.4 Engineering 2D vdW Heterostructures With and Without Twist

Stacking 2D crystals with different properties to achieve desired optoelectronic properties is a very powerful method to create designer heterostructures.²¹⁶ Stacking angle between layers further provides another degree of freedom. In designing these vdW heterostructures, interlayer coupling between the layers involved play a critical role as shown for graphene-h-BN, and TMD based heterostructures.^{216–222} It has also been shown that rotational alignment between layers can influence the interlayer coupling.^{223–226} It is still not well understood if interlayer coupling can be used as a design parameter for creating the desired heterostructure.²²⁷

Figure 3a shows cross-circularly polarized differential transmission measurement on almost aligned MoSe₂-WSe₂ heterostructure.⁹⁸ It shows individual monolayer responses and the heterostructure response. In the heterostructure, the enhanced response

from individual monolayer is seen at the similar spectral position with a ~ 20 meV redshift with a broader lineshape. The coupling between layers reducing the intralayer exciton bandgap causes the redshift. The charge transfer between the layers causes the broader lineshape that essentially created extra pathways for intralayer exciton relaxation.²²⁸ By tuning the angle between two layers, the interlayer coupling can be further modified which could result in the modified differential spectrum.

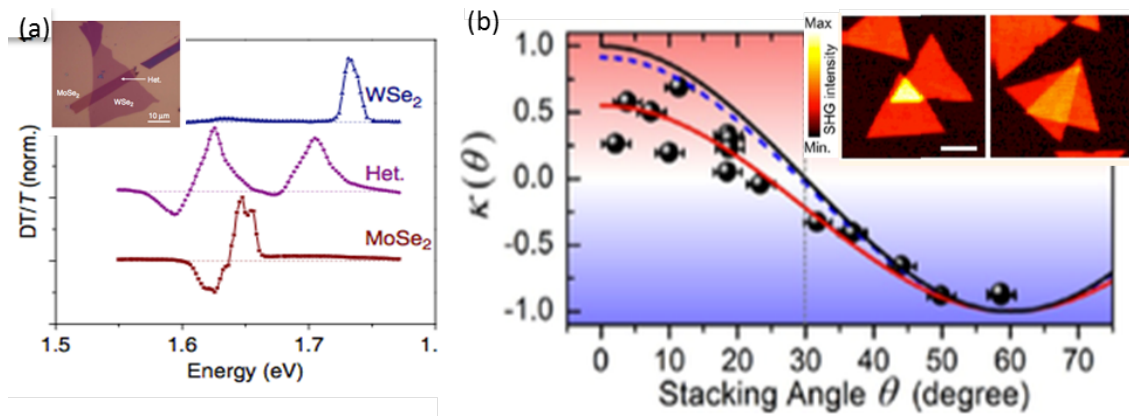


Figure 6.4: (a) Differential transmission spectrum from WSe₂, heterostructure, and MoSe₂ region shown in the inset.⁹⁸ (b) SHG from WSe₂-WS₂ heterostructure as a function of twist angle between two layers. The inset shows spatial SHG maps for 2° and 30° rotation.²²⁹ [Adapted from^{98, 229} .]

Another example of such a heterostructure is shown in Figure 6.4b where second harmonic generation from different TMD twisted bilayer heterostructures are studied. The SHG response as a function of the angle between two layers in WSe₂-WS₂ heterostructure shows the maximum response for smaller angle domains. The inset shows SHG maps for 2° and 30° domain. Similar SHG response as a function of angle was reported in the same study for WSe₂-MoS₂, WSe₂-WS₂ heterostructure. The second

harmonic field from the stacked structure is a coherent superposition of the second harmonic fields from individual layers with a phase difference.²²⁹

We will study how interlayer coupling in twisted heterostructures affects the electronic structure. There are endless possible combinations for stacking and twisting 2D vdW materials to produce desired interlayer electronic states for next generation optoelectronics. Materials for stacking will be chosen intelligently based on the interlayer coupling to engineer 2D material heterostructures with a twist between the two layers. Ultrafast space-time maps of carrier relaxation as well as photocurrent generation will be measured to identify potential efficient 2D heterostructure devices for optoelectronic technology.

7. BIBLIOGRAPHY

1. Norio Taniguchi. On the Basic Concept of 'Nano-Technology'. in *On the Basic Concept of 'Nano-Technology'* (Proc. Intl. Conf. Prod. Eng. Tokyo, Part II, Japan Society of Precision Engineering, 1974., 1974).
2. Novoselov, K. S. *et al.* Electric field effect in atomically thin carbon films. *Science (80-.)*. **306**, 666–669 (2004).
3. Novoselov, K. S. *et al.* Two-dimensional atomic crystals. *Proc. Natl. Acad. Sci.* **102**, 10451–10453 (2005).
4. Lee, C., Wei, X., Kysar, J. W. & Hone, J. Measurement of the Elastic Properties and Intrinsic Strength of Monolayer Graphene. *Science (80-.)*. **321**, 385–388 (2008).
5. Meric, I. *et al.* Current saturation in zero-bandgap, top-gated graphene field-effect transistors. *Nat. Nanotechnol.* **3**, 654–659 (2008).
6. Zhu, Y., Sun, Z., Yan, Z., Jin, Z. & Tour, J. M. Rational Design of Hybrid Graphene Films for High-Performance Transparent Electrodes. *ACS Nano* **5**, 6472–6479 (2011).
7. Park, H., Rowehl, J. A., Kim, K. K., Bulovic, V. & Kong, J. Doped graphene electrodes for organic solar cells. *Nanotechnology* **21**, 505204 (2010).
8. Xia, F., Mueller, T., Lin, Y., Valdes-Garcia, A. & Avouris, P. Ultrafast graphene photodetector. *Nat. Nanotechnol.* **4**, 839–843 (2009).
9. Blase, X., Rubio, A., Louie, S. G. & Cohen, M. L. Quasiparticle band structure of bulk hexagonal boron nitride and related systems. *Phys. Rev. B* **51**, 6868–6875 (1995).

10. Song, Y. *et al.* Triggering the atomic layers control of hexagonal boron nitride films. *Appl. Surf. Sci.* **313**, 647–653 (2014).
11. Nair, R. R. *et al.* Fine Structure Constant Defines Visual Transparency of Graphene. *Science (80-.)*. **320**, 2008 (2008).
12. Novoselov, K. S., Mishchenko, A., Carvalho, A. & Castro Neto, A. H. 2D materials and van der Waals heterostructures. *Science (80-.)*. **353**, aac9439-aac9439 (2016).
13. Mak, K. F., Lee, C., Hone, J., Shan, J. & Heinz, T. F. Atomically thin MoS₂: A new direct-gap semiconductor. *Phys. Rev. Lett.* **105**, 2–5 (2010).
14. Bhimanapati, G. R. *et al.* Recent Advances in Two-Dimensional Materials beyond Graphene. *ACS Nano* **9**, 11509–11539 (2015).
15. Nicolosi, V., Chhowalla, M., Kanatzidis, M. G., Strano, M. S. & Coleman, J. N. Liquid Exfoliation of Layered Materials. *Science (80-.)*. **340**, 1226419 (2013).
16. Dreyer, D. R., Park, S., Bielawski, C. W. & Ruoff, R. S. The chemistry of graphene oxide. (2009). doi:10.1039/b917103g
17. Nicolosi, V., Chhowalla, M., Kanatzidis, M. G., Strano, M. S. & Coleman, J. N. Liquid Exfoliation of Layered Materials. *Science (80-.)*. **340**, 1226419–1226419 (2013).
18. Joensen, P., Frindt, R. F. & Morrison, S. R. Single-layer MoS₂. *Mater. Res. Bull.* **21**, 457–461 (1986).
19. Eda, G. *et al.* Photoluminescence from Chemically Exfoliated MoS₂. (2011). doi:10.1021/nl201874w
20. M, C. Photoluminescence from Chemically Exfoliated MoS₂. *Nano Lett.* **12**, 526

- (2012).
21. Yu, J., Li, J., Zhang, W. & Chang, H. Synthesis of high quality two-dimensional materials via chemical vapor deposition. *Chem. Sci.* **6**, 6705–6716 (2015).
 22. Tsen, A. W., Brown, L., Havener, R. W. & Park, J. Polycrystallinity and stacking in CVD graphene. *Acc. Chem. Res.* **46**, 2286–2296 (2013).
 23. Li, X. *et al.* Large-area synthesis of high-quality and uniform graphene films on copper foils. *Science (80-.)*. **324**, 1312–1314 (2009).
 24. Brown, L. *et al.* Polycrystalline graphene with single crystalline electronic structure. *Nano Lett.* **14**, 5706–5711 (2014).
 25. Hao, L. *et al.* Self-supporting graphene films and their applications. *IET Circuits, Devices Syst.* **9**, 420–427 (2015).
 26. Goniszewski, S. *et al.* Correlation of p-doping in CVD Graphene with Substrate Surface Charges. doi:10.1038/srep22858
 27. Kang, J., Tongay, S., Zhou, J., Li, J. & Wu, J. Band offsets and heterostructures of two-dimensional semiconductors. *Appl. Phys. Lett.* **102**, 22–25 (2013).
 28. Ling, X. *et al.* Role of the Seeding Promoter in MoS₂ Growth by Chemical Vapor Deposition. *Nano Lett.* **14**, 464–472 (2014).
 29. Liu, Z. K. *et al.* Discovery of a Three-Dimensional Topological Dirac Semimetal, Na₃Bi.
 30. Sutter, P., Cortes, R., Lahiri, J. & Sutter, E. Interface formation in monolayer graphene-boron nitride heterostructures. *Nano Lett.* **12**, 4869–4874 (2012).
 31. Huang, C. *et al.* Lateral heterojunctions within monolayer MoSe₂–WSe₂ semiconductors. *Nat. Mater.* **13**, 1–6 (2014).

32. Duan, X. *et al.* Lateral epitaxial growth of two-dimensional layered semiconductor heterojunctions. (2014). doi:10.1038/NNANO.2014.222
33. Zhang, X.-Q., Lin, C.-H., Tseng, Y.-W., Huang, K.-H. & Lee, Y.-H. Synthesis of Lateral Heterostructures of Semiconducting Atomic Layers. doi:10.1021/nl503744f
34. Gong, Y. *et al.* Vertical and in-plane heterostructures from WS₂/MoS₂ monolayers. (2014). doi:10.1038/NMAT4091
35. Novoselov, K. S. Electric Field Effect in Atomically Thin Carbon Films. *Science* (80-.). **666**, 666–670 (2010).
36. Blake, P. *et al.* Making graphene visible. *Appl. Phys. Lett.* **91**, 2007–2009 (2007).
37. Benameur, M. M. *et al.* Visibility of dichalcogenide nanolayers. *Nanotechnology* **22**, 125706 (2011).
38. Havener, R. W. *et al.* Hyperspectral imaging of structure and composition in atomically thin heterostructures-Supporting information. *Nano Lett.* **13**, 3942–3946 (2013).
39. Yu, P. Y. & Cardona, M. *Fundamentals of Semiconductors: Physics and Materials Properties*, 4th Edition.
40. Kim, K. K. *et al.* Synthesis of Monolayer Boron Nitride on Cu Foil Using Chemical Vapor Deposition. *Nano Lett.* **xx**, xx (2011).
41. Mak, K. F., Shan, J. & Heinz, T. F. Seeing many-body effects in single- and few-layer graphene: Observation of two-dimensional saddle-point excitons. *Phys. Rev. Lett.* **106**, 1–4 (2011).
42. Chae, D.-H. H. *et al.* Excitonic fano resonance in free-standing graphene. *Nano*

- Lett.* **11**, 1379–1382 (2011).
43. Mak, K. F., Lui, C. H., Shan, J. & Heinz, T. F. Observation of an electric-field-induced band gap in bilayer graphene by infrared spectroscopy. *Phys. Rev. Lett.* **102**, 100–103 (2009).
 44. Zhang, Y. *et al.* Direct observation of a widely tunable bandgap in bilayer graphene. *Nature* **459**, 820–823 (2009).
 45. Robinson, J. T. *et al.* Electronic Hybridization of Large-Area Stacked Graphene Films. **7**, 637–644 (2013).
 46. Havener, R. W., Zhuang, H., Brown, L., Hennig, R. G. & Park, J. Angle-resolved raman imaging of interlayer rotations and interactions in twisted bilayer graphene. *Nano Lett.* **12**, 3162–3167 (2012).
 47. Wang, Y. *et al.* Stacking-dependent optical conductivity of bilayer graphene. *ACS Nano* **4**, 4074–4080 (2010).
 48. Moon, P. & Koshino, M. Optical absorption in twisted bilayer graphene. *Phys. Rev. B - Condens. Matter Mater. Phys.* **87**, 1–11 (2013).
 49. Animation for the Principle of Fluorescence and UV-Visible Absorbance | Analytical Chemistry | PharmaXChange.info. Available at: <http://pharmaxchange.info/press/2013/03/animation-for-the-principle-of-fluorescence-and-uv-visible-absorbance/>. (Accessed: 21st July 2017)
 50. Thewalt, M. L. W., Watkins, S. P., Ziemelis, U. O., Lightowlers, E. C. & Henry, M. O. Photoluminescence lifetime, absorption and excitation spectroscopy measurements on isoelectronic bound excitons in beryllium-doped silicon. *Solid State Commun.* **44**, 573–577 (1982).

51. Kim, J. G., Yun, W. S., Jo, S., Lee, J. & Cho, C.-H. Effect of interlayer interactions on exciton luminescence in atomic-layered MoS₂ crystals. (2016). doi:10.1038/srep29813
52. Steinhoff, A. *et al.* Efficient Excitonic Photoluminescence in Direct and Indirect Band Gap Monolayer MoS₂. *Nano Lett.* **15**, 6841–6847 (2015).
53. Lin, Y. S. M. M. I. of T. Optical properties of two-dimensional transition metal dichalcogenides. (2014).
54. McCreary, K. M., Hanbicki, A. T., Jernigan, G. G., Culbertson, J. C. & Jonker, B. T. Synthesis of Large-Area WS₂ monolayers with Exceptional Photoluminescence. *Sci. Rep.* **6**, 19159 (2016).
55. Berera, R., van Grondelle, R. & Kennis, J. T. M. Ultrafast transient absorption spectroscopy: principles and application to photosynthetic systems. *Photosynth. Res.* **101**, 105–18 (2009).
56. Jimenez, R. and G. R. F. Ultrafast Spectroscopy of Photosynthetic Systems. *Kluwer Acad. Publ. Dordrecht.* p. 409.
57. Joly, A. G. & Nelson, K. A. Femtosecond transient absorption spectroscopy of chromium hexacarbonyl in methanol: observation of initial excited states and carbon monoxide dissociation. *J. Phys. Chem.* **93**, 2876–2878 (1989).
58. Ronayne, K. L., Ward, a D. & Towrie, M. Transient absorption microscopy. *Spectroscopy* 2006–2008 (2007).
59. Huang, L. *et al.* Ultrafast transient absorption microscopy studies of carrier dynamics in epitaxial graphene. *Nano Lett.* **10**, 1308–1313 (2010).
60. Lytle, F. E., Parrish, R. M. & Barnes, W. T. An Introduction to Time-Resolved

- Pump / Probe Spectroscopy. *Appl. Spectrosc.* **39**, (1985).
61. Basic Spectroscopy. Available at: http://photobiology.info/Nonell_Viappiani.html. (Accessed: 21st July 2017)
 62. Raman, C. V. & Krishnan, K. S. A New Type of Secondary Radiation. *Nature* **121**, 501–502 (1928).
 63. Byrne, H. J., Sockalingum, G. D. & Stone, N. *Raman Microscopy: Complement or Competitor? Biomedical Applications of Synchrotron Infrared Microspectroscopy: A Practical Approach* (2011). doi:10.1039/9781849731997-00105
 64. Havener, R. W., Tsen, A. W., Choi, H. C. & Park, J. Laser-based imaging of individual carbon nanostructures. *NPG Asia Mater.* **3**, 91–99 (2011).
 65. Krauss, B. *et al.* Laser-induced disassembly of a graphene single crystal into a nanocrystalline network. *Phys. Rev. B - Condens. Matter Mater. Phys.* **79**, 1–9 (2009).
 66. Huang, P. Y. *et al.* Grains and grain boundaries in single-layer graphene atomic patchwork quilts. *Nature* **469**, 389–92 (2011).
 67. Mohiuddin, T. M. G. *et al.* Uniaxial strain in graphene by Raman spectroscopy: G peak splitting, Grüneisen parameters, and sample orientation. *Phys. Rev. B - Condens. Matter Mater. Phys.* **79**, 1–8 (2009).
 68. Lui, C. H. *et al.* Imaging stacking order in few-layer graphene. *Nano Lett.* **11**, 164–169 (2011).
 69. Ferrari, A. C. & Basko, D. M. Raman spectroscopy as a versatile tool for studying the properties of graphene. *Nat. Nanotechnol.* **8**, 235–246 (2013).

70. Malard, L. M., Pimenta, M. A., Dresselhaus, G. & Dresselhaus, M. S. Raman spectroscopy in graphene. *Phys. Rep.* **473**, 51–87 (2009).
71. Yu, Q. *et al.* Control and characterization of individual grains and grain boundaries in graphene grown by chemical vapour deposition. *Nat. Mater.* **10**, (2011).
72. Ogawa, Y. *et al.* Structure and transport properties of the interface between CVD-grown graphene domains. doi:10.1039/c3nr06828e
73. Tan, P. H. *et al.* The Shear Mode of Multi-Layer Graphene. *Engineering* 1–6 (2011). doi:10.1038/nmat3245
74. You, Y., Ni, Z., Yu, T. & Shen, Z. Edge chirality determination of graphene by Raman spectroscopy. *Appl. Phys. Lett.* **93**, 2006–2009 (2008).
75. Ferrari, A. C. *et al.* Raman spectrum of graphene and graphene layers. *Phys. Rev. Lett.* **97**, 1–4 (2006).
76. Reina, A. *et al.* Large area, few-layer graphene films on arbitrary substrates by chemical vapor deposition. *Nano Lett.* **9**, 30 (2008).
77. Graf, D. *et al.* Spatially Resolved Raman Spectroscopy of Single-and Few-Layer Graphene. doi:10.1021/nl061702a
78. Zeng, J. *et al.* Irradiation effects of graphene and thin layer graphite induced by swift heavy ions. *Chinese Phys. B* **24**, 86103 (2015).
79. Liao, L. *et al.* Van Hove Singularity Enhanced Photochemical Reactivity of Twisted Bilayer Graphene. *Nano Lett.* **15**, 5585–5589 (2015).
80. Ni, Z. *et al.* G -band Raman double resonance in twisted bilayer graphene: Evidence of band splitting and folding. *Phys. Rev. B - Condens. Matter Mater. Phys.* **80**, 1–5 (2009).

81. Kim, K. *et al.* Raman spectroscopy study of rotated double-layer graphene: Misorientation-angle dependence of electronic structure. *Phys. Rev. Lett.* **108**, 1–6 (2012).
82. Xie, C., Chen, D. & Li, Y.-Q. Raman sorting and identification of single living micro-organisms with optical tweezers. *Opt. Lett.* **30**, 1800–1802 (2005).
83. Minsky, M. Memoir on inventing the confocal scanning microscope. *Scanning* **10**, 128–138 (1988).
84. Imaging, N. R. C. (US) C. on R. C. through A. C. *Visualizing Chemistry. Visualizing Chemistry: The Progress and Promise of Advanced Chemical Imaging* (National Academies Press (US), 2006). doi:10.17226/11663
85. Havener, R. W. *et al.* High-throughput graphene imaging on arbitrary substrates with widefield raman spectroscopy. *ACS Nano* **6**, 373–380 (2012).
86. Batchelder, D. N., Cheng, C., Müller, W. & Smith, B. J. E. A compact Raman microprobe/microscope: Analysis of polydiacetylene Langmuir and Langmuir-Blodgett films. *Makromol. Chemie. Macromol. Symp.* **46**, 171–179 (1991).
87. Treado, P. J., Levin, I. R. A. W. & Lewis, E. N. E. L. rapid communication High-Fidelity Raman Imaging Spectrometry : A Rapid Method Using an Acousto-optic Tunable Filter. **46**, 1211–1216 (1992).
88. Puppels, G. J., Grond, M. & Greve, J. Direct Imaging Raman Microscope Based on Tunable Wavelength Excitation and Narrow-Band Emission Detection. **47**, (1993).
89. Schlu, S., Schaeberle, M. D., Huffman, S. W. & Levin, I. W. Raman Microspectroscopy: A Comparison of Point, Line, and Wide-Field Imaging

- Methodologies. **75**, 4312–4318 (2003).
90. Kaminska, K., Lefebvre, J., Austing, D. G. & Finnie, P. Real-time in situ Raman imaging of carbon nanotube growth. *Nanotechnology* **18**, 165707 (2007).
 91. Meyer, J. C. *et al.* Accurate measurement of electron beam induced displacement cross sections for single-layer graphene. *Phys. Rev. Lett.* **108**, 1–6 (2012).
 92. Kotakoski, J. & Meyer, J. C. Mechanical properties of polycrystalline graphene based on a realistic atomistic model. *Phys. Rev. B - Condens. Matter Mater. Phys.* **85**, 1–6 (2012).
 93. Meyer, J. C. *et al.* The structure of suspended graphene sheets. *Nature* **446**, 60–3 (2007).
 94. Dong, N. *et al.* Optical Limiting and Theoretical Modelling of Layered Transition Metal Dichalcogenide Nanosheets. *Sci. Rep.* **5**, 14646 (2015).
 95. Krivanek, O. L. *et al.* Atom-by-atom structural and chemical analysis by annular dark-field electron microscopy. *Nature* **464**, 571–574 (2010).
 96. Graphene, P. *et al.* Grain Boundary Mapping in. *ACS Nano* **5**, 2142–2146 (2011).
 97. van der Zande, A. M. *et al.* Grains and grain boundaries in highly crystalline monolayer molybdenum disulphide. *Nat. Mater.* **12**, 554–61 (2013).
 98. Schaibley, J. R. *et al.* Directional interlayer spin-valley transfer in two-dimensional heterostructures. *Nat. Commun.* **7**, 13747 (2016).
 99. Graf, D., Molitor, F., Ensslin, K. & Stampfer, C. Spatially resolved Raman spectroscopy of single-and few-layer graphene. *Nano Lett.* **7**, 238–42 (2007).
 100. Wu, B. *et al.* Self-organized graphene crystal patterns. *NPG Asia Mater.* **5**, (2013).
 101. Lv, R. *et al.* Transition metal dichalcogenides and beyond: Synthesis, properties,

- and applications of single- and few-layer nanosheets. *Acc. Chem. Res.* **48**, 56–64 (2015).
102. Vernon-Parry, K. D. Scanning electron microscopy: an introduction. *III-Vs Rev.* **13**, 40–44 (2000).
 103. Lee, H. C. *et al.* Review of the synthesis, transfer, characterization and growth mechanisms of single and multilayer graphene. *RSC Adv.* **7**, 15644–15693 (2017).
 104. Tu, Z. *et al.* Controllable growth of 1-7 layers of graphene by chemical vapour deposition. *Carbon N. Y.* **73**, 252–258 (2014).
 105. Probe, S. & Spm, M. A Practical Guide to.
 106. Meyer, E. Atomic force microscopy. *Prog. Surf. Sci.* **41**, 3–49 (1992).
 107. Seo, Y. & Jhe, W. Atomic force microscopy and spectroscopy. *Reports Prog. Phys.* **71**, 16101 (2008).
 108. Martin, Y., Williams, C. C. & Wickramasinghe, H. K. Atomic force microscope–force mapping and profiling on a sub 100-Å scale. *J. Appl. Phys.* **61**, 4723–4729 (1987).
 109. Xu, K., Cao, P. & Heath, J. R. Graphene Visualizes the First Water Adlayers on Mica at Ambient Conditions. *Science (80-.).* **329**, 1188–1191 (2010).
 110. Park AFM Systems. Atomic Force Microscope Modes & Technique | Park Systems. Available at: <http://www.parkafm.com/index.php/park-afm-modes/130-products/park-afm-modes>. (Accessed: 22nd August 2017)
 111. Bertolazzi, S. *et al.* Exploring Flatland: AFM of mechanical and electrical properties of graphene, MoS₂ and other low-dimensional materials. *Microsc. Anal.* 21–24 (2013).

112. Zhang, Y., Tan, Y., Stormer, H. & Kim, P. Experimental observation of the quantum Hall effect and Berry's phase in graphene. *Nature* **438**, 201–204 (2005).
113. Das, A. *et al.* Monitoring dopants by Raman scattering in an electrochemically top-gated graphene transistor. *Nat. Nanotechnol.* **3**, 210–215 (2008).
114. Gorbachev, R. V. *et al.* Hunting for monolayer boron nitride: Optical and raman signatures. *Small* **7**, 465–468 (2011).
115. O'Shea, S. J. Conducting atomic force microscopy study of silicon dioxide breakdown. *J. Vac. Sci. Technol. B Microelectron. Nanom. Struct.* **13**, 1945 (1995).
116. Murrell, M. P. *et al.* Spatially resolved electrical measurements of SiO₂ gate oxides using atomic force microscopy. *Appl. Phys. Lett.* **62**, 786–788 (1993).
117. Lee, H. J. & Park, S.-M. Electrochemistry of Conductive Polymers. 30. Nanoscale Measurements of Doping Distributions and Current–Voltage Characteristics of Electrochemically Deposited Polypyrrole Films. *J. Phys. Chem. B* **108**, 1590–1595 (2004).
118. Kremmer, S. *et al.* Nanoscale morphological and electrical homogeneity of HfO₂ and ZrO₂ thin films studied by conducting atomic-force microscopy. *J. Appl. Phys.* **97**, 74315 (2005).
119. Tejedor, P., Díez-Merino, L., Beinik, I. & Teichert, C. Conductive atomic force microscopy study of InAs growth kinetics on vicinal GaAs (110). *Appl. Phys. Lett.* **95**, 123103 (2009).
120. Beinik, I. *et al.* Nanoscale electrical characterization of arrowhead defects in GaInP thin films grown on Ge. doi:10.1116/1.3454373

121. De Wolf, P., Snauwaert, J., Clarysse, T., Vandervorst, W. & Hellemans, L. Characterization of a point-contact on silicon using force microscopy-supported resistance measurements. *Appl. Phys. Lett.* **66**, 1530–1532 (1995).
122. Olbrich, A., Ebersberger, B. & Boit, C. Conducting atomic force microscopy for nanoscale electrical characterization of thin SiO₂. http://oasc12039.247realmedia.com/RealMedia/ads/click_lx.ads/www.aip.org/pt/adcenter/pdfcover_test/L-37/1560419294/x01/AIP-PT/APL_ArticleDL_071217/CiSE_BeakerPipes_1640x440.jpg/434f71374e315a556e61414141774c75?x (1998). doi:10.1063/1.122690
123. Ahmad, M. *et al.* Nanoscale investigation of charge transport at the grain boundaries and wrinkles in graphene film. *Nanotechnology* **23**, 285705 (2012).
124. Coffey, D. C., Reid, O. G., Rodovsky, D. B., Bartholomew, G. P. & Ginger, D. S. Mapping Local Photocurrents in Polymer / Fullerene Solar Cells with Photoconductive Atomic Force Microscopy. *Nano* 1–4 (2007). doi:10.1021/nl062989e
125. Li, G. *et al.* Observation of Van Hove singularities in twisted graphene layers. *Nat. Phys.* **6**, 109–113 (2009).
126. Lahiri, J., Lin, Y., Bozkurt, P., Oleynik, I. I. & Batzill, M. An extended defect in graphene as a metallic wire. *Nat. Nanotechnol.* **5**, 326–329 (2010).
127. Introduction to Scanning Tunneling Microscopy.
128. Chaika, A. N. Electron Orbital Contribution in Distance-Dependent STM Experiments. doi:10.5772/63270
129. Brihuega, I. *et al.* Unraveling the intrinsic and robust nature of van hove

- singularities in twisted bilayer graphene by scanning tunneling microscopy and theoretical analysis. *Phys. Rev. Lett.* **109**, 1–5 (2012).
130. Bai, C. *Scanning tunneling microscopy and its application*. (Springer, 2000).
 131. Lee, C. *et al.* Anomalous lattice vibrations of single-and few-layer MoS₂. *ACS Nano* **4**, 2695–700 (2010).
 132. Bandstructure, L. & Graphene, O. Recall that $\sim x \frac{1}{2}$ denote the position of the two carbon atoms within the unit-cell. Applying for.
 133. Takase, K., Tanabe, S., Sasaki, S., Hibino, H. & Muraki, K. Transport spectroscopy of epitaxial graphene on SiC using quantum capacitances.
 134. Novoselov, K. S. *et al.* Two-dimensional atomic crystals. *Proc. Natl. Acad. Sci.* **102**, 10451–10453 (2005).
 135. Castro, E. V *et al.* Electronic properties of a biased graphene bilayer. *J. Phys. Condens. Matter* **22**, 175503–14 (2010).
 136. Kuzmenko, A. B., Crassee, I., van der Marel, D., Blake, P. & Novoselov, K. S. Determination of the gate-tunable band gap and tight-binding parameters in bilayer graphene using infrared spectroscopy. *Phys. Rev. B* **80**, 165406 (2009).
 137. Min, H., Sahu, B., Banerjee, S. K. & MacDonald, A. H. *Ab initio* theory of gate induced gaps in graphene bilayers. *Phys. Rev. B* **75**, 155115 (2007).
 138. Latil, S. & Henrard, L. Charge carriers in few-layer graphene films. *Phys. Rev. Lett.* **97**, 36803 (2006).
 139. Aoki, M. & Amawashi, H. Dependence of band structures on stacking and field in layered graphene. *Solid State Commun.* **142**, 123–127 (2007).
 140. Neto, A. H. C. *et al.* The electronic properties of graphene. *Rev. Mod. Phys.* **81**,

- 109–162 (2009).
141. Shallcross, S., Sharma, S., Kandelaki, E. & Pankratov, O. A. Electronic structure of turbostratic graphene. *Phys. Rev. B* **81**, 165105 (2010).
 142. Shallcross, S., Sharma, S. & Pankratov, O. Emergent momentum scale, localization, and van Hove singularities in the graphene twist bilayer. 245403 (2013). doi:10.1103/PhysRevB.87.245403
 143. Graham, M. W. *et al.* Transient Absorption and Photocurrent Microscopy Show That Hot Electron Supercollisions Describe the Rate-Limiting Relaxation Step in Graphene. *Nano Lett.* **13**, 5497–5502 (2013).
 144. Bistritzer, R. & Macdonald, A. H. No Title. *Proc. Natl. Acad. Sci. U. S. A.* **108**, 12233–7 (2011).
 145. Brihuega, I. *et al.* Unraveling the Intrinsic and Robust Nature of van Hove Singularities in Twisted Bilayer Graphene by Scanning Tunneling Microscopy and Theoretical Analysis. **20**,
 146. Trambly De Laissardière, G., Mayou, D. & Magaud, L. Localization of Dirac Electrons in Rotated Graphene Bilayers. *Nano Lett.* **10**, 804–808 (2010).
 147. Wang, F. *et al.* Observation of Excitons in One-Dimensional Metallic Single-Walled Carbon Nanotubes. doi:10.1103/PhysRevLett.99.227401
 148. Yang, L., Deslippe, J., Park, C.-H., Cohen, M. L. & Louie, S. G. Excitonic Effects on the Optical Response of Graphene and Bilayer Graphene. *Phys. Rev. Lett.* **103**, 186802 (2009).
 149. Brihuega, I. *et al.* Unraveling the intrinsic and robust nature of van hove singularities in twisted bilayer graphene by scanning tunneling microscopy and

- theoretical analysis. *Phys. Rev. Lett.* **109**, 1–5 (2012).
150. Fano, U. Effects of configuration interaction on intensities and phase shifts. *Phys. Rev.* **124**, 1866–1878 (1961).
151. Luk, B. *et al.* The Fano resonance in plasmonic nanostructures and metamaterials. (2010). doi:10.1038/nmat2810
152. Havener, R. W., Liang, Y., Brown, L., Yang, L. & Park, J. Van hove singularities and excitonic effects in the optical conductivity of twisted bilayer graphene. *Nano Lett.* **14**, 3353–3357 (2014).
153. Liang, Y. *et al.* Strongly bound excitons in gapless two-dimensional structures. *Phys. Rev. B - Condens. Matter Mater. Phys.* **90**, 2–7 (2014).
154. Rohlfing, M. & Louie, S. G. Electron-hole excitations and optical spectra from first principles. *Phys. Rev. B* **62**, 4927–4944 (2000).
155. Mele, E. J. Band symmetries and singularities in twisted multilayer graphene. *Phys. Rev. B* **8420**, 235439 (2011).
156. Guevara, M. L. L. de, Claro, F. & Orellana, P. A. Ghost Fano resonance in a double quantum dot molecule attached to leads. *Phys. Rev. B* **67**, 195335 (2003).
157. Malard, L. M., Fai Mak, K., Castro Neto, A. H., Peres, N. M. R. & Heinz, T. F. Observation of intra- and inter-band transitions in the transient optical response of graphene. *New J. Phys.* **15**, (2013).
158. Ju, L. *et al.* Topological valley transport at bilayer graphene domain walls. *Nature* **520**, 650–655 (2015).
159. Tielrooij, K. J. *et al.* Generation of photovoltage in graphene on a femtosecond timescale through efficient carrier heating. *Nat. Nanotechnol.* **10**, 437–443 (2015).

160. Newson, R. W., Dean, J., Schmidt, B. & van Driel, H. M. Ultrafast carrier kinetics in exfoliated graphene and thin graphite films. *Opt. Express* **17**, 2326–2333 (2009).
161. Park, J. *et al.* Observation of the intrinsic bandgap behaviour in as-grown epitaxial twisted graphene. *Nat. Commun.* **6**, 5677 (2015).
162. Jorio, A. *et al.* Optical-phonon resonances with saddle-point excitons in twisted-Bilayer graphene. *Nano Lett.* **14**, 5687–5692 (2014).
163. Bistritzer, R. & MacDonald, A. H. Moire bands in twisted double-layer graphene. **108**, 12233–12237 (2010).
164. Luican, A. *et al.* Single-layer behavior and its breakdown in twisted graphene layers. *Phys. Rev. Lett.* **106**, 1–4 (2011).
165. Grüneis, A. *et al.* Tight-binding description of the quasiparticle dispersion of graphite and few-layer graphene. *Phys. Rev. B - Condens. Matter Mater. Phys.* **78**, 1–16 (2008).
166. Carozo, V. *et al.* Resonance effects on the Raman spectra of graphene superlattices. *Phys. Rev. B - Condens. Matter Mater. Phys.* **88**, 1–10 (2013).
167. Mele, E. J. Commensuration and interlayer coherence in twisted bilayer graphene. *Phys. Rev. B - Condens. Matter Mater. Phys.* **81**, 1–4 (2010).
168. Lopes Dos Santos, J. M. B., Peres, N. M. R. & Castro Neto, A. H. Graphene bilayer with a twist: Electronic structure. *Phys. Rev. Lett.* **99**, 19–22 (2007).
169. Ohta, T. *et al.* Evidence for interlayer coupling and moiré periodic potentials in twisted bilayer graphene. *Phys. Rev. Lett.* **109**, 1–6 (2012).
170. Lu, H., L??, R. & Zhu, B. F. Tunable Fano effect in parallel-coupled double

- quantum dot system. *Phys. Rev. B - Condens. Matter Mater. Phys.* **71**, 1–8 (2005).
171. Brown, L. *et al.* Twinning and twisting of tri- and bilayer graphene. *Nano Lett.* **12**, 1609–1615 (2012).
172. Graham, M. W., Shi, S.-F., Ralph, D. C., Park, J. & McEuen, P. L. Photocurrent measurements of supercollision cooling in graphene. *Nat. Phys.* **9**, 103–108 (2012).
173. Srivastava, A., Htoon, H., Klimov, V. I. & Kono, J. Direct observation of dark excitons in individual carbon Nanotubes: Inhomogeneity in the exchange splitting. *Phys. Rev. Lett.* **101**, 1–4 (2008).
174. Matsunaga, R., Matsuda, K. & Kanemitsu, Y. Evidence for dark excitons in a single carbon nanotube due to the Aharonov-Bohm effect. *Phys. Rev. Lett.* **101**, 3–6 (2008).
175. Deslippe, J., Spataru, C. D., Prendergast, D. & Louie, S. G. Bound excitons in metallic single-walled carbon nanotubes. *Nano Lett.* **7**, 1626–1630 (2007).
176. Li, X. *et al.* Large-area graphene single crystals grown by low-pressure chemical vapor deposition of methane on copper. *J. Am. Chem. Soc.* **133**, 2816–2819 (2011).
177. Hartland, G. V. Ultrafast studies of single semiconductor and metal nanostructures through transient absorption microscopy. *Chem. Sci.* **1**, 303 (2010).
178. Breusing, M., Ropers, C. & Elsaesser, T. Ultrafast carrier dynamics in graphite. *Phys. Rev. Lett.* **102**, 1–4 (2009).
179. Malard, L., Mak, K. & Neto, A. Observation of intra- and inter-band transitions in the transient optical response of graphene. *New J. ...* 1–10 (2013).

doi:10.1088/1367-2630/15/1/015009

180. Ni, Z., Wang, Y., Yu, T., You, Y. & Shen, Z. Reduction of Fermi velocity in folded graphene observed by resonance Raman spectroscopy. *Phys. Rev. B - Condens. Matter Mater. Phys.* **77**, 1–5 (2008).
181. Patel, H. *et al.* Tunable Optical Excitations in Twisted Bilayer Graphene Form Strongly Bound Excitons. *Nano Lett.* **15**, 5932–5937 (2015).
182. Ma, Y.-Z. *et al.* Ultrafast carrier dynamics in single-walled carbon nanotubes probed by femtosecond spectroscopy. *J. Chem. Phys.* **120**, 3368–3373 (2004).
183. Wang, F., Dukovic, G., Knoesel, E., Brus, L. E. & Heinz, T. F. Observation of rapid Auger recombination in optically excited semiconducting carbon nanotubes. *Phys. Rev. B - Condens. Matter Mater. Phys.* **70**, 1–4 (2004).
184. Wang, F., Wu, Y., Hybertsen, M. S. & Heinz, T. F. Auger recombination of excitons in one-dimensional systems. *Phys. Rev. B - Condens. Matter Mater. Phys.* **73**, 1–5 (2006).
185. Sun, D. *et al.* Observation of Rapid Exciton – Exciton Annihilation in Monolayer Molybdenum Disulfide. *Nano Lett.* **14**, 5625 (2014).
186. Mouri, S. *et al.* Nonlinear photoluminescence in atomically thin layered WSe₂ arising from diffusion-assisted exciton-exciton annihilation. *Phys. Rev. B - Condens. Matter Mater. Phys.* **90**, 1–5 (2014).
187. Yan, T., Yang, S., Li, D. & Cui, X. Long valley lifetime of free carriers in monolayer WSe₂. *arXiv* **1**, 1612.01336v1 (2016).
188. Kim, C.-J. *et al.* Chiral atomically thin films. *Nat. Nanotechnol.* **11**, 520–524 (2016).

189. Liu, W. T. *et al.* Nonlinear broadband photoluminescence of graphene induced by femtosecond laser irradiation. *Phys. Rev. B - Condens. Matter Mater. Phys.* **82**, 1–4 (2010).
190. Lui, C. H., Mak, K. F., Shan, J. & Heinz, T. F. Ultrafast Photoluminescence from Graphene.pdf. *Phys. Rev. Lett.* **105**, 1–4 (2010).
191. Park, Y. *et al.* Two-Dimensional Excitonic Photoluminescence in Graphene on a Cu Surface. *ACS Nano* **11**, 3207–3212 (2017).
192. Spataru, C. D., Ismail-Beigi, S., Benedict, L. X. & Louie, S. G. Excitonic Effects and Optical Spectra of Single-Walled Carbon Nanotubes. *Phys. Rev. Lett.* **92**, 77402 (2004).
193. Wang, F. *et al.* Observation of excitons in one-dimensional metallic single-walled carbon nanotubes. *Phys. Rev. Lett.* **99**, 1–4 (2007).
194. Wu, J. *et al.* Resonant Raman spectroscopy of twisted multilayer graphene. *Nat. Commun.* **5**, 1–8 (2014).
195. Souza, A. G. *et al.* Stokes and anti-Stokes Raman spectra of small-diameter isolated carbon nanotubes. *Phys. Rev. B* **69**, 115428 (2003).
196. Buckley, S., Radulaski, M., Biermann, K. & Vučković, J. Second harmonic generation in photonic crystal cavities in (111)-oriented GaAs. *Appl. Phys. Lett.* **103**, (2013).
197. Seyler, K. L. *et al.* Electrical control of second-harmonic generation in a WSe₂ monolayer transistor. *Nat. Nanotechnol.* **10**, 407–411 (2015).
198. Ma, Y.-Z., Valkunas, L., Bachilo, S. M. & Fleming, G. R. Exciton Binding Energy in Semiconducting Single-Walled Carbon Nanotubes. *J. Phys. Chem. B* **109**,

- 15671–15674 (2005).
199. Hanbicki, a T. *et al.* Measurement of high exciton binding energy in the monolayer WS₂ and WSe₂. *arXiv* 1412.2156 (2014).
 200. Ye, Z. *et al.* Probing excitonic dark states in single-layer tungsten disulphide. *Nature* **513**, 214–218 (2014).
 201. Lu, X., Yu, M., Huang, H. & Ruoff, R. S. Tailoring graphite with the goal of achieving single sheets. *Nanotechnology* **10**, 269–272 (1999).
 202. Wang, J., Graham, M. W., Ma, Y., Fleming, G. R. & Kaindl, R. A. Ultrafast spectroscopy of midinfrared internal exciton transitions in separated single-walled carbon nanotubes. *Phys. Rev. Lett.* **104**, 1–4 (2010).
 203. Poellmann, C. *et al.* Resonant internal quantum transitions and femtosecond radiative decay of excitons in monolayer WSe₂. *Nat. Mater.* **14**, 889–893 (2015).
 204. Cha, S. *et al.* 1s-intraexcitonic dynamics in monolayer MoS₂ probed by ultrafast mid-infrared spectroscopy. *Nat. Commun.* **7**, 10768 (2016).
 205. Hsu, J. W. P., Fitzgerald, E. A., Xie, Y. H. & Silverman, P. J. Near-field scanning optical microscopy imaging of individual threading dislocations on relaxed Ge_xSi_{1-x} films. *Appl. Phys. Lett.* **65**, 344–346 (1994).
 206. Wolf, S. A. *et al.* Spintronics: A Spin-Based Electronics Vision for the Future. *Science (80-.).* **294**, 1488–1495 (2001).
 207. Rycerz, A., Tworzydło, J. & Beenakker, C. W. J. Valley filter and valley valve in graphene. *Nat. Phys.* **3**, 172–175 (2007).
 208. Shkolnikov, Y. P., De Poortere, E. P., Tutuc, E. & Shayegan, M. Valley Splitting of AlAs Two-Dimensional Electrons in a Perpendicular Magnetic Field.

doi:10.1103/PhysRevLett.89.226805

209. Gunawan, O. *et al.* Valley susceptibility of an interacting two-dimensional electron system. *Phys. Rev. Lett.* **97**, 1–4 (2006).
210. Xiao, D., Liu, G. Bin, Feng, W., Xu, X. & Yao, W. Coupled spin and valley physics in monolayers of MoS₂ and other group-VI dichalcogenides. *Phys. Rev. Lett.* **108**, 1–5 (2012).
211. Jones, A. M. *et al.* Optical generation of excitonic valley coherence in monolayer WSe₂. *Nat. Nanotechnol.* **8**, 634–638 (2013).
212. Cao, T. *et al.* Valley-selective circular dichroism of monolayer molybdenum disulphide. *Nat. Commun.* **3**, 887 (2012).
213. Mak, K. F., He, K., Shan, J. & Heinz, T. F. Control of valley polarization in monolayer MoS₂ by optical helicity. *Nat. Nanotechnol.* **7**, 494–498 (2012).
214. Schaibley, J. Control of interlayer valley excitons in atomically-thin MoSe₂-WSe₂ heterostructures. in **10102**, 101021E (2017).
215. Eginligil, M. *et al.* ARTICLE Dichroic spin–valley photocurrent in monolayer molybdenum disulphide. (2015). doi:10.1038/ncomms8636
216. Hunt, B. *et al.* REPORTS Massive Dirac Fermions and Hofstadter Butterfly in a van der Waals Heterostructure. (2013). doi:10.1126/science.1233137
217. Woods, C. R. *et al.* Commensurate–incommensurate transition in graphene on hexagonal boron nitride. *Nat. Phys.* **10**, 1–6 (2014).
218. Rivera, P. *et al.* Valley-polarized exciton dynamics in a 2D semiconductor heterostructure. *Science (80-.)*. **351**, 688–691 (2016).
219. Yu, H., Wang, Y., Tong, Q., Xu, X. & Yao, W. Anomalous Light Cones and

- Valley Optical Selection Rules of Interlayer Excitons in Twisted Heterobilayers. *Phys. Rev. Lett.* **115**, 1–5 (2015).
220. Rivera, P. *et al.* Observation of long-lived interlayer excitons in monolayer MoSe₂–WSe₂ heterostructures. *Nat. Commun.* **6**, 6242 (2015).
221. Hong, X. *et al.* Ultrafast charge transfer in atomically thin MoS₂/WS₂ heterostructures. (2014). doi:10.1038/NNANO.2014.167
222. Zhang, Y. *et al.* Direct observation of the transition from indirect to direct bandgap in atomically thin epitaxial MoSe₂. *Nat. Nanotechnol.* **9**, 111–5 (2014).
223. Van Der Zande, A. M. *et al.* Tailoring the electronic structure in bilayer molybdenum disulfide via interlayer twist. *Nano Lett.* **14**, 3869–3875 (2014).
224. Yeh, P. C. *et al.* Direct Measurement of the Tunable Electronic Structure of Bilayer MoS₂ by Interlayer Twist. *Nano Lett.* **16**, 953–959 (2016).
225. Huang, S. *et al.* Probing the interlayer coupling of twisted bilayer MoS₂ using photoluminescence spectroscopy. *Nano Lett.* **14**, 5500–5508 (2014).
226. Puretzy, A. A. *et al.* Twisted MoSe₂ Bilayers with Variable Local Stacking and Interlayer Coupling Revealed by Low-Frequency Raman Spectroscopy. *ACS Nano* **10**, 2736–2744 (2016).
227. Zhang, C. *et al.* Interlayer couplings, Moiré patterns, and 2D electronic superlattices in MoS₂/WSe₂ hetero-bilayers. *Sci. Adv.* **3**, e1601459 (2017).
228. Rigosi, A. F., Hill, H. M., Li, Y., Chernikov, A. & Heinz, T. F. Probing Interlayer Interactions in Transition Metal Dichalcogenide Heterostructures by Optical Spectroscopy: MoS₂/WS₂ and MoSe₂/WSe₂. *Nano Lett.* **15**, 5033–5038 (2015).

229. Hsu, W.-T. *et al.* Second Harmonic Generation from Artificially Stacked Transition Metal Dichalcogenide Twisted Bilayers. **8**, (2014).

8. APPENDICES

I have been involved in several projects that lie outside the scope of 2D materials in this dissertation. Here, we describe two of the projects: finding a new class of tetrahedrite material as a solar absorber for drift based thin film solar cells and luminescence studies on a series of synthesized oxalate linked heterometallic coordination rare earth polymers.

APPENDIX A: NEW CLASS OF HIGH-EFFICINCEY THIN-FILM

TETRAHEDRITE SOLAR ABSORBER- $\text{Cu}_{10}\text{Te}_4\text{S}_{13}$

8.1 Introduction

This appendix is largely adapted from H. Patel *et al.*, “A new class of high-efficiency thin-film tetrahedrite solar absorber – $\text{Cu}_{10}\text{Te}_4\text{S}_{13}$ ”, in preparation. For high efficiency thin-film solar cells, high carriers mobility and long minority carrier lifetimes are two important considerations for the absorber layer. Another way to enhance photovoltaic (PV) efficiency is increasing the photocarrier collection via drift field.¹⁻⁴ There are two central requirements for a drift based solar cells: (i) the absorber layer must be thin with an absorption coefficient of $\alpha > 10^5 \text{ cm}^{-1}$, (ii) abrupt absorption onset near the bandgap.³⁻⁵ A computational technique for material selection guide and design was introduced by Zunger et al. called spectroscopic limited maximum efficiency (SLME).⁶ This process considers the full absorption spectrum of the absorber to improve simple Shockley-Queisser bandgap model by using the band-gap as a guide.⁵ This technique was applied by Heo et al.⁷ for the system Cu-V-VI.⁸ They found several promising candidates as a PV absorber with a significantly higher SLME value than the current known solar

absorbers. In particular, Cu-V-VI contains a group V atom in the lower 3+ oxidation state which results in flat bands in the electronic structure near the band-gap resulting in a high joint density of state. Flat bands near the band gap are responsible for abrupt absorption, which then results in a high absorption coefficient.

Here, we describe the properties of one of the candidates from the tetrahedrite material family for solar absorbers for drift based high-efficiency PV cells. We report structural, optical and electrical properties of $\text{Cu}_{10}\text{Te}_4\text{S}_{13}$. In this material, Cu vacancies on the A site lead to the presence of only $d^{10} \text{Cu}^{1+}$ and a completely filled valence band⁹ which means, this material has a low subgap absorption, low conductivity and is an intrinsic semiconductor. It exhibits promising properties for thin-film solar cells. From the computational inverse design predictions, and experimental measurements shows a strong absorption coefficient and an abrupt absorption onset near the band gap.

8.2 Experiment and Methods

8.2.1 Crystal growth and thin film deposition

The pulsed laser deposition (PLD) targets were prepared from polycrystalline $\text{Cu}_{10}\text{Te}_4\text{S}_{13}$ powders, synthesized by standard solid-state reactions from stoichiometric mixtures of Cu, Te, and S elements (purity > 99.999 %; Alfa Aesar). Details of the synthesis procedure can be found elsewhere.⁷ The targets had approximately 15% excess tellurium and 20% sulfur added to avoid the possibility of forming secondary phases during deposition, prior to being molded into pellets of ~ 2-in. diameter with the Cu:Te:S ratio of 10:4.6:15.6. The pressed pellets were sintered at 450 °C under 70 MPa pressure in a hot isostatic press (AIP HP630) and then further annealed under flowing H_2S at

450 °C to produce sample densities $\geq 97\%$ of the theoretical density. $\text{Cu}_{10}\text{Te}_4\text{S}_{13}$ thin films were deposited on the fused-silica glass substrates by ablating the targets using a 248-nm KrF pulsed excimer laser. The target-substrate separation was fixed at 7.5 cm. The substrate temperature was varied from 300 to 450°C with a laser fluence of 1.5 J cm^{-2} and a pulse rate of 10 Hz. All films were deposited in the vacuum, with a base pressure of 10^{-9} Torr. Following deposition, films were cooled rapidly in vacuum and subsequently annealed at 300 °C for 30 min in evacuated, sealed fused-silica tubes.

8.2.2 Characterization and Refinement

Glancing incidence X-ray diffraction (GIXRD) for phase identification was performed using a Rigaku Ultima-IV diffractometer with a 0.02 rad slit and Cu $K\alpha$ radiation ($\lambda = 1.5418 \text{ \AA}$) at 40 kV and 40 mA. For GIXRD scans, the instrument was configured with a 5.0° incident Soller slit, a 10 nm divergent height limiting (DHL) slit, and a 5° receiving Soller slit; the DS, SS, and RS were set to 0.2, 0.5, and 0.2 mm, respectively. Data were collected between 10 and $70^\circ 2\theta$ at a step size of $0.02^\circ 2\theta$ and a dwell time of 1 s. The resulting diffraction patterns of thin films were calibrated with the (200) reflection at $2\theta_{200} = 32.96^\circ$ from the Si powder and compared to Rietveld refinements of the powder data using TOPAS Academic Ver. 4.1.¹⁰ X-ray data of powder samples was collected on a Rigaku MiniFlex diffractometer with Cu $K\alpha$ radiation. Scans from 10 to $80^\circ 2\theta$ were collected at a step size of $0.02^\circ 2\theta$ and a dwell time of 4.5 s at each step. Rietveld refinements of the data were done applying the fundamental parameter approach to refine lattice parameters, atomic positions, and site occupancies using a previously published tetrahedrite structure as a starting configuration. Thermal parameters and site of Te were constrained to the same value, and the Cu site was

modeled using an anisotropic thermal parameter. Size and strain parameters were included within the fit to account for slight peak broadening. The chemical composition of the thin films and powders was also confirmed by an electron probe microanalyzer (EPMA) measurements using a Cameca SX100 Electron Microprobe. Core X-ray intensities of Cu, Te, S, Si, and O were recorded at three different energies – 10, 15, and 20 kV. Cu metal, X, X, elemental Si, and benitoite ($\text{BaTiSi}_3\text{O}_9$) were used as standards for Cu, Te, S, Si, and O, respectively.

8.2.3 Optical Measurements

Optical absorption coefficients and the band gap of thin films were assessed from transmission and reflection measurements using a custom-built Ocean Optics HR4000 UV-VIS and NIR256-2.5 near-infrared spectrometers with a double grating monochromator. Measurements in the ultraviolet and visible regions were performed using a xenon lamp and silicon detector. A tungsten lamp and InGaAs detector were used for near-infrared measurements.

Photoluminescence measurements were performed using a custom-built Horiba fluorolog. The fluorolog consists of a wide spectrum white light source, xenon arc lamp. This light passed through the double monochromator that selects specified excitation wavelengths with chosen slit width tolerances. The monochromatic light is then incident on the sample, the emitted light from the sample then travels to emission double monochromator which is connected to either photomultiplier tube (PMT) for UV and visible or nitrogen cooled InGaAs detector for near IR to measure number of photons emitted by the sample for a given wavelength over a period of time. In addition to the standard, excitation or emission spectrum at fixed emission or excitation wavelength, we

can also acquire 3D energetic mapping or a colored contour plot of photoluminescence by scanning the excitation, and emission wavelengths simultaneously.

Transient Absorption measurements were performed with the pump and probe beams obtained from the Chameleon and OPO. The detailed procedure is described in Chapter 2, 4. The pump beam was modulated with an acousto optic modulator and sent to a delay stage to vary the time delay between the pump and the probe beam. The collinear pump and probe beams were then coupled to a microscope. The beams were raster scanned with a confocal mirror to acquire differential reflection maps. The reflection was sent to a TE cooled InGaAs photodetector. Lock in detection was used for background free measurements.¹¹

8.2.4 Electronic Structure Calculations

First principles calculations of $\text{Cu}_{10}\text{Te}_4\text{S}_{13}$ were carried out using the Wien2K suite¹² with PAW potentials.¹³ The electronic degrees of freedom are described within the DFT framework using the generalized gradient approximation (GGA) with an appropriate value for the Hubbard U parameter (for Cu, $U = 6$ eV; for others, $U = 0$ eV), and the atomic positions are fully relaxed by HSE06 while lattice parameters were kept fixed to our experimental data. For the exchange-correlation functional, the PW91 parametrization¹⁴ for accurate total energy calculations was used with a Γ -centered $4 \times 4 \times 4$ k-point grid.

8.3 Results and Discussion

8.3.1 Crystal Structure

In the past twenty years, crystal structure and composition variation of tetrahedrite have been explored.¹⁵⁻¹⁸ The crystal structure of a tetrahedrite is shown in Figure 8.1. It has a cubic structure of I-43m symmetry with six Cu atoms occupying trigonal planar 12e sites and the other six Cu atoms occupying 12d sites. Sb or Te occupies a tetrahedral site bonded with three sulfur atoms

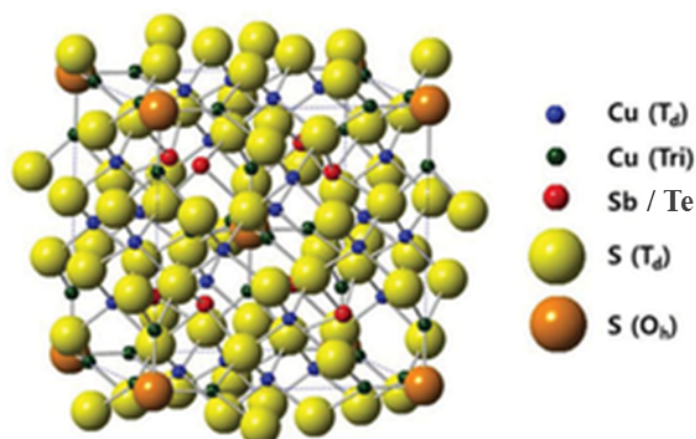


Figure 8.1: Tetrahedrite crystal structure showing Cu (Td), Cu (Tri), S (Td) and S (Oh) sites. [Adapted from ⁷.]

Monovalent Cu occupies four tetrahedral sites, a Cu^{2+} ion occupies the remaining two, and monovalent Cu occupies the trigonal planar sites in a simple crystal-chemical structure.¹⁹ There are two distinct S sites as shown in the figure. The S (Td) atoms are tetrahedrally coordinated by two Cu 12d site, one Cu 12e site and Sb or Te 8c site. The six Cu atoms in a regular octahedral coordination, 2a site surrounds the other S (Oh).²⁰

8.3.2 Electronic Structure

8.3.2.1 XRD and Band Structure

Figure 8.2a shows the XRD pattern for $\text{Cu}_{10}\text{Te}_4\text{S}_{13}$. All peaks index to a single phase tetrahedrite phase and no additional peaks due to second phases are detected. The

experimental data (circle), fitting (red) and difference (gray) is labeled. Cu atoms in trigonal sites are only vacant.

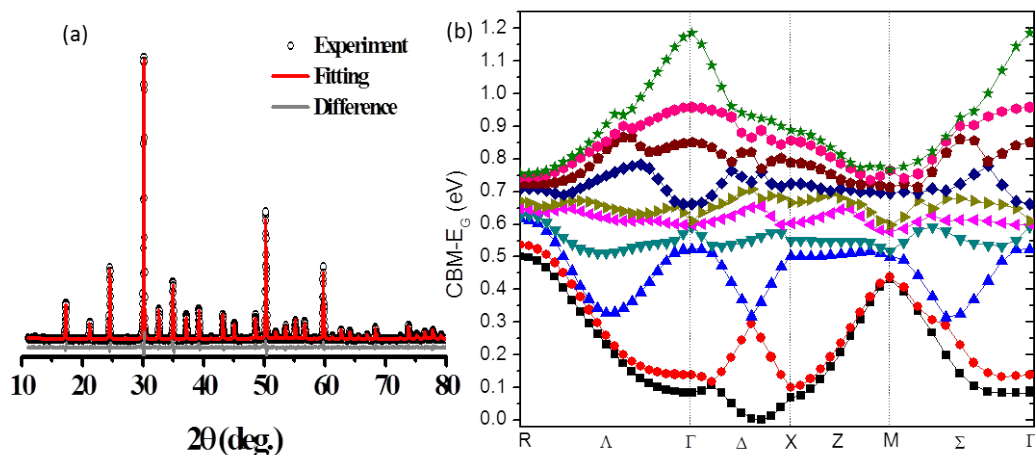


Figure 8.2: (a) XRD of $\text{Cu}_{10}\text{Te}_4\text{S}_{13}$ showing single phase tetrahedrite phase.⁷

Figure 8.2b shows the calculated band structure of $\text{Cu}_{10}\text{Te}_4\text{S}_{13}$. The lowest energy of the valence band is at the gamma point. It has a bandgap of ~ 1.4 eV with the difference between direct and indirect bandgap of ~ 0.05 eV. This small difference indicates an abrupt increase in the absorption coefficient near the band gap, which is dominated by the direct band gap contribution despite the indirect band gap nature of the material. The VBM is dominated by Cu 3d, and CBM is dominated by Te 5p states. The CBM is composed of non-bonding Te 5p states. The small cation size of Te^{4+} results in a smaller bandgap owing to a small bonding-antibonding splitting. Since the crystal radius of Te^{4+} is small ~ 0.52 Å,²¹ it leads to flat bands near CBM. As a consequence, density of states and joint density of states near the CBM increases which results in a strong absorption near the band edge.

8.3.2.2 Total and Projected Density of States

Total and projected density of states for $\text{Cu}_{10}\text{Te}_4\text{S}_{13}$ is shown in Figure 8.3. Cu 3d dominates the valence band, while Te 5p dominates the conduction band. The regions

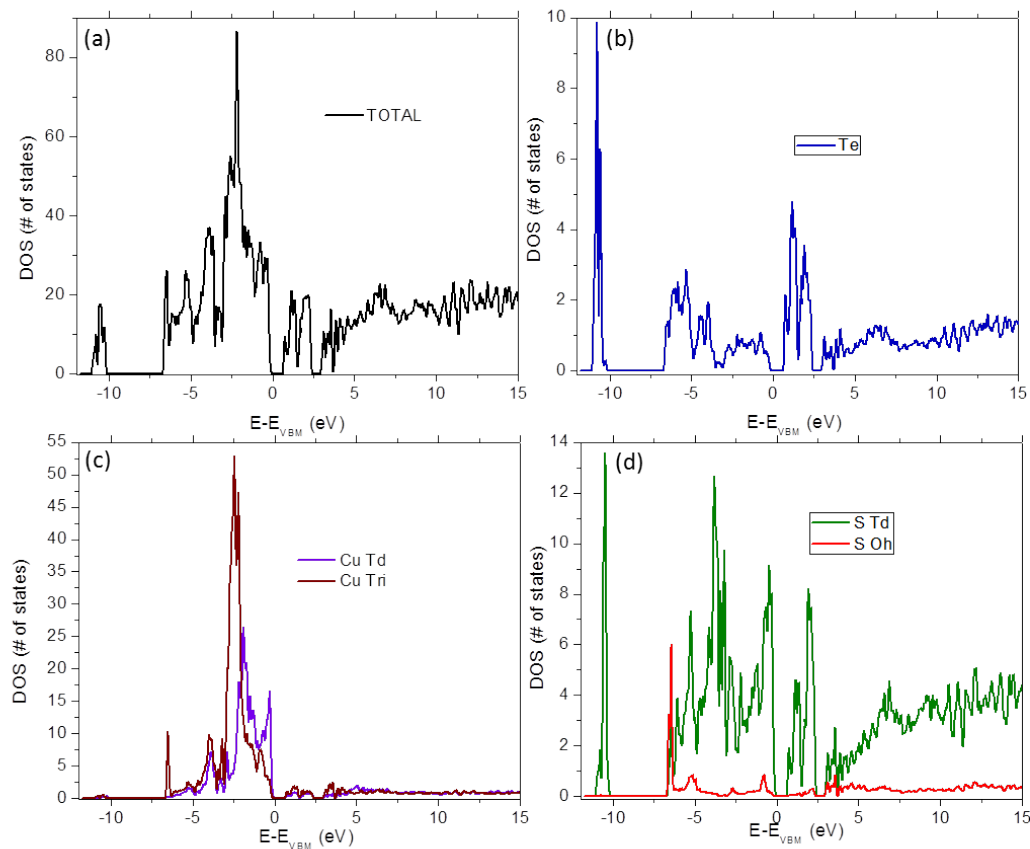


Figure 8.3: Total (a) and projected (b, c, d) density of states for $\text{Cu}_{10}\text{Te}_4\text{S}_{13}$.

with spikes in the density of states represent flat bands for bandstructure. The position of the Fermi level is shown with a dashed line and cuts the valence band.

8.3.3 Optical Properties

8.3.3.1 Optical Absorption

Figure 8.4 shows UV-VIS-IR optical absorbance calculated from transmission and reflection spectrum for $\text{Cu}_{10}\text{Te}_4\text{S}_{13}$. Abrupt absorption at 1.4 eV corresponds to the optical band gap of the material. The higher and abrupt absorption near band edge is due

to the small crystal radius of Te^{4+} resulting in a higher joint density of states near the CBM

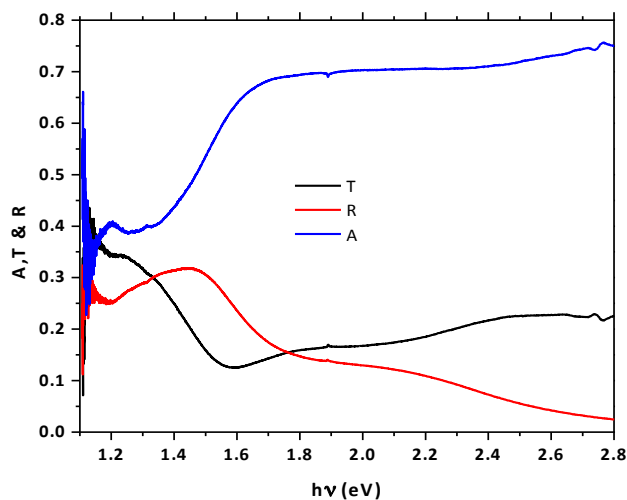


Figure 8.4: Optical absorption, transmission and reflection spectrum showing abrupt absorption edge at ~ 1.4 eV confirming the bandgap.

with low subgap absorption. It was reported by Heo et al. that the absorption onset for $\text{Cu}_{10}\text{Te}_4\text{S}_{13}$ is much steeper than $\text{Cu}_{12}\text{Sb}_4\text{S}_{13}$ or conventional thin-film solar absorber materials CdTe and CuInSe_2 .⁷

8.3.3.2 Photoluminescence

Figure 8.5 shows photoluminescence emission spectrum from $\text{Cu}_{10}\text{Te}_4\text{S}_{13}$. Upon exciting above the bandgap ~ 1.6 eV, emission peak at ~ 1.5 eV is seen. This corresponds to the predicted indirect band gap at ~ 1.5 - 1.55 eV. This first ever observed emission from $\text{Cu}_{10}\text{Te}_4\text{S}_{13}$ further confirms the band gap. It further suggests that upon exciting above the direct band gap, the carriers first relaxes through non-radiative pathways ending up in the indirect bandgap and then it emits photons via radiative relaxation pathways from the indirect band gap.

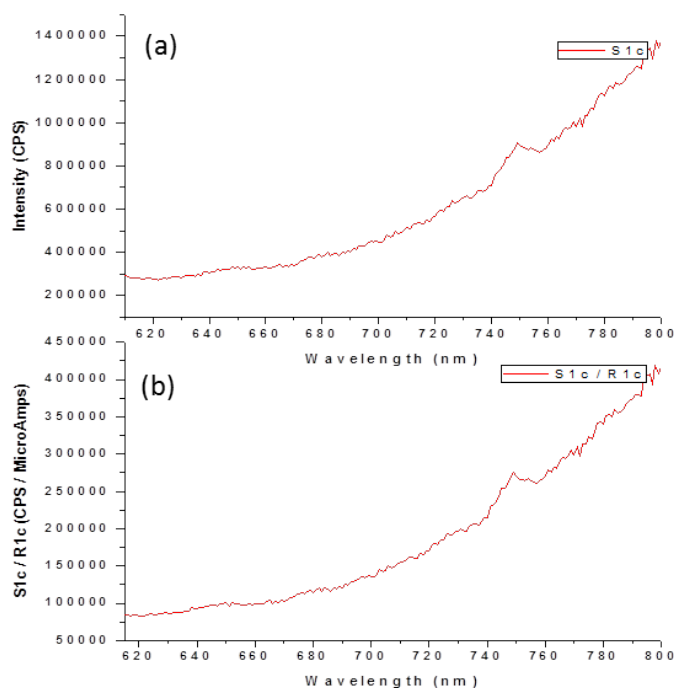


Figure 8.5: Photoluminescence spectrum of $\text{Cu}_{10}\text{Te}_4\text{S}_{13}$ for excitation above bandgap. (a) Corrected PL showing a peak at 750 nm in counts per second. (b) Normalized PL with respect to the background fluctuations confirming (a). Sloping towards 800 nm is an artifact of the detection system.

8.3.3.3 Transient Absorption Microscopy

It is important to characterize carrier lifetime in a solar cell material since the lifetimes can help predict the efficiency of the solar cell device. Figure 8.6b shows transient absorption (TA) measurements for carrier lifetimes on $\text{Cu}_{10}\text{Te}_4\text{S}_{13}$ on resonance with different pump and probe combinations. The detailed experimental setup is described in Chapter 2, 4, 5. The time-dependent transient technique contains essential information on the important physical processes, which control carrier recombination. In our TA microscopy approach, we measure relative electron population as a function of time for a given pump and probe energy. The experiment is outlined in Figure 8.6a, we

are pumping with energy ~ 1.65 eV above the direct band gap and probing with energies 1.54 eV (on resonance with the direct band gap), 1.45 eV (below direct band gap and above indirect band gap), 1.40 eV (on resonance with the indirect bandgap), 1.23 eV (far below direct and indirect band gap).

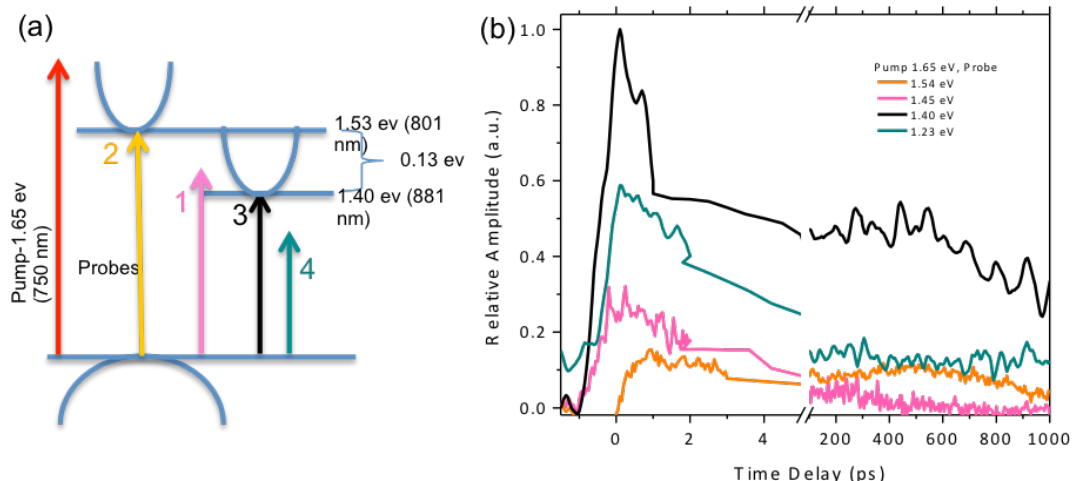


Figure 8.6: Time dynamics of $\text{Cu}_{10}\text{Te}_4\text{S}_{13}$. (a) Sketch of energy level showing pump and probe combinations used. (b) Time dynamics shows long lifetimes upon pumping above band gap and probing well below the direct and indirect bandgap suggesting long minority carrier lifetime.

Pumping above the direct band gap and probing slightly below the direct band gap (arrow 1 in Figure 8.6a) is analogous to the conventional optical absorption. The charge carriers from the direct band gap decay to the indirect band gap and then decay down to the ground state resulting in ~ 575 ps charge carrier lifetime (Figure 8.6b). Arrow 2 in figure A6 a, corresponds to pumping above and probing at the direct bandgap resulting in a lifetime of ~ 1.1 ns (Figure 8.6b). In this case, some of the charge carriers will go to the indirect band gap, most of the charge carriers will fall down to the ground state directly. Arrow 3 in Figure 8.6 shows pumping above the direct band gap and probing at the

indirect bandgap. This represents multiple radiative and non-radiative relaxation pathways with carrier lifetimes of >1.2 ns. From our photoluminescence measurements, we conclude that the charge carriers relax from the indirect band gap via a radiative pathway. Arrow 4 in Figure 8.6 shows pumping above the direct band gap and probing far below the indirect band gap resulting in lifetimes of >1.4 ns. If there are no defects, there are no available sites for carriers to occupy, on the other hand, if there are defect sites and deep energy levels or sub gap state, the charge carriers get trapped and lifetimes increases. Our results suggest long minority carrier lifetimes in $\text{Cu}_{10}\text{Te}_4\text{S}_{13}$. Further measurements, such as transient photoconductivity decay and transient photoluminescence decay could give more insights on recombination and photoconductivity for quantitative analysis of the efficiency of a solar cell device with $\text{Cu}_{10}\text{Te}_4\text{S}_{13}$ as a solar absorber layer for practical applications.

8.4 Summary

Based on inverse design, the derived material $\text{Cu}_{10}\text{Te}_4\text{S}_{13}$ from the tetrahedrite exhibits promising properties for high-efficiency thin film solar cell absorber layer. We synthesized $\text{Cu}_{10}\text{Te}_4\text{S}_{13}$ and performed various experiments to test the predicted properties. We find that as predicted it is an indirect band gap material, however, due to the small difference between direct and indirect band gap, lots of properties are dominated by the direct band gap. It has higher absorption coefficient than conventional thin film solar absorber materials such as CdSe, and others. It has an abrupt absorption near band gap and the flat band near the band edge due to the large joint density of states. We have further confirmed that it decays through non-radiative pathways and radiative

pathway through an indirect bandgap upon exciting above direct band gap. The minority carrier lifetimes are large upon exciting above the direct bandgap. This material is predicted to achieve efficiency great than 20% in a drift based solar cell mode with absorber layer as thin as 250 nm. This study opens up new possibilities for an efficient solar cell with ultra thin absorber layer for PV applications.

References

1. Sargent, E. Colloidal quantum dot solar cells. *Nat. Photonics* **6**, 133–135 (2012).
2. Johnston, K. W. *et al.* Efficient Schottky-quantum-dot photovoltaics: The roles of depletion, drift, and diffusion. *Appl. Phys. Lett.* **92**, 1–3 (2008).
3. *Handbook of Photovoltaic Science and Engineering*. (John Wiley & Sons, Ltd, 2010). doi:10.1002/9780470974704
4. Introduction. in *Third Generation Photovoltaics* 1–6 (Springer Berlin Heidelberg). doi:10.1007/3-540-26563-5_1
5. Shockley, W. & Queisser, H. J. Detailed balance limit of efficiency of p-n junction solar cells. *J. Appl. Phys.* **32**, 510–519 (1961).
6. Yu, L. & Zunger, A. Identification of Potential Photovoltaic Absorbers Based on First-Principles Spectroscopic Screening of Materials. doi:10.1103/PhysRevLett.108.068701
7. Heo, J. *et al.* Design meets nature: Tetrahedrite solar absorbers. *Adv. Energy Mater.* **5**, (2015).
8. Yu, L., Kokenyesi, R. S., Keszler, D. A. & Zunger, A. Inverse design of high absorption thin-film photovoltaic materials. *Adv. Energy Mater.* **3**, 43–48 (2013).
9. Trtjdu', A. G. CRYSTALLOGRAPHY, MINERAL CHEMISTRY AND CHEMICAL NOMENCLATURE OF GOLDFIELDITE, THE TELLURIAN MEMBER OF THE TETRAHEDRITE SOLID.SOLUTION SERIES. **36**, 15–137 (1998).
10. Alan A. Coelho. TOPAS-Academic-Version 4.1 Technical Reference (2007). Available at: <http://www.topas-academic.net/>. (Accessed: 22nd July 2017)

11. Patel, H. *et al.* Tunable Optical Excitations in Twisted Bilayer Graphene Form Strongly Bound Excitons. *Nano Lett.* **15**, 5932–5937 (2015).
12. Blaha, P. *et al.* WIEN2k An Augmented Plane Wave Plus Local Orbitals Program for Calculating Crystal Properties User's Guide, WIEN2k 17.1 (Release 07/03/2017) WIEN2k An Augmented Plane Wave + Local Orbitals Program for Calculating Crystal Properties.
13. Kresse, G. & Furthmüller, J. Efficient iterative schemes for ab initio total-energy calculations using a plane-wave basis set. *Phys. Rev. B* **54**, 11169–11186 (1996).
14. Perdew, J. *et al.* Atoms, molecules, solids, and surfaces: Applications of the generalized gradient approximation for exchange and correlation. *Phys. Rev. B* **46**, 6671–6687 (1992).
15. Pfitzner, A., Evain, M. & Petricek, V. Cu₁₂Sb₄S₁₃: A Temperature-Dependent Structure Investigation. *Acta Crystallogr. Sect. B Struct. Sci.* **53**, 337–345 (1997).
16. Jeanloz, R. & Johnson, M. L. A note on the bonding, optical spectrum and composition of tetrahedrite. *Phys. Chem. Miner.* **11**, 52–54 (1984).
17. Patrick, R. A. D., van der Laan, G., Vaughan, D. J. & Henderson, C. M. B. Oxidation state and electronic configuration determination of copper in tetrahedrite group minerals by L-edge X-ray absorption spectroscopy. *Phys. Chem. Miner.* **20**, 395–401 (1993).
18. Lu, X. THERMOELECTRIC PROPERTIES OF NATURAL MINERAL BASED TETRAHEDRITE COMPOUNDS. (2014).
19. Di Benedetto, F. *et al.* The distribution of Cu(II) and the magnetic properties of the synthetic analogue of tetrahedrite: Cu₁₂Sb₄S₁₃. *Phys. Chem. Miner.* **32**, 155–164

(2005).

20. J Wuensch, B. B., Takeuchi, Y., Nowacki, W., Kristallogr Ed, Z. & Wuensch, B. J. Refinement of the crystal structure of binnite₁, CU₁₂As₄S₁₃. **123**, 1–20 (1966).
21. Shannon, R. D. Revised Effective Ionic Radii and Systematic Studies of Interatomic Distances in Halides and Chalcogenides. *Acta Cryst* **32**, (1976).

APPENDIX B: LUMINESCENCE STUDIES ON SERIES OF OXALATE LINKED HETEROMETALLIC COORDINATION POLYMERS

Here we describe, a brief summary of the work that is in the submission process for peer review process: Collin N. Muniz, Hiral Patel, Dylan B. Fast, Lauren S. Rohwer, Eric W. Reinheimer, Michelle Dolgos, Matt W. Graham, May Nyman, “Synthesis, structural characterization, and luminescence studies of an unreported series of oxalate linked heterometallic coordination polymers”. My contribution to this work was performing photoluminescence studies and analysis of the rare-earth materials.

We demonstrate characteristic emission, and high Eu^{3+} and Tb^{3+} emission quantum yields of $\sim 70\%$ owing to the efficient Ln spacing and the absence of water in the lattice. We synthesize the previously unreported series of heterometallic, rare earth-niobate coordination polymers of the formula $[\text{LnNbO}(\text{C}_2\text{O}_4)_3(\text{DMSO})_3]$ Ln = (La, Ce, Nd, Sm, Eu, Gd, Tb) and Ln = (Dy, Ho, Er, Tm, and Yb). We perform Rietveld refinement techniques to understand the structural variation as a function of ionic radius in a single crystal of the La analogue.

